Estimating Surface Heat Fluxes Using Temperature and Wetness Information
A Particle Data Assimilation Framework

Lu, Yang

DOI
10.4233/uuid:c1040427-364d-485b-bebd-f23a89e217aa

Publication date
2019

Document Version
Final published version

Citation (APA)
Lu, Y. (2019). *Estimating Surface Heat Fluxes Using Temperature and Wetness Information: A Particle Data Assimilation Framework*. [Dissertation (TU Delft), Delft University of Technology].
https://doi.org/10.4233/uuid:c1040427-364d-485b-bebd-f23a89e217aa

Important note
To cite this publication, please use the final published version (if applicable).
Please check the document version above.

Estimating Surface Heat Fluxes Using Temperature And Wetness Information

A Particle Data Assimilation Framework

Estimating Surface Heat Fluxes Using Temperature And Wetness Information

A Particle Data Assimilation Framework

Proefschrift

ter verkrijging van de graad van doctor
aan de Technische Universiteit Delft,
op gezag van de Rector Magnificus Prof. dr. ir. T.H.J.J. van der Hagen,
voorzitter van het College voor Promoties,
in het openbaar te verdedigen op dinsdag 14 januari 2019 om 15:00 uur

door

Yang Lu

Master of Science in Cartology and Geographic Information System,
Beijing Normal University, China,
geboren te Xinyang, Henan Province, China.

Dit proefschrift is goedgekeurd door de

promotor: Prof. dr. ir. S.C. Steele-Dunne
promotor: Prof. dr. ir. N.C. van de Giesen

Samenstelling promotiecommissie:

Rector Magnificus,	voorzitter
Prof. dr. ir. S.C. Steele-Dunne,	Technische Universiteit Delft
Prof. dr. ir. N.C. van de Giesen,	Technische Universiteit Delft
Onafhankelijke leden:	
Prof. dr. ir. A.W. Heemink	Technische Universiteit Delft
Prof. dr. ir. B.J.H. van de Wiel	Technische Universiteit Delft
Prof. dr. ir. M.F.P. Bierkens	Universiteit Utrecht
Prof. dr. ir. G. De Lannoy	Katholieke Universiteit Leuven
Dr. rer. nat. C. Montzka,	Forschungszentrum Jülich

Keywords: Surface Heat Fluxes, Soil Moisture, Land Surface Temperature, Brightness Temperature, Data Assimilation

Printed by: Ipskamp Printing, Enschede

Front & Back: Designed by Xinyi Tang (5-yr old) & Yang Lu.

ISBN 978-94-028-1341-8

An electronic version of this dissertation is available at
http://repository.tudelft.nl/.

to my family

CONTENTS

SUMMARY

Surface heat fluxes (latent and sensible heat over the land surface) play a key role in the land-atmosphere interaction, and their spatial pattern as well as temporal evolution are vital to the terrestrial water cycle and surface energy balance. Ideally, we want to have accurate estimates of spatially distributed and temporally continuous fluxes. However, this cannot be achieved through interpolation of point measurements because of the limited number of flux stations and the high heterogeneity of fluxes, nor can this be done using large scale monitoring platforms such as remote sensing, since fluxes lack a unique signature that can be detected by satellites. Given the fact that surface heat fluxes are closely related to the thermal and wetness condition of the land surface, which are available from remote sensing instruments, this PhD research proposes a methodology to improve flux estimates by assimilating land surface temperature (LST) and soil wetness information into a coupled water and heat transfer model. The goal is to acquire accurate flux estimates over a large area using a simple model and a small suite of input data.

Chapter 1 provides a brief overview of the traditional methods used to estimate surface heat fluxes and discusses their respective advantages and limitations. The reason why a data assimilation approach is adopted for this research is also discussed.

Chapter 2 introduces the basic framework used in this dissertation, including the surface energy balance scheme, the coupled heat and water transfer model and the particle data assimilation formulations.

Based on previous studies, a data assimilation approach is proposed in Chapter 3, in which LST time series and soil moisture measurements are jointly assimilated using a particle batch smoother (PBS). The methodology is applied at point scale, and the results are compared to a LST-only assimilation case. The goal is to evaluate the improvement in flux estimates by exerting stronger constraints on surface energy partitioning by incorporating soil wetness information. The results demonstrate that assimilating soil moisture data improves flux estimates at 30-min time step, particularly over wet or densely vegetated surfaces. The improvement is more evident when LST observations are sparse.

Following the successful application at point scale using in situ measured LST and soil moisture data, the methodology is improved to be applicable over a large area using remote sensing observations in Chapter 4. The major challenges are to estimate land surface parameters without any prior knowledge, and to bridge the resolution gap between different remote sensing data sets. A simple model based on leaf area index (LAI) is adopted to characterize the land surface control on fluxes, and a hybrid particle assimilation strategy is proposed to facilitate the assimilation of remote sensing data. In this strategy, soil moisture data are assimilated using a particle filter, while LST time series is assimilated using an adaptive particle batch smoother (APBS). The results prove that despite the coarse resolution, assimilating remote sensing soil moisture data leads to im-

provement in both soil moisture states and surface heat flux estimates at finer scale. The methodology is independent of ground measurements, therefore is easily transferable to other regions.

A potential risk of assimilating remote sensing soil moisture data lies in the retrieval algorithm, which utilizes background information including, for example, LST. These data are often outputs of other models, which may be inconsistent or even contradictory to the simulations in the assimilation system. Therefore, a more physically consistent study is conducted in Chapter 5 which assimilates brightness temperature – the direct measurements of satellite microwave radiometers instead of soil moisture retrievals. The state propagation model is coupled to a radiative transfer model which translates modeled soil moisture into brightness temperature estimates. Brightness temperatures at horizontal and vertical polarization are assimilated separately, and the estimates are compared to those from Chapter 4. The results show that assimilating LST with brightness temperature or soil moisture leads to similar flux estimates, while assimilating brightness temperature slightly outperforms assimilating soil moisture for improving soil moisture estimates.

To explore the impact of spatio-temporal resolution of remote sensing soil moisture information on surface heat flux estimates, two comparative experiments are performed in Chapter 6, in which soil moisture data with enhanced spatial or temporal resolution are assimilated, respectively. The results indicate that surface heat flux estimates cannot be improved further by enhancing the resolution of soil moisture data, and imply that information from other sources should be introduced.

A summary of knowledge generated from this PhD research and prospectives on future research are given in Chapter 7.

SAMENVATTING

‘Surface heat fluxes’ (latente en voelbare warmtestromingen vanaf en naar het landoppervlak) spelen een sleutelrol in de interactie tussen land en atmosfeer, en hun ruimtelijke patroon en hun evolutie in de tijd zijn van vitaal belang voor de terrestrische waterkringloop en energiebalans. Idealiter willen we nauwkeurige schattingen van ruimtelijk gedistribueerde en temporeel continue fluxen. Dit kan echter niet worden bereikt door interpolatie van puntmetingen vanwege het beperkte aantal flux-meetstations en de hoge heterogeniteit van fluxen, noch kan dit worden gedaan met behulp van grootschalige monitoringstechnieken zoals remote sensing, omdat fluxen geen unieke signatuur hebben die kan worden gedetecteerd door satellieten. Gezien het feit dat surface heat fluxes nauw verwant zijn aan de thermische toestand en vochtigheidstoestand van het landoppervlak, die beschikbaar zijn via remote sensing-instrumenten, wordt in dit promotieonderzoek een methode voorgesteld om de fluxschattingen te verbeteren door de oppervlaktetemperatuur van het land (land surface temperature: LST) en bodemvochtinformatie te assimileren in een gekoppeld water- en warmteoverdrachtsmodel. Het doel is om nauwkeurige fluxschattingen over een groot gebied te verkrijgen met behulp van een eenvoudig model en een kleine set aan invoergegevens.

Hoofdstuk 1 geeft een kort overzicht van de traditionele methoden die worden gebruikt om surface heat fluxes te schatten en bespreekt hun respectievelijke voordelen en beperkingen. De reden waarom een data-assimilatiebenadering wordt gebruikt voor dit onderzoek wordt ook besproken.

Hoofdstuk 2 introduceert het basisraamwerk dat in dit proefschrift wordt gebruikt, inclusief het energiebalansschema van het oppervlak, het gekoppelde warmte- en wateroverdrachtsmodel en de ‘particle’ data-assimilatieformuleringen.

Op basis van voorgaande studies wordt een benadering voor data-assimilatie voorgesteld in hoofdstuk 3, waarin LST-tijdreeksen en bodemvochtmetingen gezamenlijk worden geassimileerd met behulp van een ‘particle batch smoother’ (PBS). De methodologie wordt toegepast op puntschaal en de resultaten worden vergeleken met een case van alleen LST-assimilatie. Het doel is om de verbetering in fluxschattingen te evalueren. Dit wordt gedaan door sterkere beperkingen op de verdeling van oppervlakte-energie uit te oefenen door middel van het meenemen van informatie over bodemvocht. De resultaten tonen aan dat het assimileren van bodemvocht de fluxschattingen voor een tijdstap van 30-min verbetert, in het bijzonder over natte of dichtbegroeide oppervlakken. De verbetering is duidelijker wanneer LST-waarnemingen schaars zijn.

Volgend op de succesvolle toepassing op puntschaal, met behulp van in situ gemeten LST en bodemvochtgegevens, is de methodologie verbeterd om toepasbaar te zijn over een groot gebied met behulp van remote sensing-observaties in hoofdstuk 4. De belangrijkste uitdagingen zijn het schatten van de landoppervlakteparameters zonder enige voorkennis, en om de kloof in resolutie tussen verschillende datasets voor remote sensing te overbruggen. Een eenvoudig model op basis van de bladoppervlakte-index

(leaf area index: LAI) wordt gebruikt om de sterkte van de invloed van het landoppervlak op fluxen te karakteriseren. Ook wordt er een hybride particle-assimilatiestrategie voorgesteld om de assimilatie van remote sensing-gegevens te vergemakkelijken. In deze strategie worden bodemvochtgegevens geassimileerd met behulp van een particle filter, terwijl LST-tijdreeksen worden geassimileerd met behulp van een adaptieve particle batch smoother (APBS). De resultaten bewijzen dat, ondanks de grove resolutie, het assimileren van door middel van remote sensing verkregen bodemvochtgegevens leidt tot verbetering van zowel bodemvochttoestanden als schattingen van de oppervlaktewarmteflux op fijnere schaal. De methodologie is onafhankelijk van metingen van grondstations en kan daarom eenvoudig worden overgedragen naar andere regio's.

Een potentieel risico van het assimileren van remote sensing-gegevens van bodemvocht op afstand, ligt in het afleidingsalgoritme dat achtergrondinformatie gebruikt, waaronder bijvoorbeeld LST. Deze gegevens zijn vaak outputs van andere modellen, die inconsistent of zelfs tegenstrijdig kunnen zijn met de simulaties in het assimilatiesysteem. Daarom wordt in hoofdstuk 5 een meer fysiek consistente studie uitgevoerd die de helderheidstemperatuur assimileert - de directe metingen van satelliet-microgolfradiometers in plaats van bodemvochtproducten. Het toestandsmodel is gekoppeld aan een stralingstransfermodel dat gemodelleerd bodemvocht omzet in schattingen van helderheidstemperatuur. Helderheidstemperaturen bij horizontale en verticale polarisatie worden afzonderlijk geassimileerd en de schattingen worden vergeleken met die uit hoofdstuk 4. De resultaten tonen aan dat het assimileren van LST met helderheidstemperatuur of bodemvocht leidt tot vergelijkbare fluxschattingen, terwijl het assimileren van de helderheidstemperatuur enigszins beter is dan het assimileren van bodemvocht om de schattingen van bodemvocht verbeteren.

Om de impact van de resolutie in tijd en ruimte van op remote sensing gebaseerde bodemvochtinformatie op schattingen van surface heat fluxes te onderzoeken worden twee vergelijkings-experimenten uitgevoerd in Hoofdstuk 6, waarin bodemvochtgegevens met verbeterde ruimtelijke of temporele resolutie worden geassimileerd. De resultaten geven aan dat schattingen van surface heat fluxes niet verder kunnen worden verbeterd door de resolutie van bodemvochtgegevens te verbeteren, en impliceren dat er informatie uit andere bronnen moet worden bijgehaald.

Een samenvatting van de kennis die is voortgekomen uit dit promotieonderzoek en perspectieven voor toekomstig onderzoek, wordt gegeven in hoofdstuk 7.

1

INTRODUCTION

1

1.1. SURFACE HEAT FLUXES: WHY DO WE CARE?

SURFACE heat fluxes, in particular sensible and latent heat fluxes, play a key role in the terrestrial water and energy cycle. Sensible heat flux refers to the conductive heat flux from the land surface to the atmosphere, while latent heat flux mainly refers to the heat flux that is related to the evaporation or transpiration of water at the land surface. As a link between the land surface water, energy and carbon exchanges with the atmosphere [Xu et al., 2014], their magnitude and relative partitioning ultimately influence cloud growth, rainfall formation, heat wave variability [Ma et al., 2010; Bateni and Entekhabi, 2012b; Wang and Dickinson, 2012], etc., exerting a profound impact on the climate and terrestrial biosphere. Thus an accurate estimation of the spatial pattern as well as the temporal evolution of surface heat fluxes is central to hydrology, meteorology, water resources management and climate studies [Rigden and Salvucci, 2015].

1.2. IN SITU FLUX MEASUREMENTS

The most commonly used in situ surface heat flux measurement techniques are the eddy covariance (EC) and the Bowen radio (BR) techniques. The EC instruments measure sensible and latent heat fluxes separately from the covariance of heat and moisture fluxes. Although the techniques are relatively accurate for a variety of situations [Foken, 2008; Vickers et al., 2010], they can have problems with energy balance closure [Wilson et al., 2002] which often leads to underestimation of fluxes, particularly for latent heat flux. Consequently, a correction procedure is often needed to close the energy balance [Twine et al., 2000]. The BR method simultaneously measures the vertical gradients of air temperature and humidity to partition the available energy at the surface to sensible and latent heat fluxes. The aerodynamic resistances to heat and water vapor are assumed equal, and the energy balance is closed by design. Both methods are able to provide measurements of up to 30 minutes at a spatial scale of hundreds of meters [Wang and Dickinson, 2012], but they are susceptible to weather conditions, and are only available from a handful of sparse flux networks, e.g., FLUXNET [Baldocchi et al., 2001].

1.3. LARGE SCALE FLUX ESTIMATION

It is difficult to obtain surface heat fluxes over a large area by direct interpolation of point measurements because of the limited number and uneven distribution of flux stations, as well as the heterogeneous nature of fluxes in space and time. Direct monitoring using remote sensing instruments is also impossible since surface heat fluxes do not have a unique signature that can be detected remotely. Previous studies for large scale flux estimation can be categorized into two groups. The first group is known as the 'triangle methods', which calculates surface heat fluxes from local predictors such as land surface temperature (LST) and vegetation indices [Tang et al., 2010; Chirouze et al., 2014; Minacapilli et al., 2016; Zhu et al., 2017] by building empirical relationships between them. These methods are easy to implement, but are largely dependent on historical data to train the model. The second group of methods adopts surface energy balance (SEB) models [Su, 2002; Bastiaanssen et al., 1998a,b; Allen et al., 2007; Anderson et al., 2011; Holmes et al., 2018] or land surface models (LSM) [Oleson et al., 2010; Niu et al., 2011; Zheng et al., 2015], and surface heat fluxes are estimated by solving the energy balance

equations. These models apply to a wide range of surface and weather conditions, but often require a large suite of input data.

1.4. DATA ASSIMILATION FOR FLUX ESTIMATION

In this dissertation, data assimilation will be used to estimate surface heat fluxes. Data assimilation refers to a wide range of techniques for combining complementary information from model simulations and observations into an optimal estimate of the geophysical field of interest [Reichle, 2008]. The most popular methods are variational data assimilation (VDA) methods, Kalman filter-based methods and particle methods.

VDA methods merge model simulations with observations by constructing and minimizing a cost function derived from the forward model within a time window [Alavi et al., 2009]. The VDA methods yield theoretically optimal estimates, and have been extensively used in hydrological applications [Reichle et al., 2001a,b; Seo et al., 2003; Lee et al., 2012]. However, VDA methods also suffer from several shortcomings. First, the VDA methods require a model adjoint to be derived, which is a difficult and time-consuming task. Second, VDA methods yield only a deterministic solution, and additional efforts need to be made to determine the estimation uncertainty. In addition, the background error covariance needs to be determined, which is very computationally demanding [Bateni and Entekhabi, 2012b].

The Kalman filter [Kalman, 1960] is one of the most widely used assimilation methods. It is a recursive filter developed for linear systems. When the model and observation errors are normally distributed, optimal results can be obtained for linear systems. For non-linear systems, variations of the Kalman filter have been developed, such as the extended Kalman filter (EKF, [Jazwinski, 1970]) and the ensemble Kalman filter (EnKF, [Evensen, 1994]). In particular, the EnKF and its extension ensemble Kalman smoother (EnKS, [Evensen and Van Leeuwen, 2000]) are based on the Monte Carlo theory and approximates the first two moments of the model prior distribution using random samples. The difference between EnKF and EnKS is that the EnKF only updates states at the observation time, while the EnKS also uses observations to update states at previous times. The EnKF and EnKS can be easily implemented with complex models, and have been widely used in hydrological applications such as soil moisture [Margulis et al., 2002; Dunne and Entekhabi, 2006; Dunne et al., 2007; De Lannoy et al., 2007a; Sahoo et al., 2013; Lievens et al., 2016, 2017b] and streamflow [Wanders et al., 2014; Lievens et al., 2016] estimation.

When the Gaussian assumption is violated and the system is highly non-linear, EnKF is unable to yield optimal solutions. On this condition, the particle filter (PF) may outperform EnKF, since the particle methods have their origin in Bayesian estimation, and map the entire prior distribution using Monte Carlo sampling [Moradkhani et al., 2005]. Therefore, the PF is theoretically better suited for hydrological applications, as it makes no assumptions on the prior distribution of the errors [Moradkhani et al., 2005; Dong et al., 2015; Yan and Moradkhani, 2016]. Some studies also suggested that the PF provides better estimates in parameter estimation [DeChant and Moradkhani, 2012; Dong et al., 2016b]. Despite the advantages, the particle methods are prone to particle degeneracy, which is the situation when most of the particles have negligible weights and the estimates become dominated by a small number of particles. To avoid this problem,

resampling of the posterior after each update is necessary.

In contrast to the direct modeling approaches to estimating surface heat fluxes discussed in the previous section, some studies have focused on assimilating time series of LST observations into simple heat transfer models to characterize the partitioning between diurnal sensible and latent heat fluxes. The rationale is that the energy partitioning at the land surface influences the temporal evolution of LST, therefore the information on energy partitioning can be extracted from time series of LST observations. The physical basis is that different surface energy balance components differ in the relative efficiency in dissipating available energy at the land surface [Bateni and Entekhabi, 2012a]. These studies generally aim to estimate two key parameters: (1) a bulk heat transfer coefficient for neutral atmosphere (C_{HN}) which scales the sum of sensible and latent heat fluxes, and (2) a daytime (09:00-16:00 LT) constant evaporative fraction (EF) which represents the partitioning between sensible and latent heat fluxes. This methodology has been successfully applied using variational assimilation [Castelli et al., 1999; Boni et al., 2001; Caparrini et al., 2003, 2004a,b; Crow and Kustas, 2005; Bateni and Liang, 2012; Bateni et al., 2013b,a; Xu et al., 2014, 2015] and EnKS [Bateni and Entekhabi, 2012b; Xu et al., 2018]. Recently, a particle batch smoother (PBS) has been developed and used for soil moisture [Dong et al., 2015] and snow water equivalent [Margulis et al., 2015] estimation, but no applications have been performed on surface heat flux estimation.

1.5. KNOWLEDGE GAP

Although LST time series implicitly contains information on surface energy partitioning, many studies have demonstrated that the LST-only assimilation strategy performs poorly on wet or densely vegetated surfaces [Caparrini et al., 2004a; Crow and Kustas, 2005; Xu et al., 2014]. This happens because the surface energy partitioning becomes more energy-limited under these conditions, which weakens the constraint of LST time series on surface energy partitioning [Caparrini et al., 2004a]. Sini et al. [2008] demonstrated that using antecedent precipitation index (API) which is an indicator of soil moisture to constrain EF could further improve flux estimations under these conditions. However, joint assimilation of LST and soil moisture data has not been conducted. It is unclear to what extent surface heat flux estimates can be improved by including soil moisture information, particularly through comparative experiments against LST-only assimilation cases. In addition, previous studies have used variational methods and EnKS, while no applications have been conducted using particle approaches, despite the need for a particle smoothing application concerning the non-linearity and non-Gaussianity of hydrological systems. Finally, with the development of remote sensing techniques, especially with the operational soil moisture data streams from the METOP-A advanced scatterometer (ASCAT) [Bartalis et al., 2007], the ESA Soil Moisture Ocean Salinity (SMOS) mission [Kerr et al., 2001] and the NASA Soil Moisture Active Passive (SMAP) mission [Entekhabi et al., 2010] as well as merged products such as the ESA Climate Change Initiative (CCI) soil moisture [Dorigo et al., 2015], it becomes increasingly important and beneficial to evaluate the applicability of this methodology at broad scales. However, contrasting resolution gap exists between remote sensing soil moisture (typically >30 km every 2-3 days from microwave radiometers) and LST (typically <5 km hourly from geostationary satellites) data. An appropriate assimilation strategy needs to

be proposed, which should efficiently bridge the large resolution gap.

1.6. RESEARCH OUTLINE

The objective of this PhD research is to propose a data assimilation framework that facilitates large scale surface heat flux mapping by assimilating remote sensing LST and soil moisture information. The following chapters are structured as follows:

Chapter 2 describes the basic assimilation framework used in this dissertation, including surface energy balance, assimilation methods and state propagation models.

A point scale experiment is conducted in Chapter 3 using in situ measured forcing data and observations and aims to answer three questions: (1) Can particle smoothing methods be used to improve surface heat flux estimates by assimilating LST time series? (2) Can the estimates be further improved by including soil moisture observations, particularly on wet or densely vegetated surfaces? (3) Will the application robustness be affected when the number of LST observations is limited in remote sensing applications? The main goal is to test the applicability of the proposed methodology for the next step application at broader scale using remote sensing data.

Chapter 4 is focused on applying the proposed methodology to remote sensing data and aims to answer three questions: (1) Can the methodology tested at point scale be applied to improve surface heat flux estimates over a large area using remote sensing data? (2) How can the spatial and temporal resolution gap between soil moisture and LST data be bridged? (3) What is the added value of remote sensing soil moisture data, given the coarse spatial and temporal resolution? To maximize the applicability of the methodology, the forcing data are provided by remote sensing or reanalysis products, and in situ flux observations are not required for calibration. As the dependence on in situ data is minimized, the methodology can be easily applied to other areas.

Chapter 5 compares the assimilation of LST data with either direct brightness temperature observations or soil moisture retrievals, and aims to answer two questions: (1) Will flux estimates be further improved by directly assimilating brightness temperature observations instead of soil moisture retrievals? (2) What is the difference between assimilating brightness temperature from horizontal and vertical polarizations? This study couples the state propagation model used in Chapter 4 with a radiative transfer model to facilitate brightness temperature assimilation. This is to eliminate the uncertainties caused by the difference in LST data used in the retrieval process and modeled in the assimilation system. The differences between different assimilation strategies is discussed.

Chapter 6 builds on previous chapters and aims to answer one question: Can surface heat flux estimates be improved, if the spatial or temporal resolution of remote sensing soil moisture data is enhanced? This is done by conducting two comparative assimilation cases using soil moisture data sets with finer spatial and temporal resolution, respectively.

Chapter 7 summarizes the key contributions of this PhD research, the knowledge generated, the limitations and prospectives for future research.

2

BASIC ASSIMILATION FRAMEWORK

2.1. INTRODUCTION

IN this dissertation, LST time series and soil moisture information (either in the form of soil moisture data or brightness temperature observations) are assimilated into a coupled heat and water transfer model to estimate surface heat fluxes. The key of this coupling is the tight interaction between soil moisture and latent heat flux: the modeled soil moisture directly influences the evaporative fraction, which determines latent heat flux together with modeled LST, while the estimated latent heat flux serves as the sink term in the soil moisture modeling. Previous studies have focused on assimilating LST time series into heat transfer models to estimate surface heat fluxes, but no studies have coupled the heat and water transer processes to facilitate joint assimilation of both LST and soil moisture information. This chapter introduces the basic framework of the proposed methodology, including the surface energy balance, the coupled heat and water transfer scheme and the data assimilation approach.

2.2. SURFACE ENERGY BALANCE

The flux estimation is fundamentally based on the surface energy balance equation:

$$R_n = H + LE + G \tag{2.1}$$

where R_n [W/m^2] is net radiation, H [W/m^2] is sensible heat flux, LE [W/m^2] is latent heat flux and G [W/m^2] is ground heat flux. H can be calculated from the vertical gradient of temperature between the land surface and the near-surface air by:

$$H = \rho C_p C_H U (T_s - T_a) \tag{2.2}$$

Here ρ [kg/m^3] is air density, C_p [J/kg/K] is specific heat capacity of air, C_H [−] is the bulk coefficient for heat transfer, U [m/s] is wind speed, T_s [K] and T_a [K] are the temperature of land surface and near-surface air (generally measured at 2 meters above the land surface).

C_H is mainly dependent on two factors: the landscape characteristics and the atmospheric stability. As the influence of landscape depends mainly on the surface geometry and the vegetation phenology, it varies slowly over time (e.g., monthly)[Caparrini et al., 2003, 2004a,b; Crow and Kustas, 2005; Sini et al., 2008; Bateni and Liang, 2012; Bateni and Entekhabi, 2012b; Bateni et al., 2013b,a; Xu et al., 2014, 2015]. Here we adopt the stability correction function introduced by Caparrini et al. [2003] to estimate C_H. The stability correction function has proved effective in several studies to estimate surface heat fluxes [Caparrini et al., 2003, 2004a,b; Crow and Kustas, 2005; Sini et al., 2008; Bateni and Liang, 2012; Bateni and Entekhabi, 2012b; Bateni et al., 2013a,b; Farhadi et al., 2014, 2016; Xu et al., 2014, 2015]. The function is given by

$$C_H = C_{HN} \cdot f(R_i) = C_{HN} \cdot (1 + 2(1 - e^{10R_i})) \tag{2.3}$$

where C_{HN} [−] is the C_H under neutral atmospheric condition, which represents the influence of land surface characteristics on surface heat fluxes, and R_i [−] is the Richardson number which is an indicator of the atmospheric stability. R_i is estimated by

$$R_i = \frac{g}{T_{pot}} \frac{\Delta T_{pot}}{\Delta z} (\frac{\Delta z}{\Delta U})^2 \tag{2.4}$$

where g [m/s^2] is gravitational acceleration, T_{pot} [K] is potential temperature, z [m] is vertical height, and Δ represents the difference across height difference Δz. R_i is dependent on atmospheric conditions and exhibits strong diurnal variation. When the atmosphere is unstable, ΔT_{pot} is negative, which leads to a negative R_i, and vice versa. H can be calculated if C_{HN} and R_i are determined.

The EF is introduced to calculate LE. EF is defined as

$$\text{EF} = \frac{LE}{H + LE} \tag{2.5}$$

which renders

$$LE = H \frac{\text{EF}}{1 - \text{EF}} \tag{2.6}$$

The primary assumption is that EF stays almost constant during daytime (09:00-16:00 LT) under clear-sky conditions [Crago, 1996; Crago and Brutsaert, 1996; Gentine et al., 2007]. This way, only one EF estimate is needed to calculate LE at every time step during daytime. This greatly reduces the number of parameters to be estimated, and increases the robustness of the retrieval in the data assimilation applications [Caparrini et al., 2004a].

2.3. COUPLED HEAT AND WATER TRANSFER MODEL

2.3.1. HEAT TRANSFER MODEL

The force-restore model is used to give the time evolution of surface temperature in response to atmospheric forcing and the restoring effect of the deep soil:

$$\frac{dT}{dt} = \frac{2\sqrt{\pi\omega}}{P_e}(R_n - H - LE) - 2\pi\omega(T_s - T_d) + \epsilon_T \tag{2.7}$$

Here P_e [Jm^{-2}K^{-1}s$^{-1/2}$] is the effective thermal inertia, ω [s^{-1}] is the diurnal frequency, T_d [K] is deep soil temperature, and ϵ_T represents model error. This model has been used extensively to characterize heat transfer at the land surface [Caparrini et al., 2003, 2004a,b; Crow and Kustas, 2005; Sini et al., 2008].

2.3.2. WATER TRANSFER MODEL

Soil moisture is modeled using the scheme from the Simple Biosphere (SiB) model [Sellers et al., 1986]. For a soil column divided into n layers, the soil moisture variation is calculated by

$$\begin{cases} \frac{\partial W_1}{\partial t} = \frac{1}{\theta_s D_1}[I_1 - Q_{1,2} - \frac{1}{\rho_w}(E_s + E_{t,1})] + \epsilon_W \\ \frac{\partial W_k}{\partial t} = \frac{1}{\theta_s D_k}[Q_{k-1,k} - Q_{k,k+1} - \frac{1}{\rho_w}E_{t,k}] + \epsilon_W, \quad k = 2...n-1 \\ \frac{\partial W_n}{\partial t} = \frac{1}{\theta_s D_n}[Q_{n-1,n} - Q_n] + \epsilon_W \end{cases} \tag{2.8}$$

Here W_k [−] is the soil wetness of the kth layer, θ_s [m^3/m^3] is saturated soil moisture, I_1 [cm/s] is the infiltration into the first layer from precipitation, D_k [cm] is the thickness of the kth layer, $Q_{k,k+1}$ [cm/s] is the flow between the kth and $k+1$th layer, ρ_w [g/cm^3] is the water density, E_s [$g/cm^2/s$] is the water loss from soil evaporation, $E_{t,k}$ [$g/cm^2/s$] is the water loss from vegetation transpiration in the kth layer, Q_n [cm/s] is the gravitational drainage from the deepest layer, and ϵ_W represents model error. In this dissertation, the soil column is divided into 6 layers, with layer thicknesses of 5, 10, 15, 15, 15, 30 cm, respectively.

W_k is defined as

$$W_k = \frac{\theta_k - \theta_r}{\theta_s - \theta_r} \tag{2.9}$$

where θ_k [m^3/m^3] is the soil moisture of the kth layer and θ_r [m^3/m^3] is the residual moisture.

I_1 is given by

$$I_1 = \min(P_{rate}, K_{sat}) \tag{2.10}$$

where P_{rate} [cm/s] and K_{sat} [cm/s] are precipitation rate and the hydraulic conductivity at saturation.

Following the formulation in Sellers et al. [1986], the water transfer between adjacent layers is given by

$$Q_{k,k+1} = \frac{D_k K_k + D_{k+1} K_{k+1}}{D_k + D_{k+1}}[2\frac{\psi_k - \psi_{k+1}}{D_k + D_{k+1}} + 1], \quad k = 1...n-1 \tag{2.11}$$

where K [cm/s] and ψ [cm] are hydraulic conductivity and soil water potential, which are derived using the Van Genuchten [1980] method.

To implement the scheme, the estimated LE needs to be partitioned into soil evaporation E_s and vegetation transpiration E_t. The partitioning is conducted by assuming

$$\frac{E_t}{LE} = 1 - e^{(c*\mathrm{LAI})} \tag{2.12}$$

Here LAI is leaf area index. The constant c characterizes the radiation extinction by the canopy, which is influenced by the sun angle, plant distribution and the arrangement of leaves [Simunek et al., 2005]. Values suggested for c vary from -0.82 [Campbell, 1985], to -0.5 [Kustas et al., 1996; Anderson et al., 1997] and -0.463 in HYDRUS-1D [Simunek et al., 2005; Sutanto et al., 2012]. Here c is set to -0.5. Sensitivity test demonstrates that small variations of c do not affect flux estimates significantly.

The transpiration water loss from each layer is derived from the overall percentage of available moisture $(\theta_k - \theta_r)$ weighted by root fraction:

$$E_{t,k} = \frac{f_{root,k}(\theta_k - \theta_r)}{\sum_{k=1}^{n} f_{root,k}(\theta_k - \theta_r)} \tag{2.13}$$

where $f_{root,k}$ [−] is the root fraction of the kth layer. The root distribution function adopted is the same as that used in the Community Land Model (CLM) model:

$$Y = 1 - \frac{1}{2}(e^{-r_a d} + e^{-r_b d}) \tag{2.14}$$

where Y is the cumulative root fraction from the surface, and d is soil depth. r_a and r_b are empirical parameters for different vegetation types. Values of 10.74 and 2.608 are assumed for r_a and r_b, as suggested by Zeng [2001].

2.4. DATA ASSIMILATION APPROACH

2.4.1. PARTICLE FILTER

Particle filters have their origin in Bayesian estimation. Unlike the EnKF which directly updates each ensemble based on the Gaussian assumption, the PF instead updates the particle weights based on a likelihood function, and model states are estimated as the weighted average of all particle estimates [Moradkhani et al., 2012; Yan et al., 2015; Dong et al., 2015]. This way the entire distribution of model posterior can be approximated using Monte Carlo sampling.

The evolution of model states in time can be described by

$$\mathbf{x}_t^i = f(\mathbf{x}_{t-1}^i, \mathbf{u}_t^i, \mathbf{b}_t^i) + \mathbf{w}_t^i \tag{2.15}$$

where f is the forward model, $\mathbf{x}_t^i$ is the model state vector of the ith particle at time step t, $\mathbf{u}_t^i$ is the perturbed forcing data, $\mathbf{b}_t^i$ is the model parameter vector, and $\mathbf{w}_t^i$ represents model error. Here $\mathbf{w}_t^i$ is assumed to be normally distributed.

When observations are available, they are related to the true states by

$$\mathbf{y}_t = h(\mathbf{x}_t) + \mathbf{v}_t \tag{2.16}$$

where $\mathbf{y}_t$ is the observation at time step t, $\mathbf{x}_t$ is the state vector, h is the observation operator that translates modeled states to the observations, and $\mathbf{v}_t$ is the observation error.

Initially, the particles are given uniform weight of $1/N$, where N is the particle size. At time step t when assimilation is conducted, the weights are updated by

$$w_t^{i*} \propto w_{t-1}^i p(\mathbf{y}_t | \mathbf{x}_t^i) \tag{2.17}$$

$$w_t^i = \frac{w_t^{i*}}{\sum_{i=1}^{N} w_t^{i*}} \tag{2.18}$$

where w_t^i is the weight of the ith particle, w_t^{i*} is the unnormalized weight from importance sampling, and $p(\mathbf{y}_t|\mathbf{x}_t^i)$ is the likelihood function, which is expressed as

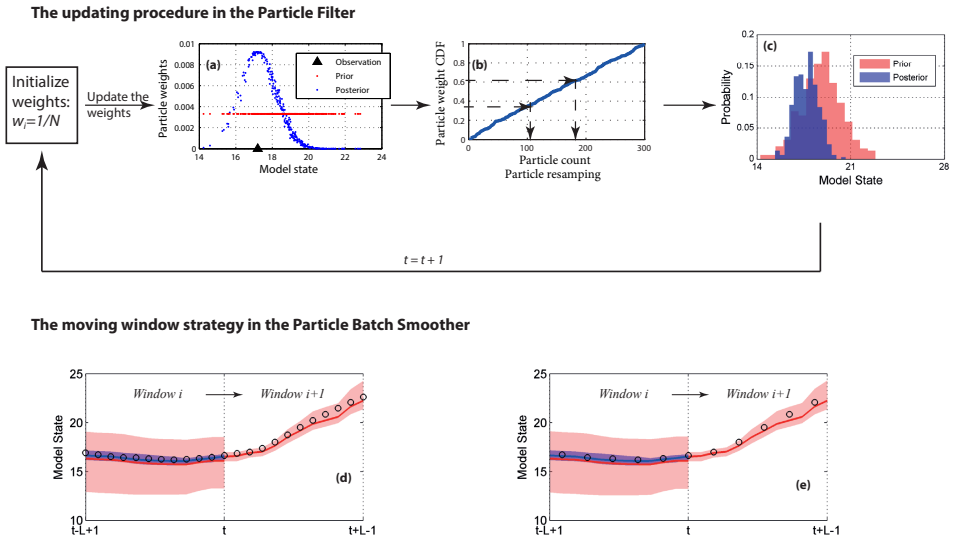

Figure 2.1: A schematic illustration of the updating procedure of the PF (a-c) and the moving window strategy of the PBS (d-e). In (d) and (e), the solid lines are the particle mean of the prior and the posterior, and the shaded areas indicate particle spread. Black circles represent the observations. This figure is modified after Dong et al. [2015].

$$p(\mathbf{y}_t|\mathbf{x}_t^i) \propto e^{\left[-0.5(\mathbf{y}_t-\hat{\mathbf{y}}_t^i)^T\mathbf{R}^{-1}(\mathbf{y}_t-\hat{\mathbf{y}}_t^i)\right]} \tag{2.19}$$

Here $\hat{\mathbf{y}}_t^i$ is the simulated observation of the ith particle, and $\mathbf{R}$ is observation variance.

The updating procedure of the PF is illustrated in Figure 2.1a-2.1c. All particles are given uniform weights initially. When an observation becomes available, the PF updates the weights of particles based on the likelihood function, and particles that yield estimates closer to the observation are given larger weights (Figure 2.1a). Resampling is then performed to avoid particle degeneracy (Figure 2.1b). When the states are updated, the posterior disbribution is generally closer to the observation than the prior distribution (Figure 2.1c).

2.4.2. PARTICLE BATCH SMOOTHER

In this dissertation, the particle batch smoother (PBS) formulations as outlined by Dong et al. [2015] are used to assimilate LST time series. The PBS [Dong et al., 2015; Margulis et al., 2015] can be seen as an extension of the PF. The difference is that the PBS updates model states within an assimilation window in a batch using all available observations in that window, while the PF assimilates observations sequentially.

In the PBS, the likelihood function is given by

$$p(\mathbf{y}_{t-L+1:t}|\mathbf{x}_{t-L+1:t}^i) \propto \prod_{j=t-L+1}^{t} e^{\left[-0.5(\mathbf{y}_j-\hat{\mathbf{y}}_j^i)^T\mathbf{R}^{-1}(\mathbf{y}_j-\hat{\mathbf{y}}_j^i)\right]} \tag{2.20}$$

Here L is the length of the assimilation window, $\mathbf{R}$ is the error covariance matrix of observations, and $\mathbf{y}_j$ is the observation vector.

The moving window strategy of the PBS is illustrated in Figure 2.1d-2.1e. The updating procedure is the same as of the PF, except that the likelihood is calcuated using observations within a time window in a batch. The likelihood is then used to update states within that window. Different observation intervals can be adopted in utilizing the PBS algorithm, as is shown in Figure 2.1d and 2.1e.

As is discussed in Chapter 1, the assimilation performance can greatly deteriorate when particle degeneracy occurs. To avoid this, resampling is conducted after each update. However, for cases when the observations are located on the tail of the prior distribution (e.g., nearly perfect observations or very inaccurate model simulations), resampling alone cannot prevent particle degeneracy [Stordal et al., 2011]. For such cases, the variance of particle weights will be extremely high, giving too much importance to a few particles, while most of the particles will be removed after resampling. As a result, the estimates will be unreliable. This problem also occurs when the dimension of model states is high [Bengtsson et al., 2008]. Stordal et al. [2011] suggested that this problem could be avoided by approximating the posterior with heavy tails. Although biases are introduced in this process, the final estimates are almost surely to converge to the true posterior.

Dong et al. [2016b] introduced a tuning factor β that modified the likelihood function (Equation 2.20) as

$$p(\mathbf{y}_{t-L+1:t}|\mathbf{x}^i_{t-L+1:t}) \propto \prod_{j=t-L+1}^{t} e^{\left[-0.5\beta^2(\mathbf{y}_j-\hat{\mathbf{y}}^i_j)^T\mathbf{R}^{-1}(\mathbf{y}_j-\hat{\mathbf{y}}^i_j)\right]} \tag{2.21}$$

where β ranges from 0 to 1, effectively reducing the variance of the particle weights after updates. Small β values essentially allow the particle spread to be wide enough to encompass the observations within the PBS assimilation window. When $\beta = 1$ is used, the modified likelihood function is reduced to that in Equation 2.20. The optimal value of β depends on the specific application.

3

Estimating Surface Heat Fluxes Using in situ Soil Moisture and Land Surface Temperature Observations

.

This chapter is based on:

Lu, Y., J. Dong, S. C. Steele-Dunne, and N. van de Giesen (2016), Estimating surface turbulent heat fluxes from land surface temperature and soil moisture observations using the particle batch smoother, *Water Resources Research*, 52, 9086–9108, doi:10.1002/2016WR018943.

3.1. INTRODUCTION

CHAPTER 1 summarizes surface heat flux estimation using data assimilation. Previous studies have focused on using variational methods or ensemble Kalman smoothers. The particle batch smoother (PBS) has recently been introduced independently by Margulis et al. [2015] to estimate snow water equivalent and by Dong et al. [2015] to estimate soil moisture. Compared to the PF, the PBS utilizes information contained not only in each individual observation but also in the temporal evolution of a series of observations, as all available observations in the window are assimilated in a batch. This makes the PBS preferable in estimating surface heat fluxes from LST time series.

The PBS is unique in many aspects:

1. Compared to the variational methods [Caparrini et al., 2003, 2004a,b; Sini et al., 2008; Bateni and Liang, 2012; Bateni et al., 2013a,b], the PBS requires no computation of model adjoint or background error covariance, hence it is much easier to implement.

2. Compared to the Kalman filter-based (e.g., EnKF and EnKS) methods [Bateni and Entekhabi, 2012b], the PBS makes no assumptions about the prior distributions, which is theoretically more accurate for hydrological applications in which the prior distributions are often non-Gaussian and the performance of ensemble methods are often suboptimal [Moradkhani et al., 2005; Dong et al., 2015; Yan and Moradkhani, 2016]. It is also better suited to parameter estimation [Dong et al., 2016b], as the PBS tracks the entire prior distribution of parameters using Monte Carlo sampling, which performs more robustly when the Gaussian error assumption is violated [DeChant and Moradkhani, 2012].

Here we will use the PBS to assimilate in situ measured LST and soil moisture data. There are three objectives of this study: (1) to investigate the performance of the PBS in the assimilation of LST observations for surface heat flux estimation; (2) to introduce a soil moisture transfer scheme to constrain EF and jointly assimilate LST and soil moisture observations to improve the poor performance on wet or densely vegetated surfaces; and (3) to explore the influence of LST data availability on flux estimation.

In the first experiment, the PBS is used to estimate surface heat fluxes by assimilating in situ measured LST observations into the force-restore model through a joint state-parameter estimation strategy. This is the first study that adopts the PBS to estimate surface heat fluxes by assimilating LST data.

Although LST time series contains information about surface energy partitioning, many studies have demonstrated that the assimilation strategy performs poorly on wet or densely vegetated surfaces [Caparrini et al., 2004a; Crow and Kustas, 2005; Bateni and Entekhabi, 2012b; Xu et al., 2014]. This happens because under these conditions, the surface energy partitioning becomes more energy-limited, which weakens the constraint of LST on surface energy partitioning [Caparrini et al., 2004a]. Sini et al. [2008] demonstrated that using soil wetness information to constrain EF could improve flux estimation under these conditions. Soil moisture controls the partitioning of available energy into sensible and latent heat fluxes through its influence on evapotranspiration [Entekhabi et al., 1996; Margulis et al., 2002; Koster et al., 2004; Entekhabi et al., 2010; Seneviratne et al., 2010; Crow et al., 2015]. Many studies have demonstrated a positive correlation between EF and soil moisture at different depths [Kustas et al., 1993; Lhomme and Elguero, 1999; Dirmeyer et al., 2000; Basara and Crawford, 2002; Wang et al., 2006; Gentine et al., 2007; Santanello et al., 2011].

In the second experiment, we investigate for the first time in depth the potential value of joint soil moisture and LST assimilation through comparative experiments. A simple soil water transfer scheme is introduced and coupled to the force-restore model, and soil moisture observations are assimilated simultaneously with LST observations. To provide an additional constraint on EF, an EF ~ soil wetness relationship is adopted.

Ultimately, this approach will be used to assimilate LST and soil moisture observations from remote sensing. Potential sources for LST observations include the Advanced Very High Resolution Radiometer (AVHRR), the Moderate Resolution Imaging Spectroradiometer (MODIS), and the Geostationary Operational Environmental Satellites (GOES), among others. However, the estimation robustness may be affected by the number of available LST observations, in addition to the influence of spatial resolution and data accuracy, among others. Typically, the same area is observed no more than twice each day by polar-orbiting satellites, and the observations may fall outside the nominal assimilation window. For geostationary satellites, cloudy-sky conditions which represent more than half of the day-to-day weather [Jin, 2000] can dramatically reduce the amount of available observations. Thus it is necessary to evaluate if the methodology is robust when the LST observations are limited.

In the third experiment, a data-denial experiment is conducted to assess the influence of LST data availability on flux estimates. The model is run multiple times with different numbers of available LST observations. The time of available observations is randomly chosen within the assimilation window to simulate the random occurrence of cloud contamination.

3.2. MATERIALS AND METHODS

3.2.1. STUDY AREA AND DATA

The experiments are conducted using data from the First ISLSCP (International Satellite Land Surface Climatology Project) Field Experiment (FIFE) which took place in the summers of 1987 and 1988 in the prairies in central Kansas [Sellers et al., 1992]. During the experiment, meteorological data were routinely measured with Portable Automatic Meteorological (PAM) stations. LST was measured with a downward-looking radiometer at each PAM station, and surface fluxes were measured at 22 and 10 sites in 1987 and 1988 respectively using either Bowen ratio or eddy-covariance instruments. Considering the data quality and data sampling problems at individual sites [Duan et al., 1996], the site-averaged data sets of 30-min forcing data, LST and surface flux observations provided by Betts and Ball [1998] are used here. This study is comparable to the previous studies using the same data sets [Caparrini et al., 2004a; Crow and Kustas, 2005; Bateni and Entekhabi, 2012b; Bateni and Liang, 2012; Bateni et al., 2013b].

Soil moisture was systematically measured using the gravimetric method for the top 10-cm soil and neutron probes to a depth of up to 2 meters. To generate a FIFE average, Betts and Ball [1998] first averaged measurements at each site, then obtained one daily value for each site, and after that, averaged these values to get a daily FIFE site average. The surface soil moisture (SSM) measured at 5-cm depth is used, and the gravimetric values are converted to volumetric soil moisture by multiplying a bulk soil density of 1.1 g/cm^3 as suggested by Betts and Ball [1998]. Soil texture falls in the texture classes of silty

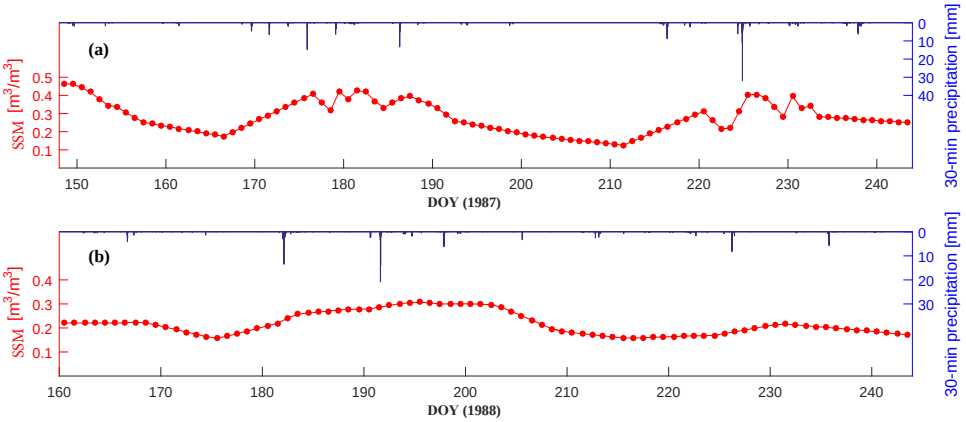

Figure 3.1: 30-min precipitation and daily surface soil moisture (0-5cm) time series of FIFE 87 (a) and FIFE 88 (b).

clay and silty clay loam, and the bulk densities range from 0.96 to 1.5 g/cm^3.

The longest contiguous periods during the FIFE experiment (DOY (day of year) 148-243 for FIFE 87 and 160-243 for FIFE 88) are used for assimilation and validation. To facilitate inter-comparison, the same time periods are adopted as used in previous studies [Caparrini et al., 2004a; Bateni and Liang, 2012; Bateni and Entekhabi, 2012b; Bateni et al., 2013b]. Figure 3.1 shows the time series of the 30-min precipitation data and daily-averaged volumetric soil moisture of the top 5-cm soil of FIFE 87 and 88. The data from the two campaigns are very different. FIFE 87 experienced a very wet initial period and a long dry down (until DOY 166). After that, soil moisture fluctuated with precipitation, and another long dry down ran from DOY 187 to DOY 211. In contrast, during FIFE 88, the soil was in general much drier, and soil moisture responded more slowly to precipitation compared to FIFE 87. It should be noted that soil moisture was sampled less frequently during FIFE 88 [Betts and Ball, 1998], which may reduce the accuracy of the site-average data.

3.2.2. EXPERIMENT SETUP

In this chapter the PBS is used for data assimilation. The model is run for a number of reasonable tuning factors (β), and the β value that minimizes the RMSE of flux estimates is chosen as the optimal value. In this chapter, the optimal β values are 0.8 and 0.5 for the first and the second experiment. In the first experiment, the PBS was used to assimilate LST into the force-restore model to estimate surface fluxes (hereafter PBS$_T$). In the second experiment, a soil moisture transfer scheme was coupled to the force-restore model, and LST and soil moisture data were assimilated simultaneously using the PBS (hereafter PBS$_{T\theta}$). In the third experiment, the first two experiments were run multiple times with different number of available LST observations (1, 2, 3, 4, 5, 10 and 14, respectively). The time of observations was randomly chosen in the assimilation window to simulate the random occurrence of cloud contamination. Offline convergence tests showed that there was only marginal improvement in the RMSE of flux estimates when

Table 3.1: Initial range of C_{HN} for each time period.

FIFE 87		
DOY	Optimal C_{HN}	C_{HN} Range
148-177	8.96×10^{-3}	$(7.96\sim9.96) \times 10^{-3}$
178-206	7.12×10^{-3}	$(6.12\sim8.12) \times 10^{-3}$
207-243	4.60×10^{-3}	$(3.60\sim5.60) \times 10^{-3}$
FIFE 88		
DOY	Optimal C_{HN}	C_{HN} Range
160-190	1.91×10^{-3}	$(0.91\sim2.91) \times 10^{-3}$
191-220	3.76×10^{-3}	$(2.76\sim4.76) \times 10^{-3}$
221-243	3.59×10^{-3}	$(2.59\sim4.59) \times 10^{-3}$

* The optimal C_{HN} values were derived by Caparrini et al. [2004a].

over 100 particles were used in both experiments. As additional particles were not computationally expensive, to ensure sufficient particles for state and parameter estimation, 300 particles were used. Following the approaches of Caparrini et al. [2003, 2004a]; Sini et al. [2008]; Bateni and Entekhabi [2012b]; Bateni and Liang [2012]; Bateni et al. [2013b], the PBS was implemented using a daytime assimilation window (09:00-16:00 LT), during which the EF can reasonably be assumed to be a constant. At the beginning of each time period, the C_{HN} value for each particle was randomly sampled within a given range. Table 3.1 shows the valid ranges for C_{HN} initialization in each time period. The ranges were determined by the 'optimal values' provided by Caparrini et al. [2004a] plus a $\pm$ 1 $\times 10^{-3}$ variation. Caparrini et al. [2004a] determined these 'optimal values' by minimizing the cost function through a variational scheme. The C_{HN} ranges imply considerable uncertainty while maintaining the validity of C_{HN} within a 30-day time period.

PBS WITH ONLY LST (PBS_T)

In the first experiment, P_e was given a constant value of 750 $Jm^{-2}K^{-1}s^{-1/2}$ following Caparrini et al. [2004a] and Sini et al. [2008]. It was shown that variations in P_e did not significantly affect the results [Sini et al., 2008]. T_d was estimated with a semi-diurnal filter of the land surface following Caparrini et al. [2003]. An additive Gaussian error with a standard deviation of 0.1 K was added at each time step.

The soil texture particles were randomly sampled within the two texture classes and bulk density values were sampled from the range shown in Table 3.2. The corresponding hydraulic properties were generated from ROSETTA software [Schaap et al., 2001]. The forcing data in this experiment are net radiation, air temperature and wind speed from the FIFE data sets. Different forms of perturbations have been applied to characterize the error distributions of forcing data [Reichle et al., 2008; Leisenring and Moradkhani, 2011; Dong et al., 2016b]. In this experiment, the forcing data perturbations are described in Table 3.2 following Bateni and Entekhabi [2012b] and Dong et al. [2016b]. To make the perturbation less subjective, approaches such as the variable variance multiplier can be used to dynamically adjust the ensemble spread of the state and parameter predictions in future studies [Leisenring and Moradkhani, 2012].

Table 3.2: Perturbation of forcing data and soil properties

Variable	Perturbation	Standard Deviation	Bound
Silt[%]	Uniform	-	USDA Texture Class
Clay[%]	Uniform	-	USDA Texture Class
Bulk Density [g/cm^3]	Uniform	-	[0.96,1.5]
Net Radiation [W/m^2]	Gaussian,×	0.1 × Net Radiation	-
Air Temperature [K]	Gaussian,+	1	-
Wind Speed [m/s]	Gaussian,+	0.1	-
Precipitation [mm/s]	Gaussian,×	0.1 × Precipitation	-

The model was run from 09:00 to 16:00 local time at 30-min time steps (i.e., 15 time steps per day). Each day at 09:00, the LST particles need to be initialized. Here, the first available observations, typically at 09:00, were used to provide an initial condition for the assimilation window, and a 3 K additive Gaussian error was used following Bateni and Entekhabi [2012b]. If the in situ observations are not available, the particles can also be initialized with data from other sources, such as geostationary satellites, land data assimilation systems, and reanalysis data. For each particle, a daytime average EF was randomly sampled from a uniform distribution with a range of 0.1 to 0.9. At each time step, H was first calculated from Equation 2.2, and LE was derived from H and EF using Equation 2.6. The force-restore model was then used to propagate LST to the next time step.

At 16:00, all available LST observations (14 observations in this experiment) in the daytime window were assimilated using the PBS. The state vector for the ith particle is

$$\mathbf{X} = [T^i_{t1} \quad T^i_{t2} \quad \dots \quad T^i_{tm}] \tag{3.1}$$

Here $t1 \dots tm$ are the time steps when LST observations are available. Particle weights are determined from Equation 2.18. The flux estimates at each time step were calculated as a weighted sum of all particles, and C_{HN} particles were resampled to give the prior estimates for the next day. Results were compared to an open-loop (OL, i.e., no assimilation case) run.

PBS WITH BOTH LST AND θ (PBS$_{T\theta}$)

In the second experiment, the water transfer model from the SiB model is coupled to the force-restore model. The modeled soil moisture data are used in two ways: to constrain daily EF and to serve as a model state in the assimilation. Here the relationship proposed by Dirmeyer et al. [2000] is adopted as

$$\mathrm{EF_{ref}} = \frac{2\mathrm{EF_{max}}}{\pi} arctan(\alpha \mathrm{SWI}) \tag{3.2}$$

where $\mathrm{EF_{ref}}$ [−] is the prior guess of the reference daily EF, $\mathrm{EF_{max}}$ [−] is the maximum possible EF and can be safely assumed to be unity, α [−] is a slope factor that controls the shape of the curve, and SWI is a soil wetness index calculated from field capacity and wilting point based on soil texture. Here SWI was taken as the mean of all particle estimates.

At 09:00 each day, the SWI of each particle was calculated, and a daily reference EF_{ref} was generated using Equation 3.2. The daily average EF of each particle was uniformly sampled within the range of $EF_{ref} \pm \epsilon$. In this experiment, α=4 was used which proves effective to capture the arctangent EF ~ SWI relationship, and ϵ=0.2 was shown to allow a reasonably large and valid range of EF variation.

From 09:00 to 16:00, fluxes are estimated using Equation 2.2 and 2.6, and precipitation data and LE estimates are used to force the water transfer scheme to propagate soil moisture. From 16:00 to 09:00 the next day, LE cannot be derived as EF is no longer conservative. Here G is estimated randomly as a fraction of R_n [Choudhury et al., 1987; French et al., 2003], and LE is calculated as the residual of surface energy balance:

$$G = c_G \cdot u[0,1] \cdot R_n \tag{3.3}$$

where c_G is a coefficient indicating the highest percentage of G in R_n, and $u[0,1]$ represents a random number between 0 and 1. Based on the statistics in Betts and Ball [1998], c_G was assumed to be 0.3. In general, fluxes between 16:00 and 09:00 were relatively low, and test showed that this simple scheme worked reasonably well for flux estimation.

In contrast to PBS_T which requires state initialization every day, LST and θ only need to be initialized once at the beginning of the experiment in $PBS_{T\theta}$. The model was then propagated with perturbed forcing data shown in Table 3.2. At the end of the day, the available LST and SSM observations were assimilated. We only assimilated SSM observations at 5-cm depth, which corresponds to the typical penetration depth of L-band microwave remote sensing observations, such as soil moisture products from SMOS and SMAP. As only daily average SSM was available, the mean modeled θ was calculated as the prior estimate. The state vector for the ith particle is

$$\mathbf{X} = [T^i_{t1} \quad T^i_{t2} \quad \dots \quad T^i_{tm} \quad \frac{\sum_{j=1}^{48} \theta^i_{j,1}}{48}] \tag{3.4}$$

where $t1 \dots tm$ are the time steps when LST observations are available, and $\theta^i_{j,1}$ is the soil moisture of the top layer of the ith particle at time step j. The observation errors for θ was assumed 0.04 m^3/m^3, which is typical for remote sensing observations [Das et al., 2011; Jackson et al., 2012]. During assimilation, LST and θ as well as C_{HN} were resampled and acted as the prior estimates for the next day.

3.3. RESULTS AND DISCUSSION

3.3.1. PBS_T VS. OL

Figure 3.2 shows the estimated daytime average LST from PBS_T and OL versus observations. The three time periods of each campaign are delineated with dash-dot lines. It is evident that the PBS_T captures the temporal trend of LST very well and is always closer to the observations than the OL for both FIFE 87 and FIFE 88. The RMSE decreases from 3.00 K (OL) to 0.81 K (PBS_T) for FIFE 87, and from 4.01 K (OL) to 0.53 K (PBS_T) for FIFE 88. The improvement is more evident for FIFE 88 than for FIFE 87. As the soil is generally much drier in FIFE 88, the surface energy partitioning is more moisture-limited. This makes LST a stronger constraint on surface heat flux partitioning for FIFE 88 than for FIFE 87.

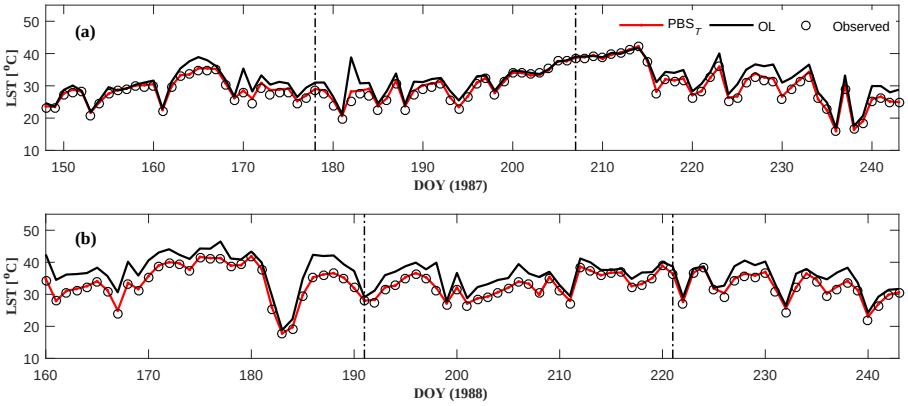

Figure 3.2: Estimated daytime average LST from PBS_T and OL versus observations for FIFE 87 (a) and FIFE 88 (b) with 14 LST observations assimilated.

Figure 3.3 shows the estimated daytime average EF from the PBS_T and OL versus EF calculated from observed turbulent heat fluxes. The three time periods of each campaign are delineated with dash-dot lines. As EF is not constrained in OL simulations, the estimated daily average EFs stay almost constant and deviate a lot from the observations, especially for days when the actual EF is high. In the PBS_T, the estimated EFs capture the daily variations in observed EFs, and the estimated EF values are generally much closer to the observations.

Daily soil moisture observations are also plotted in Figure 3.3 to facilitate analysis. PBS_T performs less satisfactorily for days when the soil is very wet (e.g., DOY 148-177 in FIFE 87) and more accurately for dry-down events (e.g., DOY 200-210 and 230-243 in FIFE 88). For wet soil, the soil moisture is high enough to supply unlimited water for evaporation and transpiration, and the surface energy partitioning is controlled mainly by surface properties and atmospheric conditions [Shokri et al., 2008; Bateni and Entekhabi, 2012b]. Therefore, the coupling between EF and LST becomes very weak, and the estimation of EF from LST is very uncertain. In contrast, during a dry-down event, EF is mainly controlled by soil moisture availability, leaving plenty of information of energy partitioning in LST time series, thus the estimation of EF is more accurate and robust. It is noted that for DOY 199-206 in FIFE 87, the EF estimates capture the decreasing trend but quickly drift away from the observations despite the dry-down event. This is caused by a sharp drop in C_{HN} between time periods. A mean C_{HN} of 7.12×10^{-3} is initially used for DOY 177-206, but C_{HN} quickly drops to 4.31×10^{-3} for DOY 192-221 according to Caparrini et al. [2004a]. This may be caused by the changing vegetation phenology. According to Hall et al. [1992], the LAI quickly fell from about 1.5 to about 0.5 during DOY 180-215 in FIFE 87, which may explain to some extent the dramatic fall of C_{HN}. As is shown in the estimated C_{HN} time series in Figure 3.4, the PBS takes longer to converge to the much lower C_{HN} value, leading to higher H and lower LE estimates, therefore EFs are underestimated. When C_{HN} is initialized reasonably well for the third time period, EF is estimated more accurately (DOY 207).

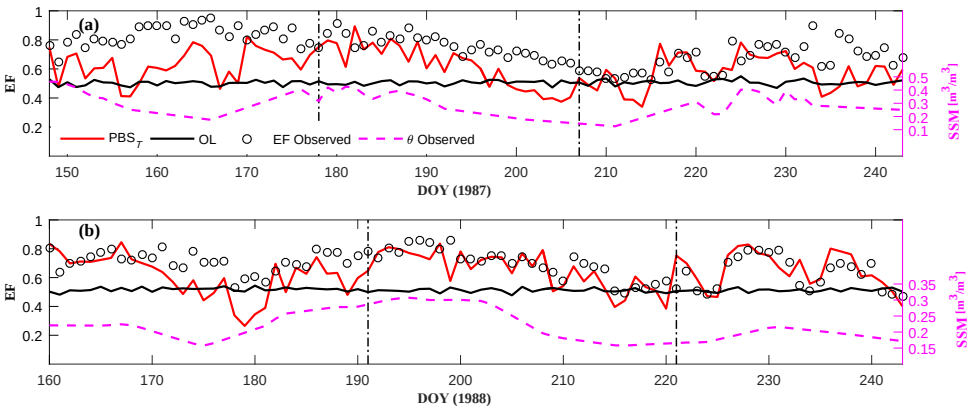

Figure 3.3: Estimated daytime average EF from PBS_T and OL versus observations for FIFE 87 (a) and FIFE 88 (b) with 14 LST observations assimilated. Daily soil moisture observations are plotted in dashed line.

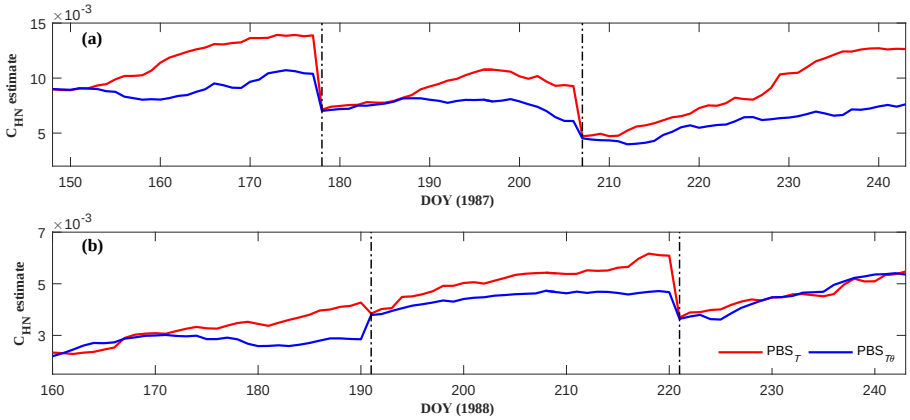

Figure 3.4: C_{HN} estimates from PBS_T and $PBS_{T\theta}$ for FIFE 87 (a) and FIFE 88 (b) with 14 LST observations assimilated.

Figure 3.5 shows the daytime average modeled H and LE versus observations for FIFE 87 and FIFE 88. Generally, significant improvement is seen for all time periods in both campaigns in terms of RMSE and R. The overall RMSEs decrease from 100.7 W/m^2 to 70.7 W/m^2 for H, and from 101.3 W/m^2 to 72.7 W/m^2 for LE in FIFE 87. In FIFE 88, the overall RMSEs decrease from 63.5 W/m^2 to 39.6 W/m^2 for H, and from 103.4 W/m^2 to 56.1 W/m^2 for LE. The statistics are comparable to the results reported in Caparrini et al. [2004a] which also used the force-restore model and variational assimilation. Besides, the improvement in estimation bias is also evident. Overall, the biases decrease from 86.4 W/m^2 to 51.2 W/m^2 for H, and from -89.8 W/m^2 to -47.2 W/m^2 for LE in FIFE 87. In FIFE 88,the overall biases decrease from 45.8 W/m^2 to 8.8 W/m^2 for H, and from -89.9 W/m^2 to -29.7 W/m^2 for LE.

Figure 3.6 shows the 30-min flux estimates versus observations. The estimates at 09:00 are plotted as large open circles and the other estimates as small dots. This is to highlight the fact that some extremely large and negative results are obtained at 09:00, especially in LE estimates. This is caused by the weak hypothesis of constant EF at the very first time step of the assimilation window. In the early morning, LST is sometimes close to or even lower than the air temperature. After particle initialization at 09:00 each day, many particles will have values lower than air temperature. This leads to negative H estimates which are then magnified by the constant EF hypothesis in LE estimation. The same problem was also reported in Caparrini et al. [2004a]. The recalculated RMSE and R excluding estimates at 09:00 are shown in parenthesis. The improvement is also remarkable even at 30-min time scale. When estimates at 09:00 are excluded, the overall RMSEs decrease from 116.9 W/m^2 to 83.6 W/m^2 for H, and from 97.1 W/m^2 to 68.3 W/m^2 for LE in FIFE 87. In FIFE 88, the overall RMSEs decrease from 75.9 W/m^2 to 46.3 W/m^2 for H, and from 104.3 W/m^2 to 58.6 W/m^2 for LE. The reduction in biases is also significant. In FIFE 87, the overall biases decrease from 97.4 W/m^2 to 60.6 W/m^2 for H, and from -82.2 W/m^2 to -33.3 W/m^2 for LE. In FIFE 88, the overall biases decrease from 52.3 W/m^2 to 12.3 W/m^2 for H, and from -87.6 W/m^2 to -24.2 W/m^2 for LE.

3.3.2. $PBS_{T\theta}$ vs. PBS_T

Figure 3.7 shows the daily SSM estimates from OL and $PBS_{T\theta}$ versus observations. Although the sub-daily dynamics are smoothed in the daily area average soil moisture data, improvement on soil moisture estimates after assimilation is still evident, particularly in FIFE 87. After assimilation, the soil moisture time series agrees better with observations. Despite the difference in absolute values, the PBS captures the dry-down events of DOY 148-166 in FIFE 87 and DOY 200-210 in FIFE 88, and the fluctuations during DOY 176-192 in FIFE 87 are captured very well. These improved soil moisture estimates would benefit the estimation of EFs.

A comparison of C_{HN} estimates from PBS_T and $PBS_{T\theta}$ is shown in Figure 3.4. In general, C_{HN} estimates from both strategies follow similar temporal trends. In FIFE 87, the C_{HN} estimates from PBS_T are always higher than those from $PBS_{T\theta}$, which explains the overall underestimation of EFs (Figure 3.3). In FIFE 88, the C_{HN} estimates from both strategies are comparable, particularly in the last time period (DOY 221-243). This implies that LST time series is a strong constraint in surface energy partitioning, which is also demonstrated in the EF estimates shown in Figure 3.3. The temporal evolution of

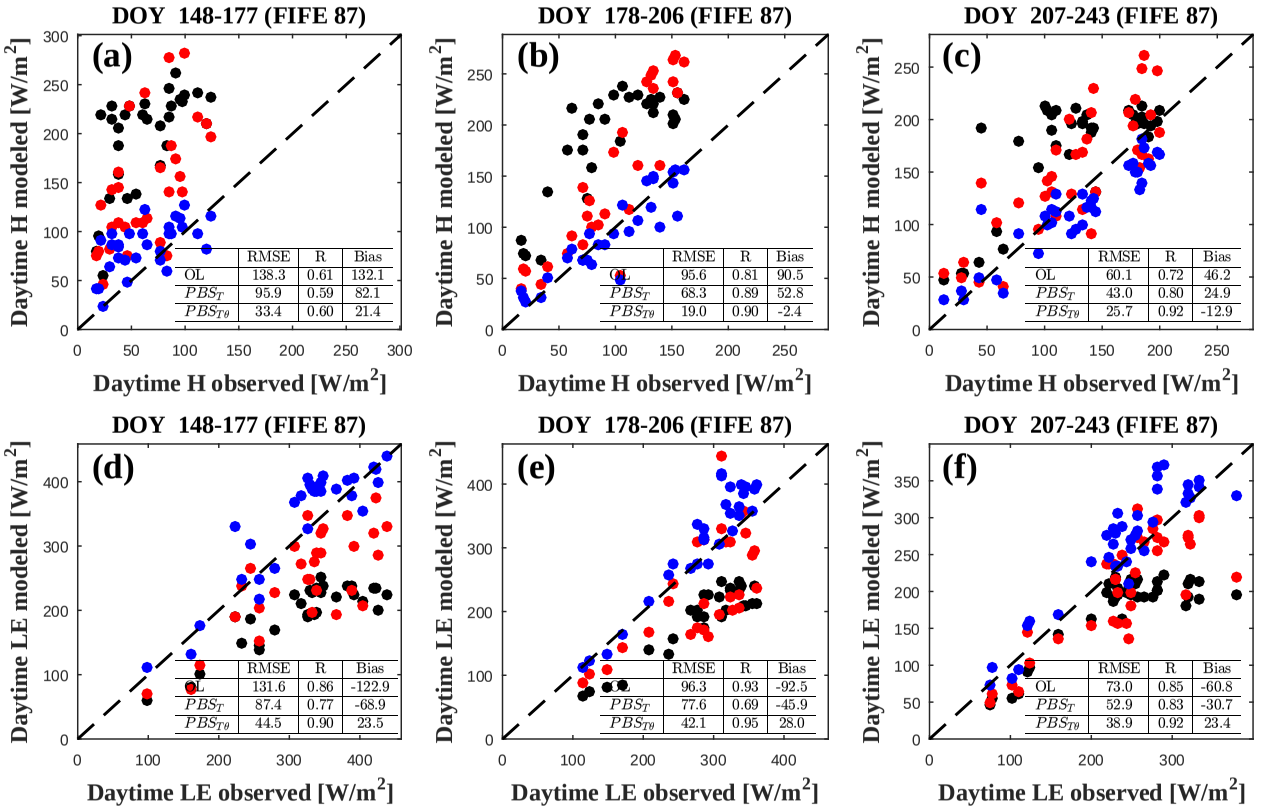

(a)

Figure 3.5: Scatter plot of daytime average modeled fluxes versus observations for FIFE 87 (a-f) and FIFE 88 (g-l) from OL (black), PBS_T (red) and $PBS_{T\theta}$ (blue) with 14 LST observations assimilated. The units of RMSE and bias are W/m^2. The results for the three time periods are plotted separately.

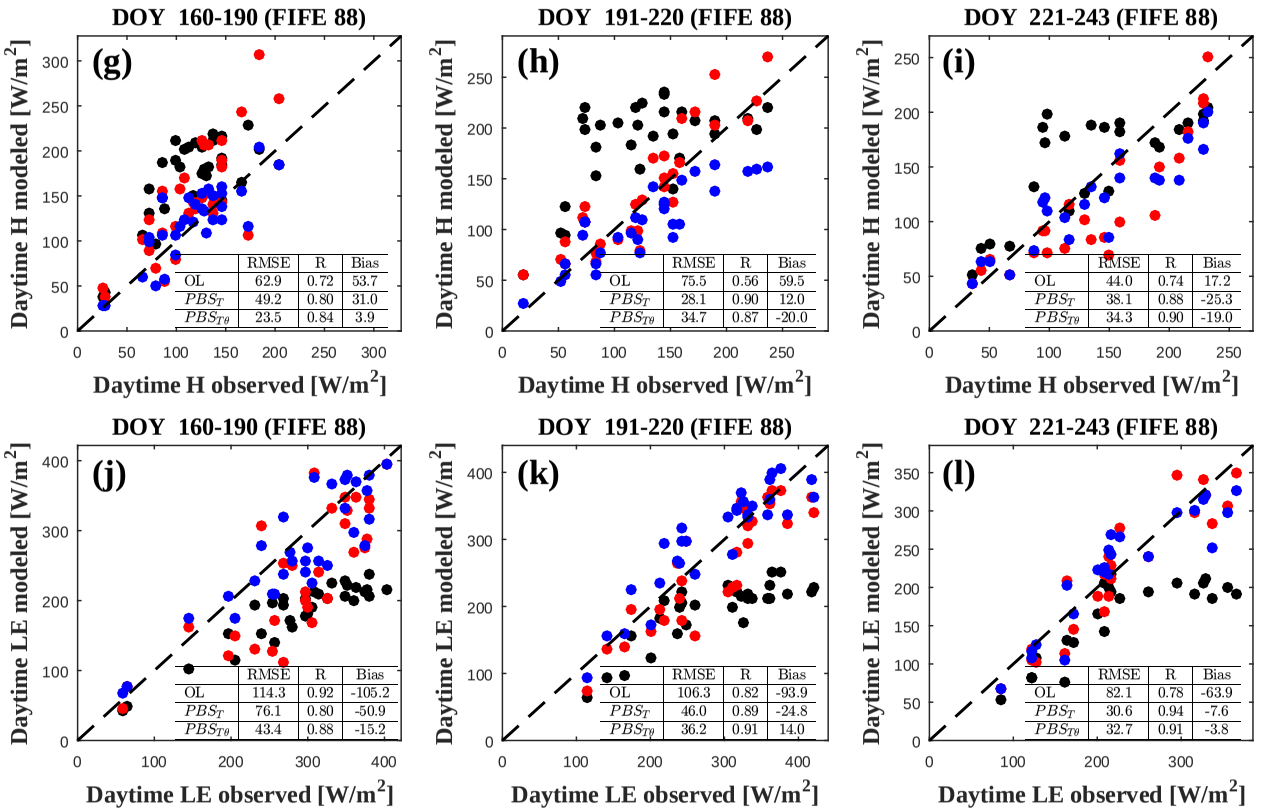

(b)

Figure 3.5: Continued.

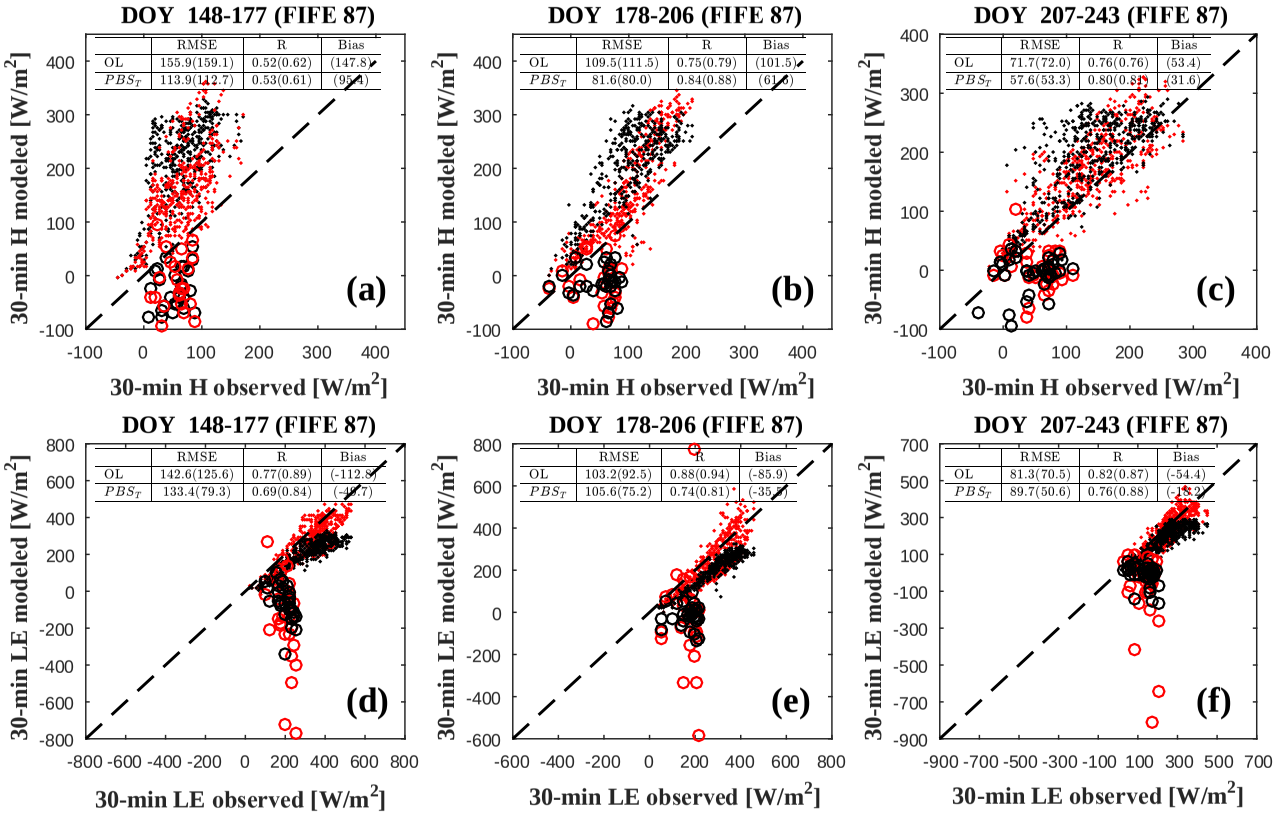

(a)

Figure 3.6: Scatter plot of 30-min modeled fluxes versus observations for FIFE 87 (a-f) and FIFE 88 (g-l) from OL (black) and PBS$_T$ (red) with 14 LST observations assimilated. The units of RMSE and bias are W/m^2. The estimates at 09:00 are plotted in large open circles and the other estimates in small dots. The results for the three time periods are plotted separately.

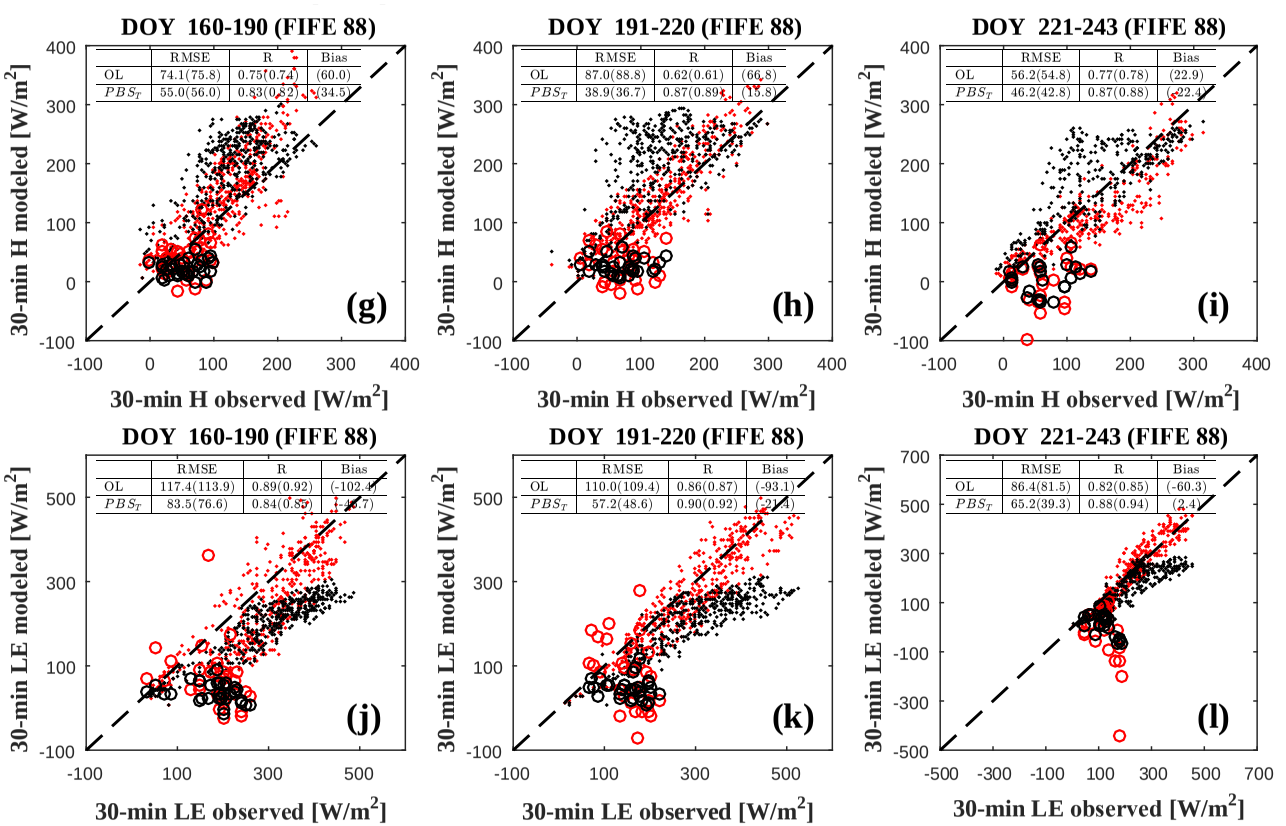

(b)

Figure 3.6: Continued.

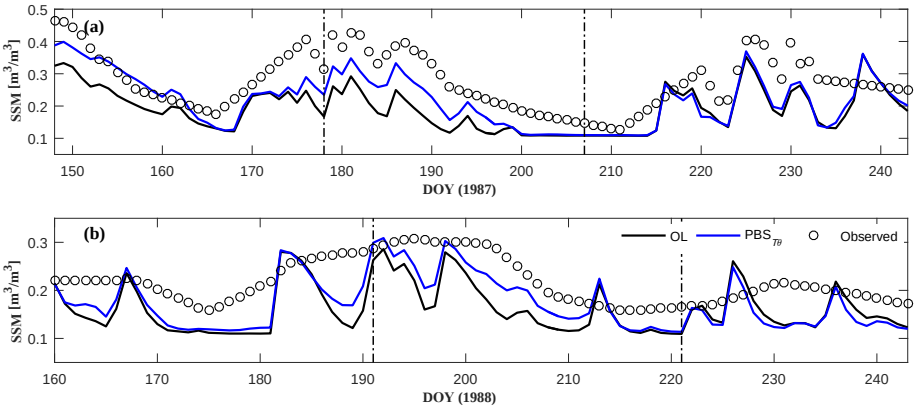

Figure 3.7: Daily SSM estimates from OL and PBS$_{T\theta}$ versus observations for FIFE 87 (a) and FIFE 88 (b) with 14 LST observations assimilated.

C_{HN} can be explained by vegetation phenology. According to Hall et al. [1992], in FIFE 87 the LAI falls first until DOY 160, and then keeps rising until DOY 170-180 followed by a long fall until about DOY 215. After that, LAI gradually rises until DOY 243. The temporal evolution of LAI agrees very well with the C_{HN} estimates from PBS$_{T\theta}$. In FIFE 88, the C_{HN} estimates vary only in a very small range in both strategies compared to FIFE 87. This may be explained by the small variation of LAI (1.2 to 1.4) during FIFE 88 reported in Bateni and Entekhabi [2012b].

Figure 3.8 shows the estimated EFs from PBS$_T$ and PBS$_{T\theta}$. The shaded area indicates the prior guess of the EF range, and the blue and red lines are the estimates from PBS$_{T\theta}$ and PBS$_T$, respectively. Almost all observed EFs fall in the shaded area, showing the validity of the EF ~ SWI relationship. The PBS$_{T\theta}$ estimates are generally much closer to observations, which demonstrates the benefit of assimilating soil moisture observations. In FIFE 87, the improvement is most evident in the first time period (DOY 148-177) when the soil is very wet and for DOY 199-206 when C_{HN} varies strongly. When the soil is wet enough to supply unlimited water, the LST is no longer a strong constraint on energy partitioning. Adding soil moisture assimilation improves EF estimation by forcing relatively high EF values. When C_{HN} varies strongly, the soil moisture estimates prevent sharp fluctuations in EF. This ensures that C_{HN} converges to more realistic values. In FIFE 88, the improvement is most evident in the first time period (DOY 160-190) which features many light rain events. When soil moisture assimilation is performed, EF is constrained to vary within a more reasonable range, which has a great impact on EF and flux estimation.

Daytime average fluxes modeled by PBS$_{T\theta}$ are plotted against observations in Figure 3.5. The most significant improvement over PBS$_T$ is seen in the first two time periods (DOY 148-206) in FIFE 87 and the first time period (DOY 160-190) in FIFE 88 as expected. For other time periods where PBS$_T$ results are already accurate, the benefit of including soil moisture is marginal. The overall RMSEs of H and LE are 26.7 and 41.7 W/m^2 from PBS$_{T\theta}$, compared to 70.7 and 72.7 W/m^2 from PBS$_T$ for FIFE 87. In FIFE 88, the overall

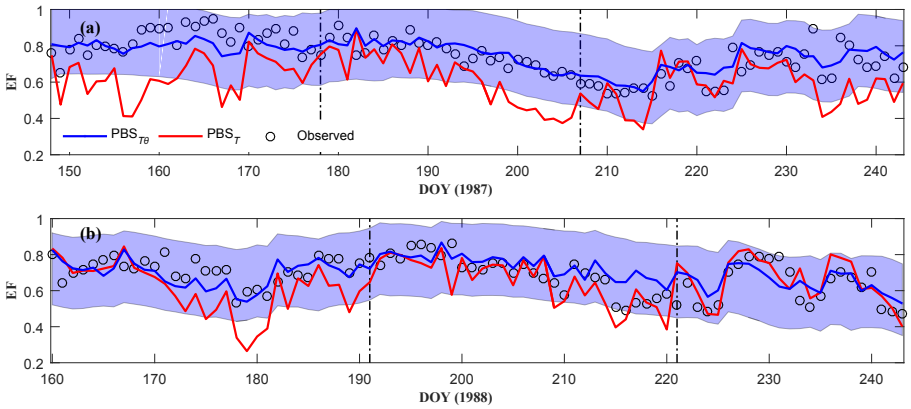

Figure 3.8: Estimated daytime average EF from PBS$_{T\theta}$ and PBS$_T$ versus observations for FIFE 87 (a) and FIFE 88 (b) with 14 LST observations assimilated. The shaded area is the prior guess of valid EF range from PBS$_{T\theta}$.

RMSEs of H and LE are 30.9 and 38.2 W/m^2 from PBS$_{T\theta}$, compared to 39.6 and 56.1 W/m^2 from PBS$_T$. Similarly, the estimation biases are to a large extent improved. The overall bias is reduced from 51.2 and -47.2 W/m^2 for H and LE from PBS$_T$ to 1.0 and 24.8 W/m^2 from PBS$_{T\theta}$ in FIFE 87. In FIFE 88, the the overall bias varies from 8.8 and -29.7 W/m^2 for H and LE from PBS$_T$ to -10.9 and -1.7 W/m^2 from PBS$_{T\theta}$. There is also a small increase in R compared to the results from the PBS$_T$.

Similar to Figure 3.6, the 30-min fluxes from PBS$_T$ and PBS$_{T\theta}$ are plotted against observations in Figure 3.9. One great advantage of PBS$_{T\theta}$ is that the problem of erroneous estimates at 09:00 is to a large extent solved. As LST particles are resampled at the end of the previous assimilation window and then modeled continuously during the night, the particle spread of modeled LST at 09:00 will be smaller compared to randomly generated particles from PBS$_T$. Therefore, it is less likely to result in large negative flux estimates. The decrease of RMSEs is evident when considering the full 09:00-16:00 period. When estimates at 09:00 are excluded, the improvement is more evident in H estimates. The RMSEs for H decrease from 83.6 W/m^2 to 33.7 W/m^2 in FIFE 87 and from 46.3 W/m^2 to 38.5 W/m^2 in FIFE 88. The RMSEs for LE decrease slightly from 68.3 W/m^2 to 63.8 W/m^2 in FIFE 87, and from 58.6 W/m^2 to 52.9 W/m^2 in FIFE 88. Reduction in estimation biases are also dramatic. The overall bias for H decreases from 60.6 W/m^2 to 1.3 W/m^2 in FIFE 87 and from 12.3 W/m^2 to -10.6 W/m^2 in FIFE 88. The overall bias for LE decreases from -33.3 W/m^2 to 27.2 W/m^2 in FIFE 87 and from -24.2 W/m^2 to -0.7 W/m^2 in FIFE 88.

The time series of estimated daytime average flux estimates from the OL, PBS$_T$ and PBS$_{T\theta}$ are compared with the observations as well as R_n for FIFE 87 and FIFE 88 in Figure 3.10. The red and blue shaded areas indicate the particle spread (i.e., the range between minimum and maximum particle estimates) of PBS$_T$ and PBS$_{T\theta}$ estimates. Compared to the results from PBS$_T$, the day-to-day variations of fluxes using PBS$_{T\theta}$ are more consistent with those of observations. The particle spread of both PBS methods varies with the magnitude of R_n. The particle spread gets larger when R_n is high (e.g., DOY 199-200 in FIFE 87), and smaller when R_n is low (e.g., DOY 224 in FIFE 87). Both PBS methods

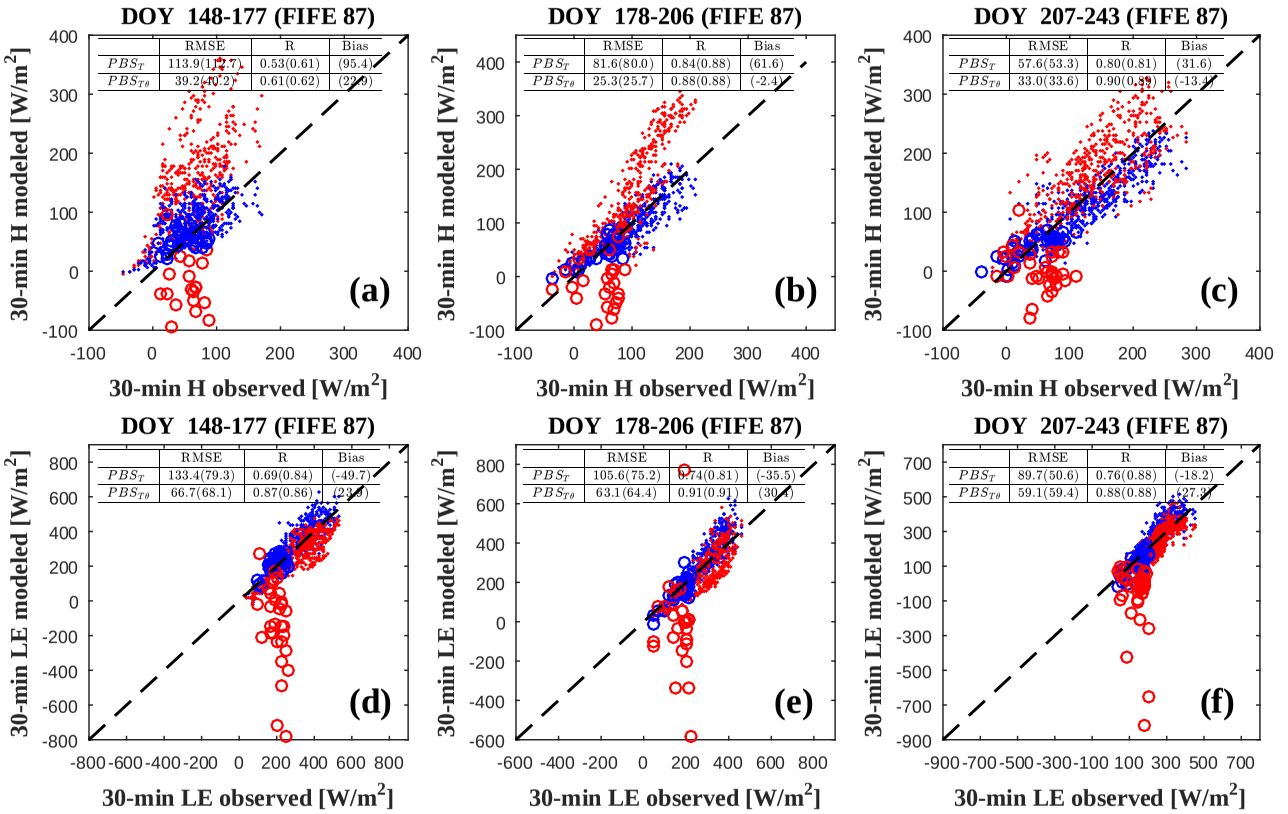

	RMSE	R	Bias
PBS_T	113.9(112.7)	0.53(0.61)	(95.4)
$PBS_{T\theta}$	39.2(40.2)	0.61(0.62)	(27.9)

	RMSE	R	Bias
PBS_T	81.6(80.0)	0.84(0.88)	(61.6)
$PBS_{T\theta}$	25.3(25.7)	0.88(0.88)	(-2.4)

	RMSE	R	Bias
PBS_T	57.6(53.3)	0.80(0.81)	(31.6)
$PBS_{T\theta}$	33.0(33.6)	0.90(0.89)	(-13.4)

	RMSE	R	Bias
PBS_T	133.4(79.3)	0.69(0.84)	(-49.7)
$PBS_{T\theta}$	66.7(68.1)	0.87(0.86)	(23.0)

	RMSE	R	Bias
PBS_T	105.6(75.2)	0.74(0.81)	(-35.5)
$PBS_{T\theta}$	63.1(64.4)	0.91(0.91)	(30.4)

	RMSE	R	Bias
PBS_T	89.7(50.6)	0.76(0.88)	(-18.2)
$PBS_{T\theta}$	59.1(59.4)	0.88(0.88)	(27.3)

(a)

Figure 3.9: Scatter plot of 30-min modeled fluxes versus observations for FIFE87 (a-f) and FIFE88 (g-l) from PBS_T (red) and $PBS_{T\theta}$ (blue) with 14 LST observations assimilated. The units of RMSE and bias are W/m^2. The estimates at 09:00 are plotted in large open circles and the other estimates in small dots. The results for the three time periods are plotted separately.

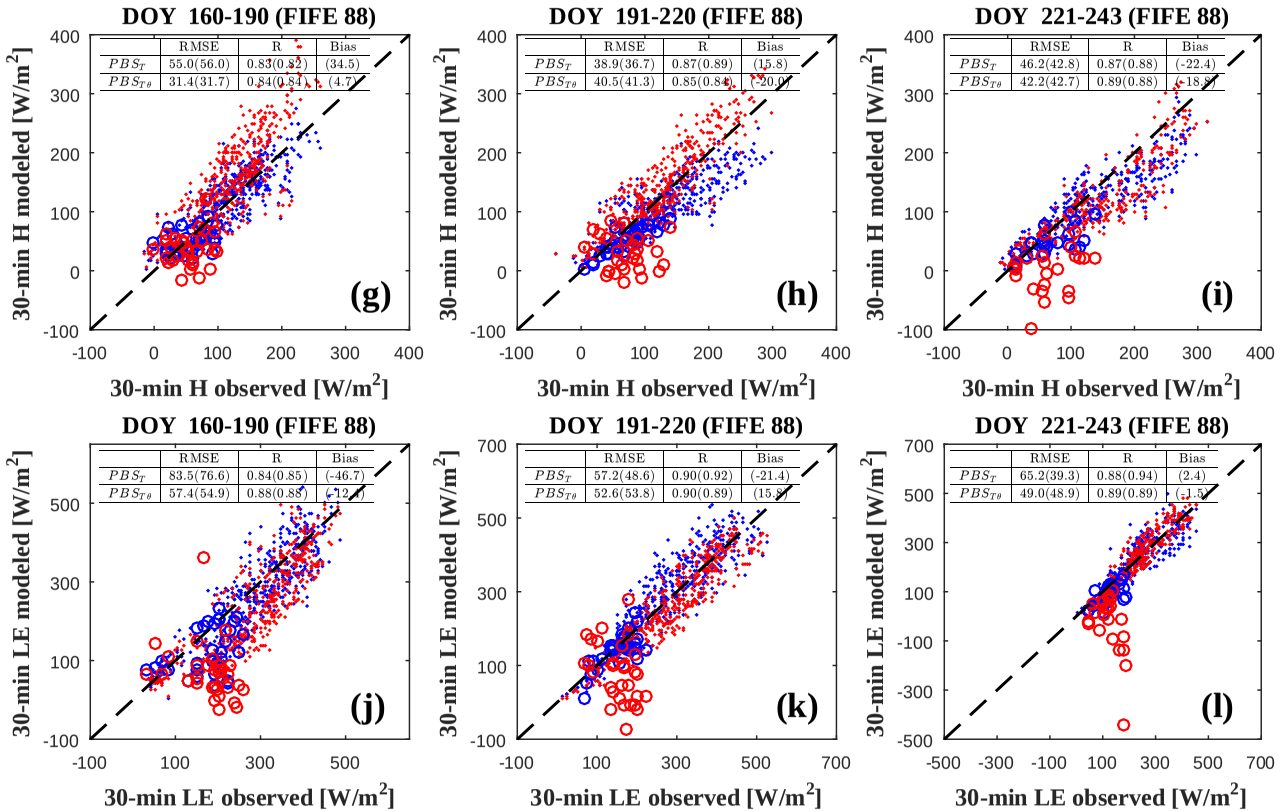

(b)

Figure 3.9: Continued.

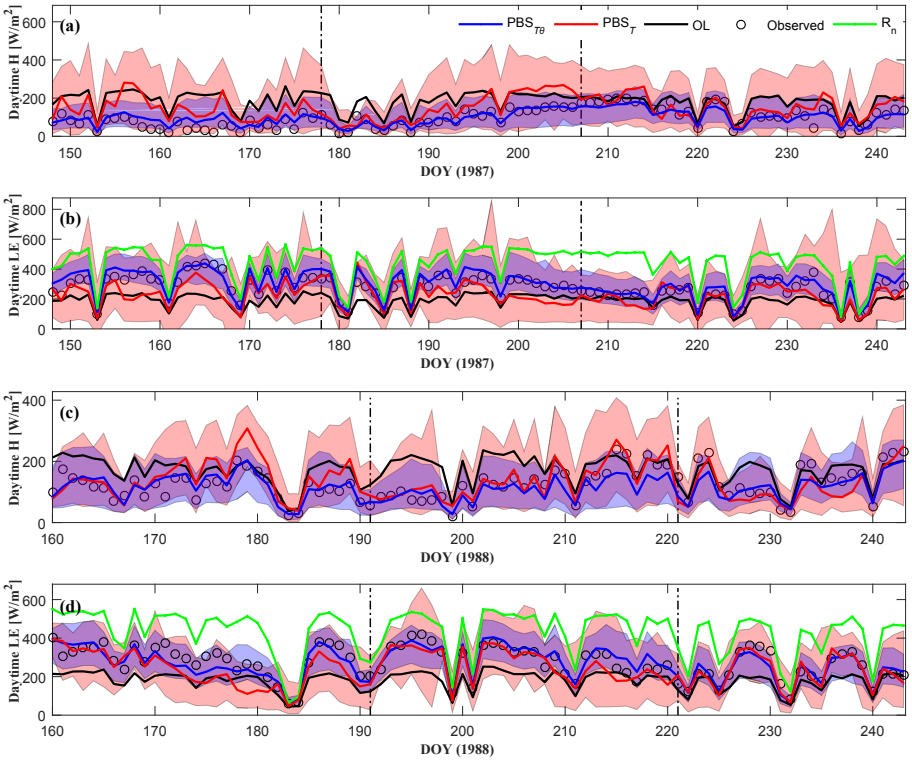

Figure 3.10: Estimated time series of daytime average H and LE from OL, PBS$_T$ and PBS$_{T\theta}$ versus observations and R_n for FIFE 87 (a-b) and FIFE 88 (c-d) with 14 LST observations assimilated. The shaded areas are the particle spread of PBS$_T$ (red) and PBS$_{T\theta}$ (blue).

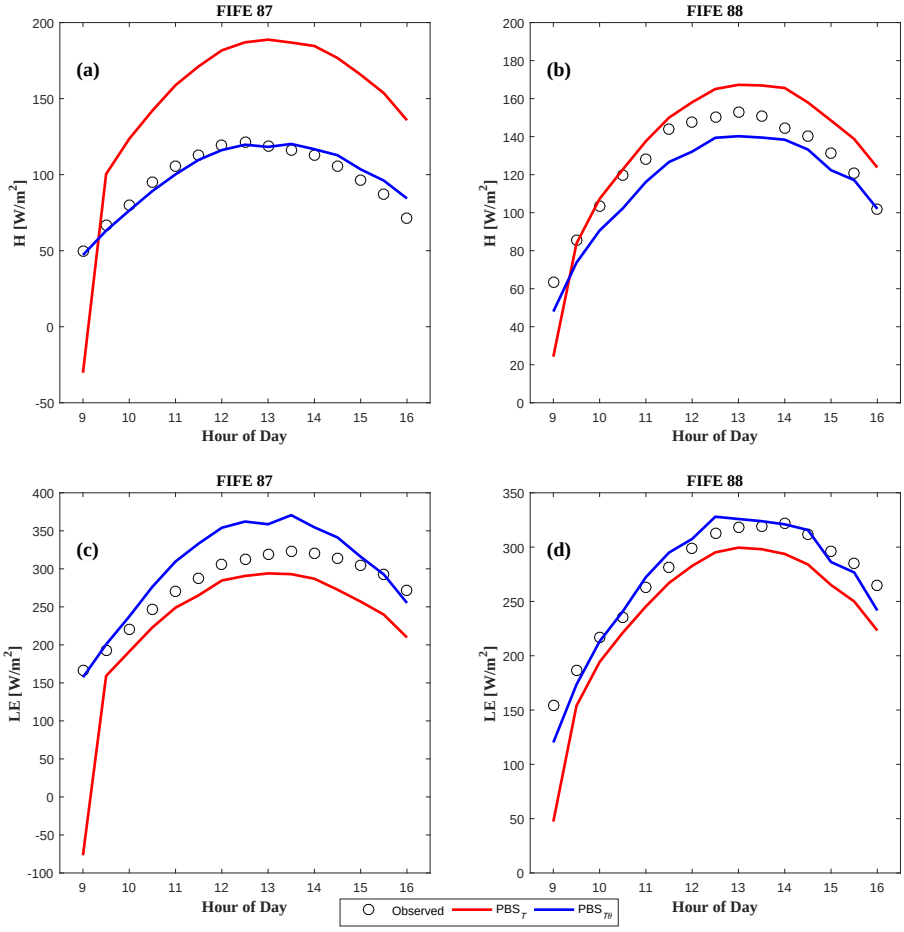

Figure 3.11: Diurnal cycle of average observed and estimated surface heat fluxes for FIFE 87 and FIFE 88 with 14 LST observations assimilated.

provide valid ranges of flux estimates, while the particle spread of $PBS_{T\theta}$ is smaller and more reasonable. Overall, the results show that the assimilation of LST time series with PBS can successfully estimate turbulent heat fluxes, and that introducing soil moisture constraints can improve the estimation, particularly when the surface energy partitioning is energy-limited.

Figure 3.11 shows the mean diurnal cycle of observed and estimated surface heat flux components for FIFE 87 and FIFE 88. In general, PBS_T overestimates H and underestimates LE in both campaigns, and this is also demonstrated by the underestimated EFs in Figure 3.8. $PBS_{T\theta}$ restores the diurnal behavior of surface heat fluxes better, particularly in FIFE 88. An evident deviation from the observations is seen at 09:00 using PBS_T as a result of the outliers at the very first time step of the assimilation window, especially in FIFE 87. When soil moisture is assimilated, this problem is largely solved.

3.3.3. INFLUENCE OF LST AVAILABILITY

Results from the simulation test on LST data availability are shown in Figure 3.12. To eliminate the influence of negative outliers at 09:00, only estimates during 09:30 and 16:00 are used. At the daytime (09:30-16:00 LT) scale, the RMSEs of both H and LE decrease quickly with more available LST observations using PBS_T, particularly when the observations are sparse. When more than five LST observations are available, the benefit of more LST observations becomes less evident. This indicates that the diurnal variation of LST and surface heat fluxes can be restored reasonably well with as few as five LST observations using PBS_T. When soil moisture observations are assimilated, the flux estimates are greatly improved, particularly when LST observations are limited.

The 30-min results from 09:30-16:00 are shown in Figure 3.12e through 3.12h. Similar to the daytime results, the RMSEs decrease quickly with increasing number of LST observations at first, and stay almost constant when over five LST observations are available each day using PBS_T. When soil moisture observations are assimilated, the H estimates are significantly improved. When only one LST observation is available, the RMSEs can be reduced by as much as ~ 70 (~ 20) W/m^2 for H and by ~ 20 (~ 20) W/m^2 for LE in FIFE 87 (FIFE 88). This demonstrates that assimilating soil moisture information greatly enhances the performance of flux estimates even at 30-min scale.

3.4. CONCLUSIONS

A new methodology was developed to estimate surface heat fluxes by assimilating land surface temperature (LST) and soil moisture observations using the particle batch smoother (PBS). The PBS uses all available observations within a window to update states and parameters in that window. The methodology was based on the surface energy balance and aimed to estimate two parameters: a bulk heat transfer coefficient (C_{HN}) which scales the sum of surface heat fluxes, and an evaporative fraction (EF) which represents the partitioning between sensible and latent heat fluxes. Two PBS strategies were implemented in this chapter. First, LST observations were assimilated into the force-restore model using the PBS to estimate surface heat fluxes. Second, to improve the estimation on wet or densely vegetated surfaces, soil moisture was modeled with a simple scheme to further constrain EF, and soil moisture observations were jointly assimilated.

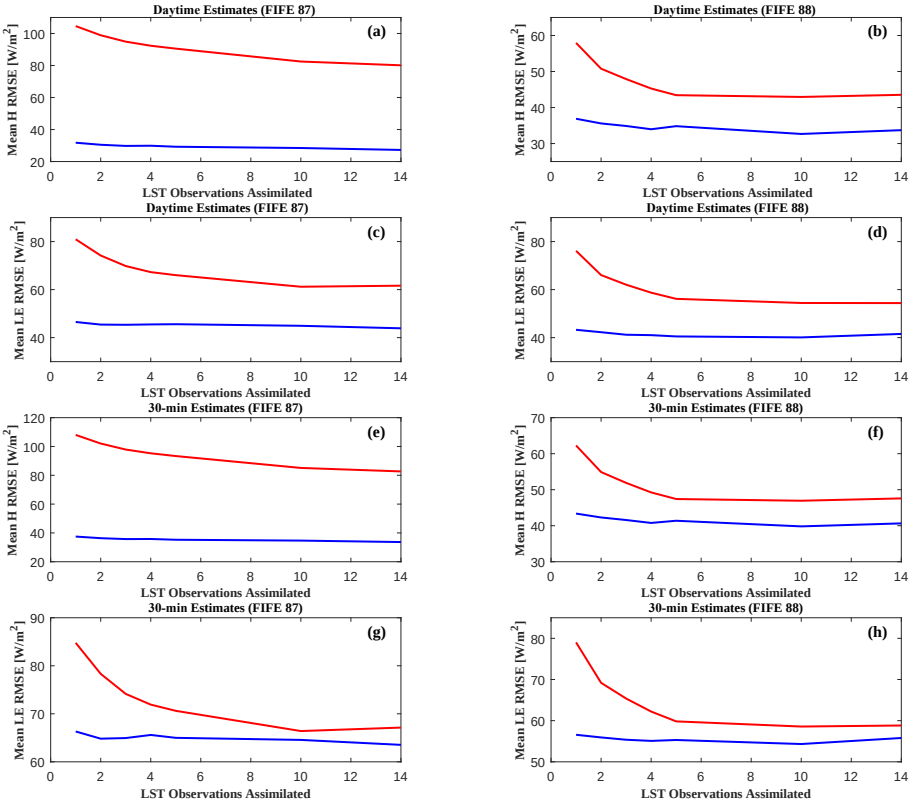

Figure 3.12: Variation of the mean RMSE of flux estimates with available LST observations at daytime and 30-min scales using PBS_T (red) and $PBS_{T\theta}$ (blue).

The methodology was applied with in situ data collected during the FIFE 87 and FIFE 88 experiments. When LST observations are assimilated, the estimated EFs successfully captured the daily variations in observed EFs, and the estimated EF values were much closer to the observations compared to OL results. The RMSEs of flux estimates were significantly reduced at both daytime and 30-min scales. The assimilation results were more accurate for dry-down events and less satisfactory on wet days. When the soil was very wet or densely vegetated, the surface heat flux partitioning became more energy-limited, thus the coupling between EF and LST became weaker, and estimating EF from LST became very uncertain. In contrast, when the soil was dry, the coupling between EF and LST was tight, and LST was a strong constraint on surface heat flux partitioning.

When soil moisture observations were assimilated simultaneously, the EF estimates were greatly improved, particularly for wet days. When the surface was wet or densely vegetated, soil moisture constrained EF by forcing high EF values. The flux estimates were also improved at both daytime and 30-min scales, especially for H estimates. This implies that assimilating soil moisture observations greatly benefits parameter estimation. The time series of daytime flux estimates demonstrated that the day-to-day variations of fluxes were more consistent with observations after assimilating soil moisture observations.

Results from a data-denial experiment showed that increasing the number of LST observations beyond five per day results in only a marginal improvement in the flux estimates. This is instructive in the context of using remote sensing data, in which the availability of observations is severely influenced by cloud cover. When soil moisture observations were assimilated, the flux estimates were significantly improved, particularly when LST observations were sparse.

4

MAPPING SURFACE HEAT FLUXES BY ASSIMILATING SMAP SOIL MOISTURE AND GOES LAND SURFACE TEMPERATURE DATA

.

This chapter is based on:

Lu, Y., S. C. Steele-Dunne, L. Farhadi and N. van de Giesen (2017), Mapping Surface Heat Fluxes by Assimilating SMAP Soil Moisture and GOES Land Surface Temperature Data, *Water Resources Research*, 53, 10858-10877, doi:10.1002/2017WR021415.

4.1. INTRODUCTION

THE previous chapter demonstrated the potential value of joint assimilation of soil moisture and LST observations for flux estimation using in situ data. Here the methodology is improved to be applicable with remote sensing data over a large area. Remote sensing techniques provide global measurements of LST [Sun and Pinker, 2003; Sobrino and Romaguera, 2004; Li et al., 2013] and soil moisture [Entekhabi et al., 2010; Kim et al., 2014; Mladenova et al., 2014], which greatly facilitate large scale surface heat flux mapping. The commonly used soil moisture products are from the Advanced Microwave Scanning Radiometer for Earth observation science (AMSR-E) [Njoku et al., 2003], the Advanced Microwave Scanning Radiometer-2 [Imaoka et al., 2010], the Advanced Scatterometer (ASCAT) [Bartalis et al., 2007], the Soil Moisture and Ocean Salinity (SMOS) [Kerr et al., 2001], and the Soil Moisture Active Passive (SMAP) [Entekhabi et al., 2010]. In particular, the SMAP mission launched in January 2015 provides global coverage of the top 5-cm soil moisture with a spatial resolution of about 36 km every 2-3 days. Various validation studies have suggested that SMAP characterizes the dynamics of soil moisture with a high accuracy [Pan et al., 2016; Cai et al., 2017; Colliander et al., 2017]. Due to the coarse resolution of soil moisture estimates from remote sensing and the spatial heterogeneity of soil moisture, it is unclear if these soil moisture data can effectively constrain EF. In addition, the large spatio-temporal resolution gap between SMAP data and LST data poses a significant challenge for the joint assimilation. For example, LST data from Geostationary Operational Environmental Satellite (GOES) are provided every hour at 0.05° resolution. Furthermore, in situ measurements are generally unavailable to force the model or to calibrate the parameters.

In this chapter, the approach proposed in the previous chapter is developed further by: (1) employing a dual-source (DS) model to characterize the influence from the soil and the canopy, (2) adopting the relationship proposed by Farhadi et al. [2014] to eliminate the need for initial C_{HN} values, (3) assimilating soil moisture data from SMAP and LST data from GOES,(4) bridging the resolution gap using a hybrid particle assimilation strategy, (5) using forcing data independent of ground measurements, and (6) making the strategy calibration-free (surface heat flux observations are not required to calibrate the tuning factor in assimilation) using an adaptive approach.

This chapter aims to answer the following questions: (1) Can surface heat fluxes be improved by assimilating SMAP soil moisture and GOES LST data? (2) How can the spatial and temporal resolution between the data sets be bridged? (3) What is the added value of the SMAP soil moisture data to flux estimation?

4.2. MATERIALS AND METHODS

4.2.1. DUAL-SOURCE MODELING

The dual-source (DS) SEB scheme, as shown in Figure 4.1 was first introduced by Norman et al. [1995] and Kustas et al. [1996]. In the DS scheme, the land surface is characterized as a mixed layer of soil and vegetation canopy, and the energy balance is constructed for soil and canopy respectively. The surface heat fluxes are calculated as weighted combination of the contributions from both sources. The net radiation for soil (R_{ns}) is partitioned into sensible heat flux (H_s), latent heat flux (LE_s) and ground heat flux (G) by

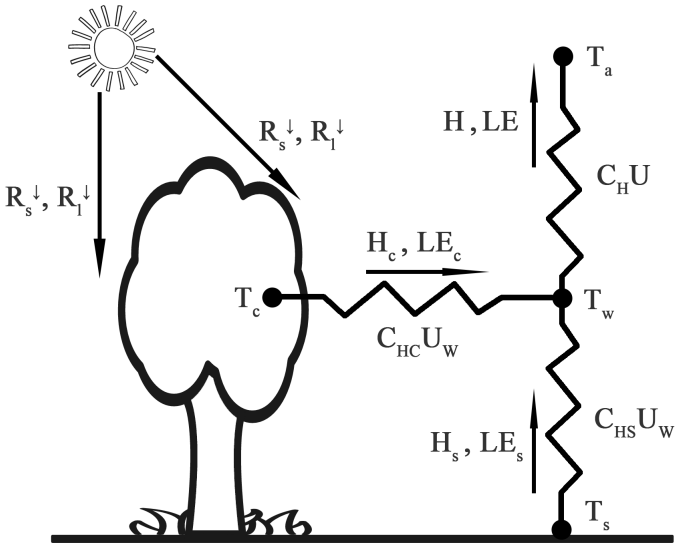

Figure 4.1: Schematic diagram of the dual-source (DS) surface energy balance scheme.

$$R_{ns} = H_s + LE_s + G \tag{4.1}$$

The heat storage in the canopy is ignored, and the net radiation for canopy (R_{nc}) is partitioned into sensible (H_c) and latent (LE_c) heat fluxes

$$R_{nc} = H_c + LE_c \tag{4.2}$$

The total fluxes are calculated by the contribution of the fluxes from soil and canopy, weighted by the respective fractional cover

$$H = f_c H_c + (1 - f_c) H_s \tag{4.3}$$

$$LE = f_c LE_c + (1 - f_c) LE_s \tag{4.4}$$

where f_c [-] is the canopy cover fraction calculated from LAI following a semi-empirical relationship [Choudhury, 1987; Norman et al., 1995; Caparrini et al., 2004b] by

$$f_c = 1 - \exp(-0.5 \cdot \text{LAI}) \tag{4.5}$$

The net radiation for soil and canopy are calculated by building a balance between incident shortwave ($R_s^{\downarrow}$) and longwave ($R_l^{\downarrow}$) radiation and the corresponding outgoing radiation for each component

$$R_{ns} = (1 - alb_s)\, R_s^{\downarrow} + R_l^{\downarrow} - \varepsilon_s \sigma T_s^4 \tag{4.6}$$

$$R_{nc} = (1 - alb_c)\, R_s^{\downarrow} + R_l^{\downarrow} - \varepsilon_c \sigma T_c^4 \tag{4.7}$$

where alb_s [-] and alb_c [-] are the surface albedo of soil and canopy, ε_s [-] and ε_c [-] are the soil and canopy emissivity, and σ [W/m^2/K^4] is the Stefan-Boltzmann constant.

The conductances for heat transfer between soil and air within the canopy and between canopy and air within the canopy are represented by C_{HS} and C_{HC}, respectively following Caparrini et al. [2004b]. H_s and H_c are given by

$$H_s = \rho C_p C_{HS} U_w (T_s - T_w) \tag{4.8}$$

$$H_c = \rho C_p C_{HC} U_w (T_c - T_w) \tag{4.9}$$

where T_s [K] and T_c [K] are soil and canopy temperature, T_w [K] and U_w [m/s] are the air temperature and wind speed at a reference height within the canopy volume.

Assuming an exponential decay of conductance within the canopy, Caparrini et al. [2004b] proposed an approach to calculate $C_{HS}U_w$ and $C_{HC}U_w$ from $C_H U$ by

$$\begin{cases} K_H = C_H U \\ K_{HS} = C_{HS} U_w = K_H \exp(-0.6 \cdot \mathrm{LAI}) \\ K_{HC} = C_{HC} U_w = K_H \exp(-0.3 \cdot \mathrm{LAI}) \end{cases} \tag{4.10}$$

C_H is calculated from C_{HN} using Equation 2.3. Following Farhadi et al. [2014], C_{HN} is estimated by

$$C_{HN} = exp(a + b \cdot \mathrm{LAI}) \tag{4.11}$$

where a and b represent the surface control on energy fluxes from the soil and vegetation density, respectively.

H can also be calculated using C_H for the heat transfer between air within the canopy and air above the canopy by

$$H = \rho C_p C_H U (T_w - T_a) \tag{4.12}$$

The equation for T_w retrieval can be derived by solving Equation 4.3, 4.8, 4.9, 4.10 and 4.12:

$$T_w = \frac{1}{K_H + (1 - f_c) K_{HS}} \left[\frac{f_c (1 - \mathrm{EF_c})}{\rho C_p} R_{nc} + K_H T_a + (1 - f_c) K_{HS} T_s \right] \tag{4.13}$$

Likewise, T_c can be obtained as

$$T_c = \frac{\left[(1 - alb_c)\, R_s^{\downarrow} + R_l^{\downarrow} + 3\varepsilon_s \sigma T_a^4 \right] (1 - \mathrm{EF_c}) + \rho C_p K_{HC} T_w}{4\varepsilon_s \sigma T_a^3 (1 - \mathrm{EF_c}) + \rho C_p K_{HC}} \tag{4.14}$$

Here, $\mathrm{EF_s}$ and $\mathrm{EF_c}$ are the evaporative fraction for soil and canopy, respectively.

To constrain EF_s and EF_c with modeled soil moisture, the relationship proposed by Dirmeyer et al. [2000] is improved to apply to the soil and canopy separately:

$$EF_s^{ref} = \frac{2EF_{max}}{\pi} arctan(\alpha_s \cdot SWI_s) \tag{4.15}$$

$$EF_c^{ref} = \frac{2EF_{max}}{\pi} arctan(\alpha_c \cdot SWI_c) \tag{4.16}$$

where EF_s^{ref} and EF_c^{ref} are the reference daytime EF values estimated from the corresponding soil wetness indices (SWI). EF_{max} is the maximum possible EF and is assumed to be unity [Lu et al., 2016]. α_s and α_c are slope factors that control the shape of the curve and will be estimated during the assimilation. When the reference EF is determined, the prior guess of daytime EF is uniformly sampled within a ±0.2 range following Lu et al. [2016].

EF_s is assumed to be dependent only on the wetness condition of the surface soil (θ_1), and EF_c is assumed to be affected by the total transpirable water of the soil column (θ_{col}):

$$SWI_s = \frac{\theta_1 - \theta_r}{\theta_s - \theta_r} \tag{4.17}$$

$$SWI_c = \frac{\theta_{col} - \theta_{wp}}{\theta_{fc} - \theta_{wp}} \tag{4.18}$$

where θ_s and θ_r are saturated and residual soil moisture, while θ_{fc} and θ_{wp} are field capacity and wilting point. θ_{col} is the mean soil moisture of all layers weighted by root fractions proposed by Zeng [2001].

4.2.2. STUDY AREA AND DATA

The developed methodology is tested over an area in the US Southern Great Plains as illustrated in Figure 4.2. The major part of the study area (35.75°N to 37.24°N, 96.72°W to 98.21°W) is in Oklahoma and a small portion is in Kansas. The area is mostly flat with elevation ranging from about 230 m to 450 m above sea level. The area is covered by 4 × 4 SMAP soil moisture grid cells, or 30 × 30 GOES LST grid cells. The major land cover types are grassland and cropland according to ESA CCI (Climate Change Initiative) land cover data set (v1.6.1). The main soil texture classes are silt loam and sandy loam, and the soil hydraulic properties are estimated from soil texture data using ROSETTA software [Schaap et al., 2001]. 30-min in situ flux measurements are available from four Energy Balance Bowen Ratio (EBBR) flux stations provided by the Atmospheric Radiation Measurement (ARM) network. Hourly soil moisture measurements at the depths of 5, 10, 20, 50 and 100 cm are obtained at two stations: Abrams from the Soil Climate Analysis Network (SCAN; Schaefer et al. [2007]) and Stillwater from the US Climate Reference Network (USCRN; Bell et al. [2013]).

Precipitation forcing data are obtained from Global Precipitation Measurement (GPM) [Hou et al., 2014] 3IMERGHH product. The data set provides multi-satellite precipitation estimates with gauge calibration which are available every 30 minutes at a spatial resolution of 0.1° [Huffman et al., 2015]. Other atmospheric forcing data ($R_s^{\downarrow}$, $R_l^{\downarrow}$, T_a, U and

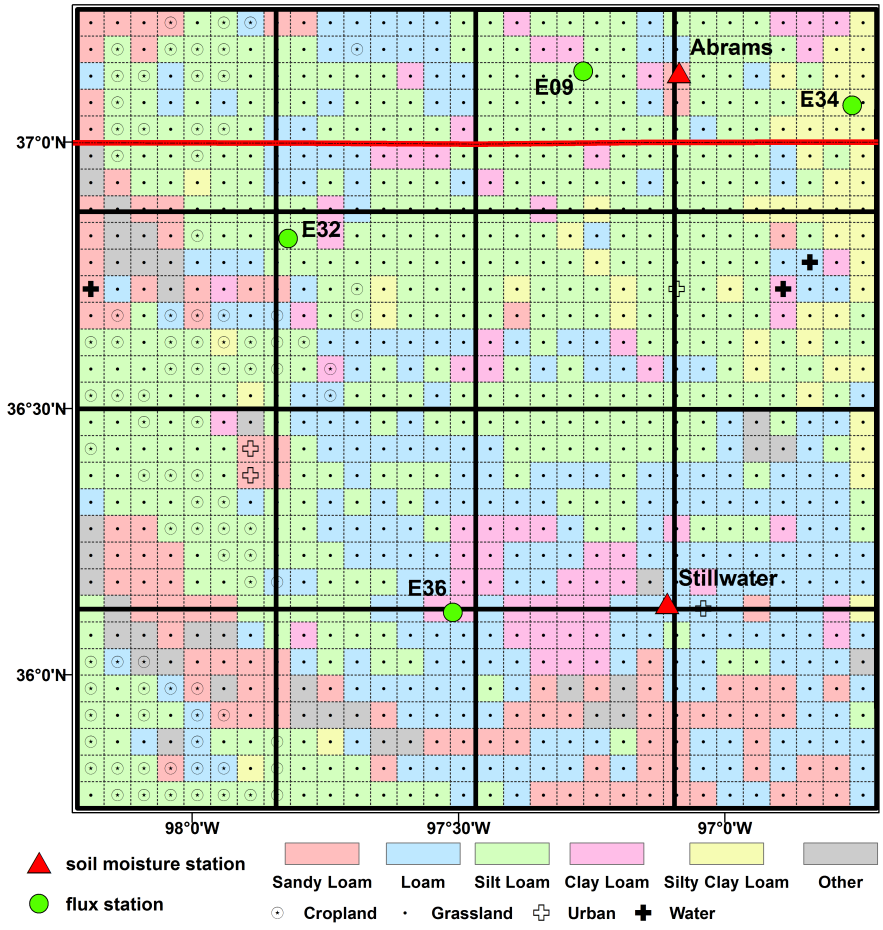

Figure 4.2: Stations and dominant soil types and land cover for each pixel in the study area. The thick black grids represent SMAP soil moisture grids, while the thin dashed grids represent GOES LST grids. The thick red line demarcates the border between Kansas and Oklahoma.

Table 4.1: Summary of data sets.

Category	Source	Data Set	Original Resolution	
			Spatial	Temporal
Forcing	NLDAS-2	$R_s^{\downarrow}, R_l^{\downarrow}, U, T_a, P_a$	0.125°	1 h
	GPM	P	0.1°	30 min
Ancillary	NSIDC	soil texture	3 km	-
	MODIS	LAI	1 km	8 days
Assimilation	SMAP	soil moisture	36 km	2-3 days
	GOES	LST	0.05°	1 h

air pressure (P_a)) are provided by the North American Land Data Assimilation System project phase 2 (NLDAS-2) Forcing File A [Xia et al., 2012]. The majority of forcing data are interpolated from the North American Regional Reanalysis (NARR), and are provided hourly at 0.125° resolution.

Soil texture data, including sand fraction, clay fraction and bulk density data are also used for SMAP soil moisture retrieval [Das, 2013], and are obtained from the National Snow and Ice Data Center (NSIDC) . These data sets are provided at 3-km resolution. LAI data are extracted from the Moderate Resolution Imaging Spectroradiometer (MODIS) MCD15A2 product [Knyazikhin et al., 1999]. The data are available at 1 km resolution every 8 days.

The SMAP soil moisture data used for assimilation are the Level-3 soil moisture data (L3_SM_P) retrieved from the L-band radiometer. The data are posted on 36 km EASE-2 (Equal-Area Scalable Earth-2) grids, with a typical revisit interval of 2-3 days [Entekhabi et al., 2014]. The data are acquired and mapped to geographic coordinates from https://reverb.echo.nasa.gov/.

GOES LST data are provided by Copernicus Global Land Service (http://land.copernicus.eu/global/). The LST data are generated from infrared data from a collection of geostationary satellites covering different areas to provide global coverage [Freitas et al., 2013]. The data are provided hourly at 0.05° resolution.

4.2.3. BIAS CORRECTION FOR SMAP SOIL MOISTURE

An assumption for data assimilation systems is unbiased observations and forecasts. However, the remote sensing observations and the model simulations often reveal different climatologies, in terms of long-term mean or variability [Reichle and Koster, 2004; Reichle et al., 2004]. This may be caused by the limitations of the model (e.g., imperfect structure, simplifications, sub-optimal parameters) [De Lannoy et al., 2007b] or nonuniform representation of land surface variables of the remote sensing system (e.g., shallower (<5 cm) observed depth of soil moisture) [Sahoo et al., 2013], among others. The difference in climatology can be even more dramatic for the direct brightness temperature observations [Kornelsen et al., 2015]. A common practice is to correct for the bias prior to data assimilation. Generally, bias correction methods focus on correction of the first-order moment (the long-term mean) [Sahoo et al., 2013; De Lannoy and Reichle, 2016a,b], the first two moments (mean and standard deviation) [Crow et al.,

2005; Kumar et al., 2012], or higher moments (the distribution, often through cumulative distribution function (CDF) matching) [Reichle and Koster, 2004; Lievens et al., 2016]. More sophisticated methods have also been proposed [Yilmaz and Crow, 2013; Kornelsen and Coulibaly, 2015; Su and Ryu, 2015]. There is not a simple 'optimal' bias correction method for a large range of applications, and the appropriate bias correction scheme is application dependent.

Previous studies have suggested that SMAP surface soil moisture data may be biased [Zeng et al., 2016; Colliander et al., 2017]. Before assimilation, bias correction is performed using CDF matching between the observations and simulations for each SMAP grid cell separately to reconcile the differences in long-term mean, variance and higher moments [De Lannoy and Reichle, 2016a].

The LST data however, are directly assimilated into the force-restore model without bias correction following previous studies [Bateni et al., 2013a]. One concern is that the bias between modeled and observed LST data can be caused by not only the climatological differences between the model simulations and the observation system, but also by the uncertainties of initial parameter ranges at local scale. Hence prior scaling may disturb the diurnal variations of LST evolution, and degrade the algorithm performance in updating parameters [Lu et al., 2017]. A summary of the data sets is provided in Table 4.1, and all data are converted to geographic coordinates.

4.2.4. HYBRID PARTICLE ASSIMILATION STRATEGY

Since SMAP soil moisture data and GOES LST data are provided at different spatial and temporal resolution, a hybrid particle assimilation strategy is adopted. The rationale is that SMAP soil moisture observations are a 'snapshot' of the instantaneous land surface state, and are only available every 2-3 days. Hence a filter is better suited to update the instantaneous soil moisture state. On the other hand, the information of surface energy partitioning can be revealed from the temporal evolution of LST during the daytime window rather than each individual observation, therefore smoothing is more appropriate than filtering. Here the SMAP soil moisture observations are assimilated using the particle filter (PF) at SMAP descending overpass time (06:00 LT) to update soil moisture, and all available GOES LST data between 09:00 and 16:00 are assimilated using an adaptive particle batch smoother (APBS) at the end of the daily assimilation window (16:00 LT) to update LST as well as the parameters.

PARTICLE FILTER FOR SOIL MOISTURE ASSIMILATION

At the SMAP descending overpass time (06:00 LT), SMAP soil moisture data are assimilated if available. Since SMAP soil moisture data are much coarser than the model grids, an averaging operator is used, which essentially averages the predicted surface soil moisture from the model so that they can be compared to the coarser resolution observations. First, all the model grid cells within a SMAP grid cell are found. Second, for each model grid cell, the particles are sorted based on the soil moisture of the first layer (i.e., the first particle is the wettest and the last particle is the driest). Finally, the particles from all the model grid cells within a SMAP grid cell are grouped based on their ranking (i.e., the first group contains all the particles which rank first), and the simulated 'observation' of this group is generated using an averaging operator

$$\widehat{\mathbf{y}}_t^i = \frac{\sum_{j=1}^{M} \theta_{j,1,t}^i}{M} \tag{4.19}$$

where M is the number of model grid cells within a SMAP grid cell, and $\theta_{j,1,t}^i$ is the surface soil moisture of the ith particle in jth model grid at time step t. The SMAP observation error is assumed to be 0.04 m^3/m^3 [Chan et al., 2016; Colliander et al., 2017; Cai et al., 2017], and soil moisture profile is updated after assimilation. It is worth noting that the SMAP observation error used is the nominal value at the original 36-km scale, and is prone to influence from soil texture, vegetation water content and surface heterogeneity. Furthermore, the actual observation error should be greater when the coarse soil moisture data are used to update simulations at finer resolution. Soil moisture estimates may be improved if locally more realistic observation error is available.

APBS FOR LST ASSIMILATION

The APBS was improved by Dong et al. [2016a] from the PBS. In the PBS, a tuning factor is estimated using in situ observations to prevent particle degeneracy. This is improved in the APBS by determining the tuning factor automatically in an adaptive manner. Estimating the tuning factor adaptively in the APBS eliminates the dependence on in situ observations and is more appropriate for large scale applications using remote sensing data.

In the APBS, the likelihood function is given by

$$p(\mathbf{y}_{t-L+1:t}|\mathbf{x}_{t-L+1:t}^i) \propto \prod_{j=t-L+1}^{t} e^{\left[-0.5\beta^2(\mathbf{y}_j-\widehat{\mathbf{y}}_j^i)^T\mathbf{R}^{-1}(\mathbf{y}_j-\widehat{\mathbf{y}}_j^i)\right]} \tag{4.20}$$

Here L is the length of the assimilation window, $\mathbf{R}$ is the covariance matrix of observations, and β is a tuning factor to avoid particle degeneracy [Dong et al., 2016b]. In the APBS, β for each assimilation window is determined by maximizing the reliability of model states (0 for zero reliability and 1 for perfect reliability). The probability metric of reliability is estimated using the Quantile - Quantile (Q-Q) plot, which indicates whether the estimated uncertainty is appropriate.

In the daytime window (09:00-16:00 LT), a maximum number of eight GOES LST observations are available. At the end of the daytime window (16:00 LT), the assimilation is performed for each model grid cell separately, if at least half of the observations (i.e., four observations) are available for that grid cell. GOES LST observations are related to modeled T_s and T_c following Kustas et al. [1996]

$$\text{LST} = \left[f_c T_c^4 + \left(1 - f_c\right) T_s^4\right]^{1/4} \tag{4.21}$$

The GOES LST observation error is assumed to be 3 K [Lu et al., 2016]. In the APBS, β is varied from 0.05 to 1 with an increment of 0.05, and the β value that yields the largest reliability is selected. After assimilation, particles of modeled T_s and T_c as well as parameters are updated, and fluxes are estimated as the weighted sum of all particle estimates.

Table 4.2: Perturbations used for forcing data.

Forcing	Perturbation	Standard Deviation
$R_s^{\downarrow}$	Gaussian, ×	×, 0.1
$R_l^{\downarrow}$	Gaussian, ×	×, 0.1
U	Gaussian, +	1 m/s
T_a	Gaussian, +	5 K
P	Lognormal, ×	×, 0.2

* '×' and '+' represent multiplicative and additive perturbations, respectively.

4.2.5. EXPERIMENT SETUP

The model is run for 120 days from DOY 155 to 274, 2015 at 30-min time step for each 0.05° grid cell using 600 particles. Off-line sensitivity analysis confirms that this number of particles is large enough to yield stable results. Grid cells with dominant land cover of water or urban area are masked out in the modeling. Since the model grids are of finer resolution than the forcing data, the forcing data are extracted from the forcing data grid cell in which the center of the model grid cell falls. The perturbations used for the forcing data are listed in Table 4.2. The perturbations are used to characterize the data uncertainties caused by the uncertainty of the forcing data as well as the heterogeneity within the forcing data grid cell. Sensitivity analysis reveals that flux estimation is robust as long as the perturbations are reasonable. The model and observation errors used are adopted from Lu et al. [2016], and prove to have limited influence on the flux estimates. The ancillary data are spatially aggregated to the modeling scale. The LAI data are also temporally interpolated to get daily LAI data.

The unknown parameters are a and b in estimating C_{HN}, and α_s and α_c in estimating reference EF. Based on the acceptable ranges of soil roughness and vegetation density, the valid ranges are determined for a (-7<a<-5) and b (0<b<1) following Abdolghafoorian et al. [2017]. The initial range of (1,10) is used for α_s and α_c based on Dirmeyer et al. [2000]. This range allows sufficient EF dynamics based on soil moisture condition. Sensitivity analysis demonstrated that the model would generate reliable results as long as the parameters were generated within physically reasonable ranges.

The main input data are solar radiation ($R_s^{\downarrow}$ and $R_l^{\downarrow}$) and meteorological data (P, T_a, U and P_a). At the start of the experiment, parameters are uniformly sampled within the given ranges, and the energy balance is constructed at each time step for soil and canopy separately. To calculate net radiation, soil albedo (alb_s) is calculated from surface soil moisture based on Idso et al. [1975], and canopy albedo (alb_c) is based on the values given in Houldcroft et al. [2009] and assumed constant.

During daytime, H is calculated using propagated T_s and T_c, and LE is calculated using H and estimated EF. G is derived as the residual of the energy balance equation and is used to propagate T_s of the next time step. From 16:00 to 09:00 the next day, G is assumed a random fraction of R_{ns} as EF is no longer conservative, and T_s is propagated. T_c is then assumed equal to T_s.

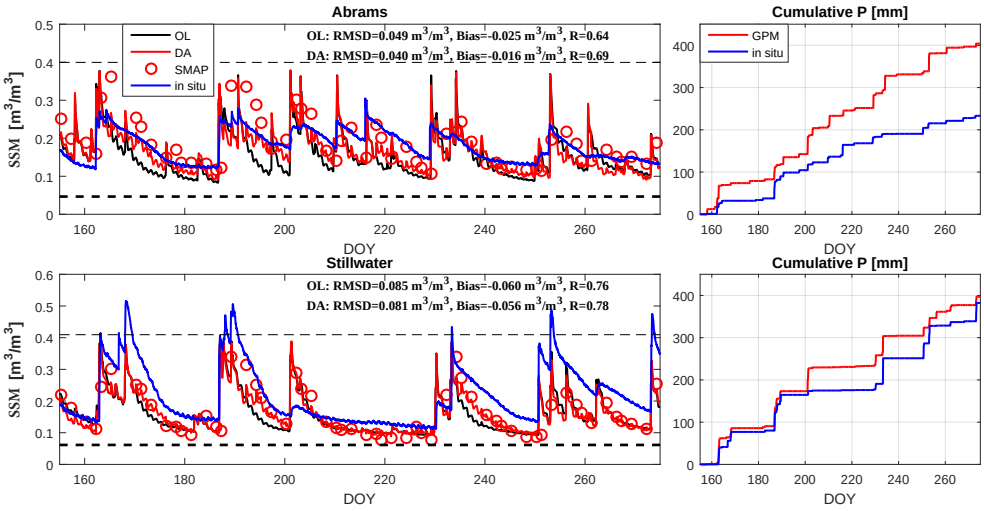

Figure 4.3: Surface soil moisture (0-5 cm, hereafter SSM) assessment against in situ measurements. The thick and thin dashed lines represent residual and saturated soil moisture used in the modeling, respectively.

4.3. RESULTS AND DISCUSSION

4.3.1. SOIL MOISTURE AND LST ESTIMATION

Modeled SSM after assimilation (hereafter DA) and from OL is assessed against in situ measurements in Abrams and Stillwater. It should be noted that the modeled results are at 0.05° resolution, while in situ data are point measurements. The same is true for flux data, therefore the term 'assessment' is used instead of 'validation'. The implicit assumption is that the point measurements are representative of the model grid cell condition, which may be influenced by surface heterogeneity. The assessment results are shown in Figure 4.3. In general, the modeled SSM from OL and DA follows the dynamics of in situ measurements very well. This reveals the good timing of precipitation events from GPM data, which can be seen more clearly in the cumulative precipitation plots on the right. When SMAP observations are available, the SSM is updated towards SMAP observations and gets closer to in situ soil moisture, which is most evident from DOY 190-200 at both stations. This demonstrates that assimilating SMAP soil moisture data improves SSM estimates, despite the coarse resolution.

The improvement is also reflected in the statistical metrics, especially in Abrams. In Abrams, the RMSD decreases from 0.049 m^3/m^3 for OL to 0.040 m^3/m^3 for DA, and the estimation bias decreases from -0.025 m^3/m^3 for OL to -0.016 m^3/m^3 for DA. The R also increases from 0.64 for OL to 0.69 for DA. The improvement is mostly due to a better characterization of the dry-down events after assimilating SMAP soil moisture data. The estimation is less accurate in Stillwater, reflected by larger RMSD and bias. Only small improvement can be seen from the RMSD (0.085 to 0.081 m^3/m^3), bias (-0.060 to -0.056 m^3/m^3) and R (0.76 to 0.78) metrics after assimilation. This is caused by the erroneous soil hydraulic properties and disagreement in precipitation magnitude between GPM and in situ precipitation measurements. For example, the saturated soil moisture (thin

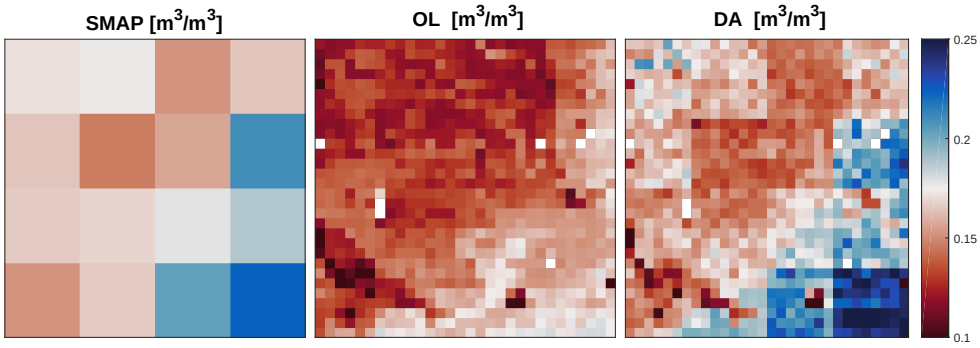

Figure 4.4: SSM from SMAP, OL and DA at 06:00 LT, DOY 173.

dashed line) estimated using ROSETTA is about 0.4 m^3/m^3, but the maximum in situ soil moisture measurement exceeds 0.5 m^3/m^3 during many rain events. This would lead to a general underestimation of soil moisture, which is reflected in the large negative bias in both OL and DA results. On DOY 201, a precipitation event is detected in both GPM and in situ data, but the magnitudes differ significantly (>50 mm from GPM and <10 mm from in situ data). As a result, modeled soil moisture increases sharply to near saturation, while only a small increase is seen from in situ soil moisture measurements. A large increase in soil moisture is also seen in SMAP observations between DOY 200 and 202, which is in line with GPM measurements. This may be caused by the spatial heterogeneity of precipitation, which appears to be lighter at the station location than in the surrounding areas.

Figure 4.4 shows that after assimilation, the magnitude of SSM agrees better with SMAP observations, and the spatial patterns are preserved at 0.05°. A dry-wet gradient from the northwest to the southeast is revealed by SMAP observations. The pattern is also seen in OL estimates but less clearly, and large gap in the magnitude exists between SMAP observations and OL estimates. After assimilation, the gradient is much clearer, and the spatial heterogeneity of soil moisture within each SMAP grid cell is preserved in the DA results.

30-min LST estimates from OL and DA within the daytime window are compared to GOES LST observations for each model grid cell in Figure 4.5. To perform the assessment, all GOES LST observations available within the daytime window each day are found. The corresponding modeled LST from OL and DA are extracted to calculate statistical metrics for each model grid cell separately. After assimilation, 30-min LST estimates improve significantly based on all the metrics. The range of R^2 improves from 0.6-0.7 for OL to 0.8-0.9 for DA, and the RMSD improves from > 5 K for OL to < 4 K for DA. The estimation bias for OL is generally between 2-8 K, and is reduced to almost zero after assimilation.

4.3.2. FLUX ESTIMATION

The 30-min H estimates are compared to in situ observations at the four flux stations on days when assimilation is performed, as shown in Figure 4.6. Generally, the improve-

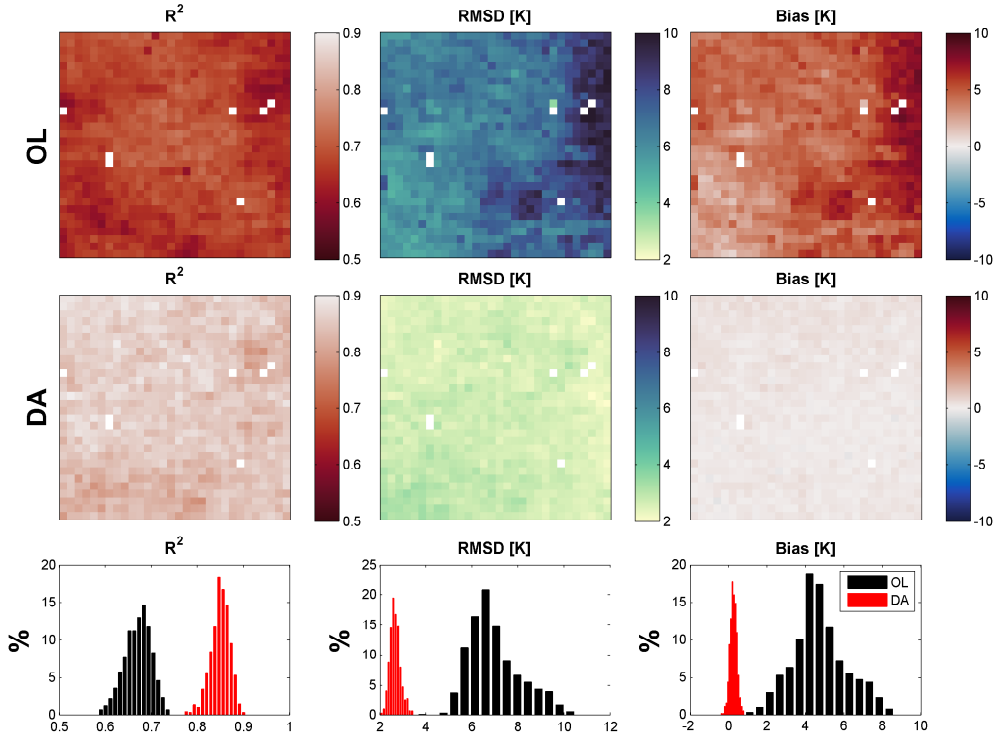

Figure 4.5: 30-min LST assessment against GOES observations. The histograms of the metrics are plotted in the third row.

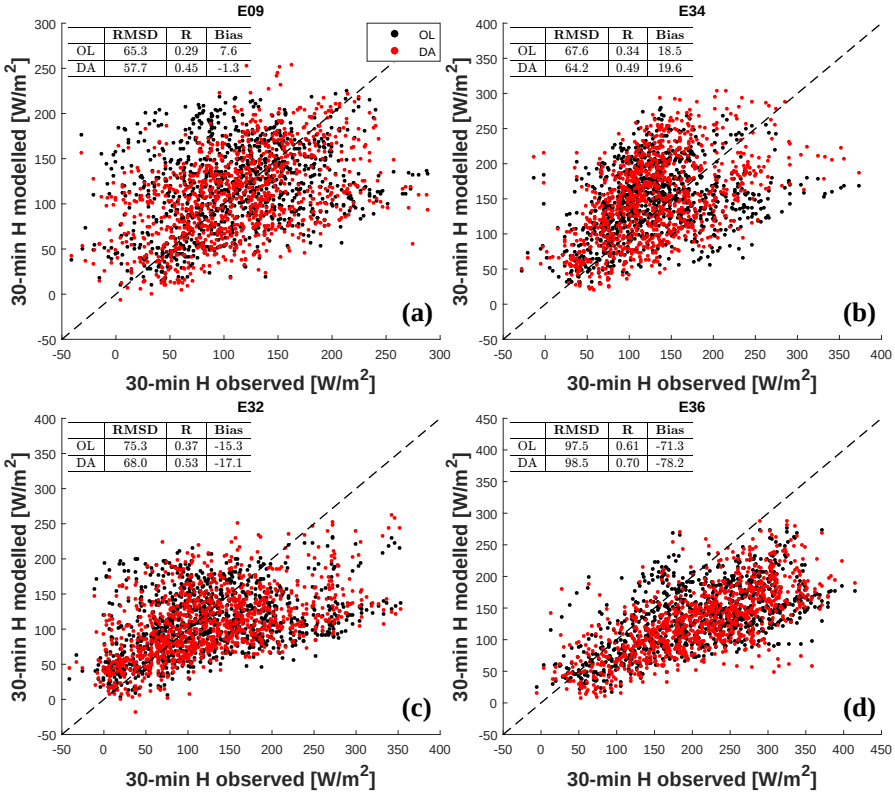

Figure 4.6: 30-min H assessment against in situ observations. The units of RMSD and Bias are W/m^2.

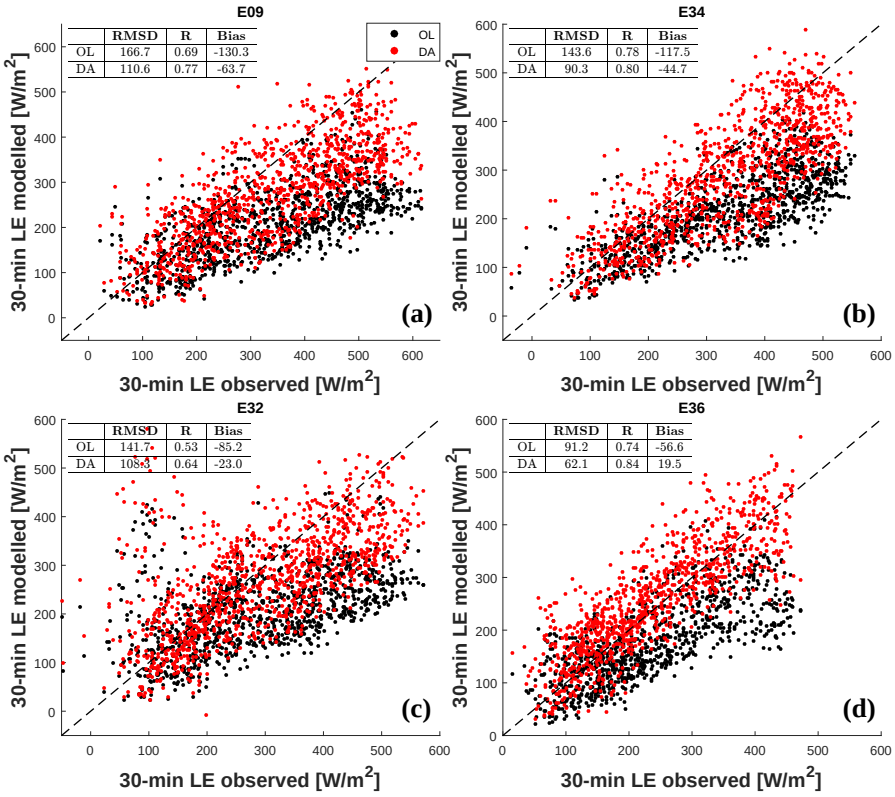

Figure 4.7: As in Figure 4.6 but for 30-min *LE* estimates.

ment in H is moderate, with the largest improvement in R. On average, R is increased by 0.14 and the RMSD is decreased by 6.3%. This is caused by the compensation effect between C_{HN} magnitude and LST dynamics on H estimates. For example, if C_{HN} is very large for a particle, G will be small based on the energy balance, which will lead to a small LST at the next time step. As C_{HN} and LST compensate each other on the influence on H, the variation of H with C_{HN} will be small, and vice versa for small C_{HN} values.

Figure 4.7 shows the skill of 30-min *LE* estimates. In contrast to the H estimates, the improvement after assimilation is more evident in all the stations. Since *LE* is determined by H and EF calculated from soil moisture, high R values are achieved in both OL and DA results, which proves the validity of the EF~ SWI relationship. The assimilation improves *LE* estimates in two ways: (1) smaller and more reasonable ranges of α_s and α_c through data assimilation to characterize EF dynamics, and (2) better daytime LST evolution to get more accurate R_n estimates. As shown in Figure 4.7, RMSD and bias decrease dramatically after assimilation. Averaged among the four stations, RMSD decreases from 135.8 W/m^2 to 92.8 W/m^2, and bias decreases from -97.4 W/m^2 to -28.0 W/m^2.

Time series of daytime H and *LE* estimates are plotted in Figure 4.8. modeled SSM

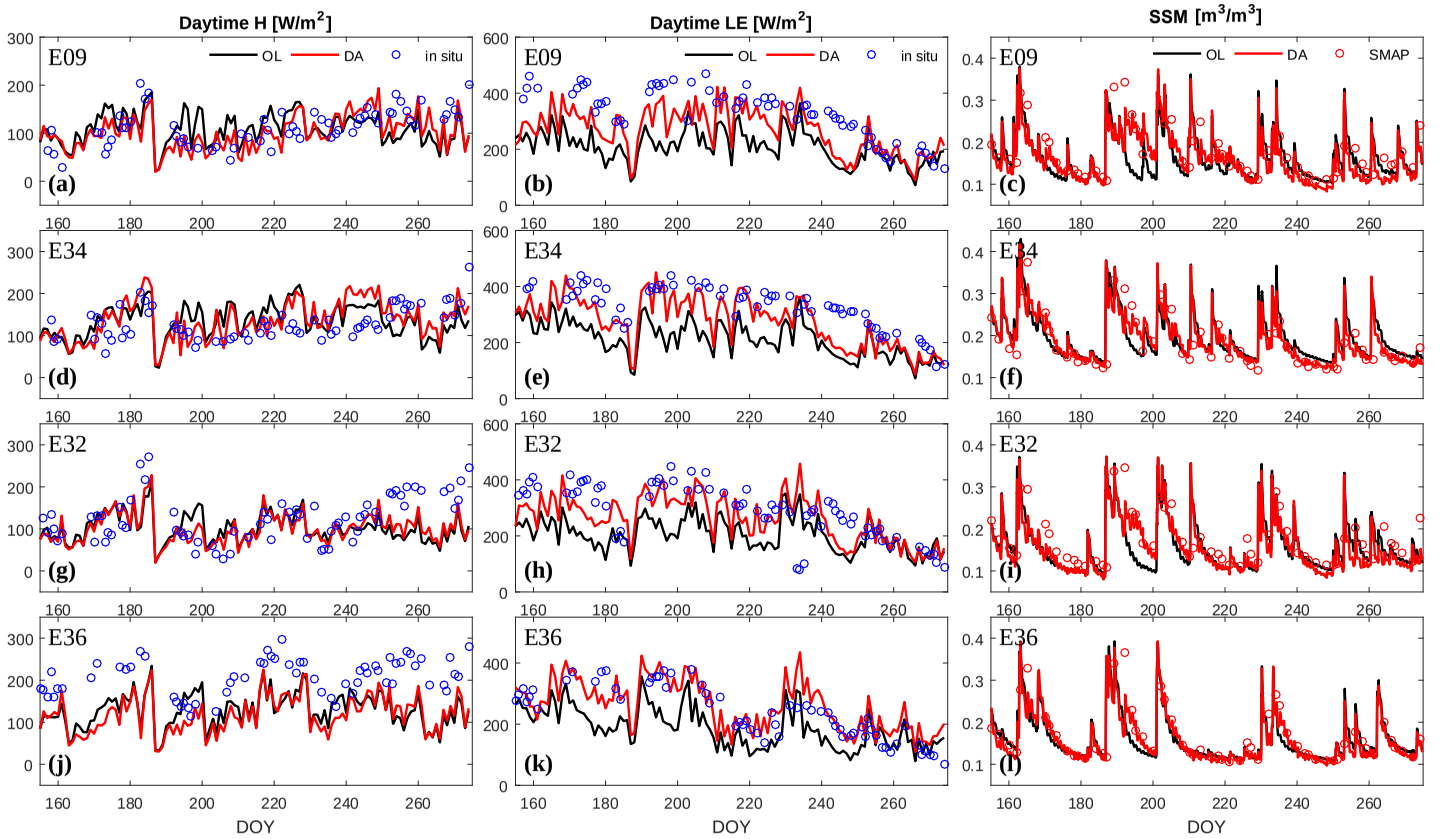

Figure 4.8: Time series of daytime flux estimates from OL, DA plotted against in situ measurements on days with assimilation at the 4 stations. The 5 cm soil moisture data from OL, DA and the corresponding SMAP grid cells are also plotted in the column on the right.

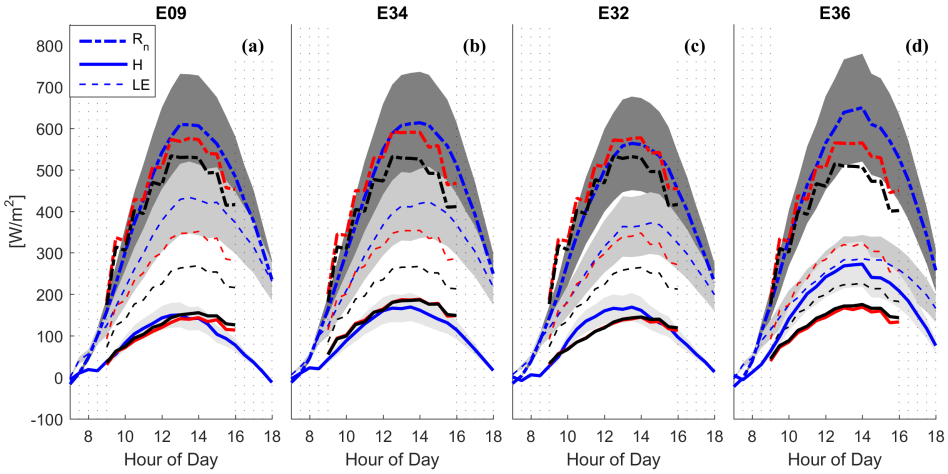

Figure 4.9: modeled and measured average daytime cycles of R_n (dash-dot line), H (solid line) and LE (dashed line). The colors indicate results from DA (red), OL (black) and in situ observations (blue). The gray bands represent observed fluxes ± 20% uncertainties.

and the corresponding SMAP observations are also plotted as a reference for soil wetness condition. The dynamics of observed H and LE agree very well with soil moisture evolution, which is consistent with the soil wetness control on surface energy partitioning. When data assimilation is performed, the magnitude of soil moisture is updated towards SMAP observations, which improves the characterization of EF dynamics. For example, during DOY 192 and 197 the OL soil moisture deviates significantly from SMAP observations at station E09 (Figure 4.8c), leading to substantial underestimation of LE. This may be caused by the failure in the forcing data to record some precipitation events. After assimilation, soil moisture gets much higher, and the high LE values are better modeled. The improvement from assimilation is also revealed in the better estimates of parameters. For example, from DOY 200 to 230, the modeled soil moisture at station E34 (Figure 4.8f) from OL and DA are almost the same, but the LE estimates from DA are in much better agreement with in situ observations. Since parameters are also updated during assimilation, more reasonable ranges are obtained for the parameters, thus EF values are estimated more accurately.

Figure 4.9 shows the comparison between average modeled fluxes (R_n, H and LE) and average in situ observations during daytime. The R_n estimates from OL are generally much lower than in situ observations. This is caused by the dry bias in soil moisture estimates (Figure 4.3) and warm bias in LST estimates (Figure 4.5) from OL. As a result, the outgoing shortwave and longwave radiation are higher, and the R_n estimates become lower, which explains the large negative bias in LE estimates from OL in Figure 4.7. The R_n estimates from DA are in better agreement with in situ observations, which further proves the validity of the R_n estimation approach. H and LE estimates from OL hardly fall in the gray bands, which indicate 20% uncertainties around in situ observations caused by measurement uncertainty and surface heterogeneity. After assimilation,

the daytime flux evolution is largely improved, especially for *LE* estimates.

4.3.3. PARAMETER ESTIMATION

Figure 4.10 shows the C_{HN} and EF estimates and the corresponding LAI and modeled SSM on 3 days with different wetness conditions. A positive gradient of LAI from the northwest to the southeast is clearly seen in Figure 4.10d-4.10f, which influences the spatial pattern of C_{HN}. During the modeling period, the area average LAI value increases from about 1.22 on DOY 155 to about 1.35 on DOY 170, and decreases to about 1.28 on DOY 185, and then increases quickly to about 1.48 on DOY 201, followed by a sharp decrease to about 0.8 on DOY 274. During DOY 176 and 193, C_{HN} increases dramatically, particularly in the western part of the area, which is largely caused by the increase in LAI. From DOY 193 to 220, LAI decreases greatly, especially in the eastern part. As a result, a decrease is observed in C_{HN} estimates. The magnitude of estimated C_{HN} is comparable to the reported values in literature [Caparrini et al., 2004b; Bateni et al., 2014; Xu et al., 2014].

The estimated EF distribution is shown in Figure 4.10g-4.10i. On DOY 176, the area is in the process of a long dry-down event from DOY 170 to 187, and the eastern part is much wetter than the western part. As a result, the EF estimates demonstrate an increasing trend eastward. Several precipitation events occurred shortly before DOY 193, therefore the area is very wet, and EF values are generally very high. From DOY 200 until DOY 225, the precipitation pattern is very different in the north and south. As is demonstrated in Figure 4.3 and Figure 4.8, precipitation in the north features several large precipitation events, while the south experiences a long dry-down. On DOY 220, the soil moisture in the north is much higher than that in the south, and the same pattern is seen in the EF map. Some grid cells with EF values greater than 0.5 exist in the south, which is caused by the heterogeneity in the soil properties.

4.3.4. ADDED VALUE OF SMAP SOIL MOISTURE DATA

To evaluate the added value of assimilating the coarse SMAP soil moisture data in flux estimation, the model is also run with only GOES LST data assimilated (hereafter DA_T) and with only SMAP soil moisture data assimilated (hereafter DA_θ)). The comparison of 30-min flux estimates from DA, DA_T and DA_θ is shown in Figure 4.11.

When only SMAP soil moisture data are assimilated, the soil moisture estimates from DA_θ will be similar to those from DA. As a result, DA_θ is able to yield comparable R values in both *H* and *LE* estimates with DA, which again proves the tight coupling between soil moisture and heat flux partitioning. However, since the parameters and LST states cannot be updated through soil moisture assimilation, the LST evolution from DA_θ is similar with LST from OL. As a result, large RMSD and bias exist in the *LE* estimates as is in OL estimates.

When only GOES LST data are assimilated, DA_T performs worse than DA in flux estimates at station E09, E34 and E32 based on all the metrics. At station E36, DA_T produces smaller RMSD and bias in *H* estimates. This is caused by the large underestimation of R_n at this station (Figure 4.9). As a result, the RMSD and bias in *LE* estimates become larger in DA_T. In general, assimilating SMAP soil moisture data leads to significant improvement in flux estimates, despite the coarse resolution.

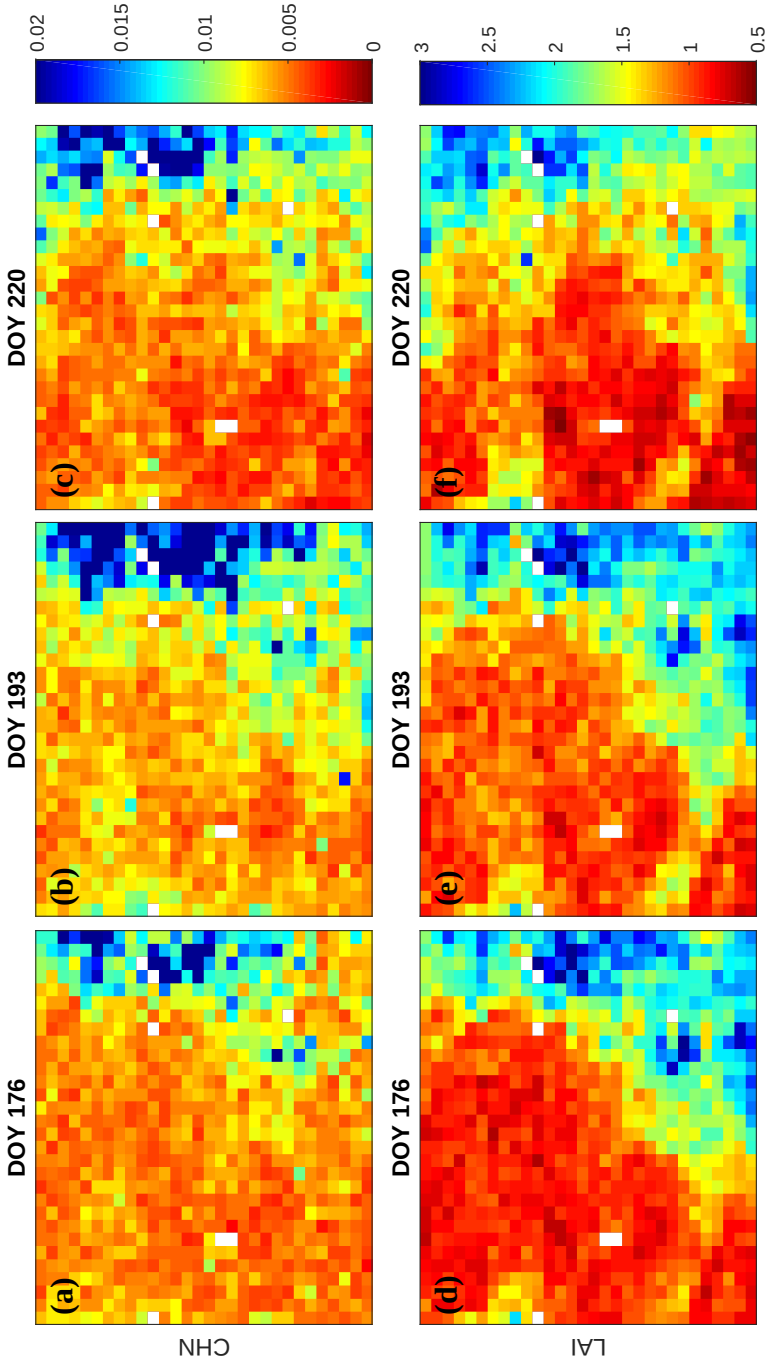

(a)

Figure 4.10: Spatial distribution of C_{HN}, LAI, EF and 5-cm modeled soil moisture on 3 days (DOY 176, 193, 220).

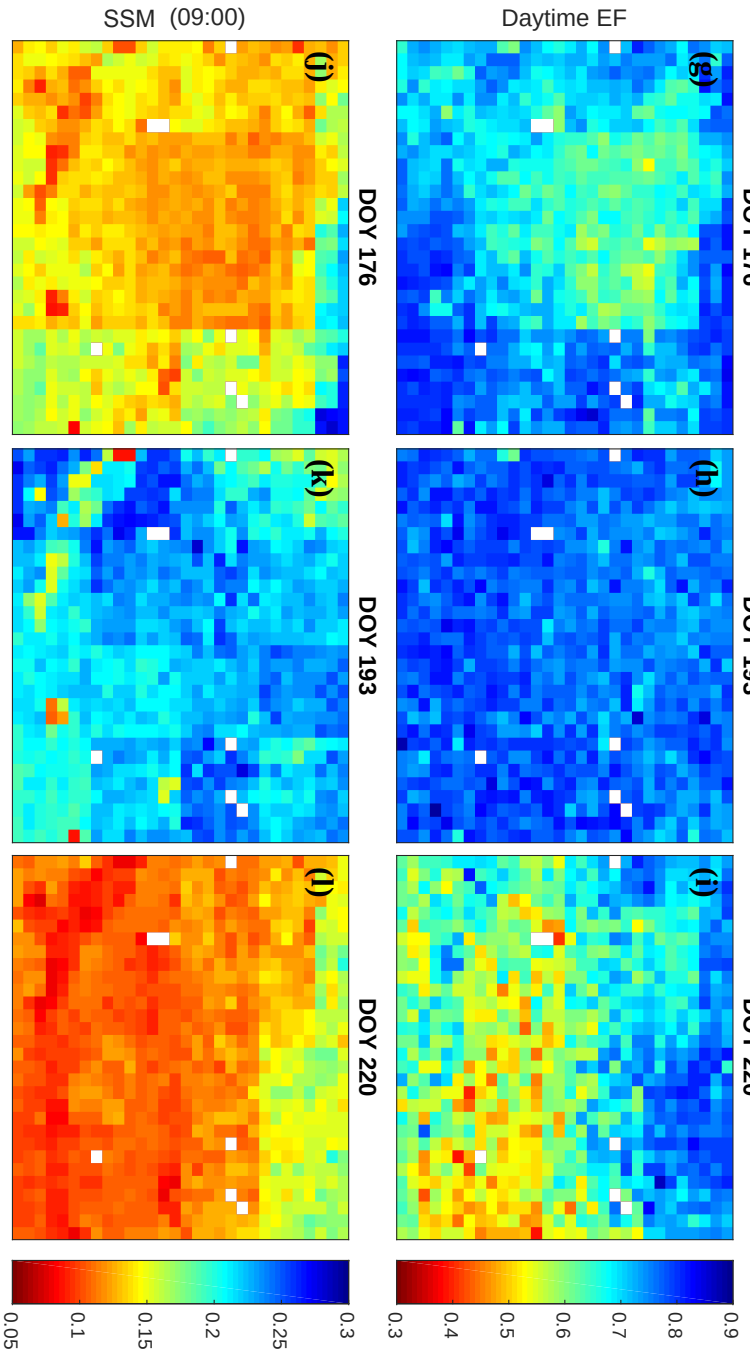

Figure 4.10: Continued.

(b)

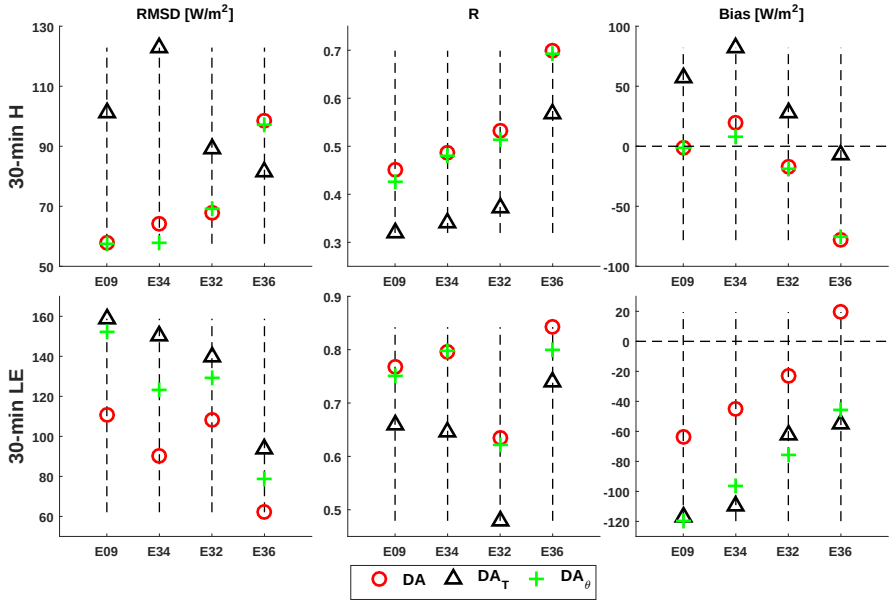

Figure 4.11: Comparison of 30-min H and LE estimates from DA, DA_T (only GOES LST assimilated) and DA_θ (only SMAP soil moisture assimilated).

It should be noted that at station E09 and E34, the flux estimates from DA_T can be even worse than OL results, featured by a significant overestimation of H and underestimation of LE. This is caused by the poor characterization of soil moisture evolution. As soil moisture data are not assimilated, the soil moisture estimates from DA_T are similar to those from OL. As is discussed in Section 4.3.2, when some precipitation events are not recorded in the forcing data, soil moisture estimates from DA_T will exhibit a dry bias, and EF will be very low accordingly. Since the model is still constrained by GOES LST data in DA_T, the particles with very large C_{HN} values will get larger weights to fit the LST observations. Consequently, the H estimates from DA_T will be much higher and the LE estimates much lower compared to OL results, leading to worse flux estimates. This demonstrates that despite the very coarse resolution, assimilating SMAP soil moisture data is not only beneficial but also crucial for successful and robust flux estimation, particularly when the uncertainties in the forcing data, model structure or parameters are large.

4.4. CONCLUSIONS

This chapter proposes a methodology to estimate surface heat fluxes by assimilating SMAP soil moisture data and GOES land surface temperature (LST) data using a hybrid particle assimilation strategy. The methodology is based on a dual-source (DS) surface energy balance model, in which the contributions from soil and canopy are calculated separately. Fluxes are derived by estimating four parameters which are used to calculate a neutral bulk heat transfer coefficient (C_{HN}) and an evaporative fraction (EF). In

the hybrid particle assimilation strategy, SMAP soil moisture data are assimilated using the particle filter (PF), and GOES LST data are assimilated within the daytime window (09:00-16:00 LT) using an adaptive particle batch smoother (APBS). In this way, the resolution gap between SMAP and GOES data is bridged, and the flux estimation becomes independent of in situ flux observations. The methodology is applied over an area in the US Southern Great Plains, and the results are compared with in situ observations.

In general, the modeled soil moisture from OL and DA follows the dynamics of in situ observations very well. After assimilation, modeled surface soil moisture is updated towards the in situ observations, which is most evident in dry-down events. In addition, the spatial heterogeneity of soil moisture within a SMAP grid cell is preserved, since the model grids are of finer resolution than SMAP grids. The improvement in LST estimates is also significant after assimilation.

H and *LE* estimates are improved after assimilation at both daytime and 30-min scales. The improvement is more evident in *LE* estimates. The time series of daytime *H* and *LE* as well as their mean daytime cycles are also better characterized after assimilation.

Despite the coarse resolution, assimilating SMAP soil moisture data leads to large improvement in flux estimates. As the estimation is influenced by the uncertainties in the forcing data, model structure and parameters, modeled soil moisture may be biased. By assimilating SMAP soil moisture data, the bias is reduced, which facilitates the estimation of EF. Therefore, assimilating SMAP soil moisture data is not only beneficial but also crucial for successful and robust flux estimation, particularly when the uncertainties are large. Here the 36-km SMAP soil moisture data are used, so the methodology should also be applicable for other soil moisture products with coarse resolution (e.g., SMOS, AMSR-E, AMSR2, ASCAT).

The forcing data used in this chapter are from remote sensing and reanalysis products, and in situ flux observations are not required to calibrate the model. As the dependence on in situ data is minimized, the methodology can be easily applied to other areas.

5

IMPROVING SURFACE HEAT FLUX ESTIMATES BY ASSIMILATION OF SMAP BRIGHTNESS TEMPERATURE AND GOES LAND SURFACE TEMPERATURE DATA

This chapter is based on:

Lu, Y., S. C. Steele-Dunne, G. De Lannoy, Improving Surface Heat Flux Estimates by Assimilation of SMAP Brightness Temperature and GOES Land Surface Temperature Data. (*in revision*)

5.1. INTRODUCTION

IN the previous chapter, it has been demonstrated that surface heat flux estimates can be improved by assimilating GOES LST data together with SMAP soil moisture retrievals. A potential risk of assimilating remote sensing soil moisture retrievals lies in the retrieval algorithm, which utilizes land surface parameters and background information including, for example, LST data. These data are often outputs of other models, which may be inconsistent with, or even contradictory to the model simulations in the assimilation system. Furthermore, the retrieval errors will be correlated to ancillary data, which in turn may be correlated to the background information used in data assimilation [De Lannoy and Reichle, 2016b]. Therefore, it is natural to consider assimilation of brightness temperature (TB), which is the direct measurement of satellite microwave radiometer.

It is more difficult to assimilate TB observations than soil moisture retrievals since the TB is indirectly related to land surface variables. A radiative transfer model (RTM) needs to be adopted as the observation operator to translate modeled land surface variables into TB simulations. Several TB assimilation studies have been conducted, which have used TB observations from Advanced Microwave Scanning Radiometer for Earth observation science (AMSR-E) [Tian et al., 2009; Zhao et al., 2016; Yang et al., 2016] and Soil Moisture Ocean Salinity (SMOS) [De Lannoy and Reichle, 2016a,b; Lievens et al., 2016, 2017a], and mainly focused on improving soil moisture estimates. However, SMAP TB assimilation studies are limited to the operational SMAP Level-4 data products [Reichle et al., 2017a,b] and research studies such as Lievens et al. [2017b], and no studies have focused on surface heat flux estimation or compared the differences between assimilating TB observations or soil moisture retrievals.

The goal of this study is to determine if the assimilation of physically consistent TB and LST data could yield improved surface heat flux estimates. Here SMAP TB observations at either horizontal or vertical polarization are assimilated together with GOES LST data, and the results are compared to those from Chapter 4, in which SMAP soil retrievals instead of TB data were assimilated. The objective is to investigate the information contained in SMAP TB observations for surface heat flux estimation in comparison with that from SMAP soil moisture retrievals, through assimilation with GOES LST data, and to provide insight into the differences in using horizontally or vertically polarized TB data.

5.2. MATERIALS AND METHODS

5.2.1. STUDY AREA AND DATA

The study area is the same with that used in Chapter 4. The input data are also similar to be consistent, except that the SMAP TB data are assimilated instead of SMAP soil moisture retrievals. The TB data for assimilation are the SMAP Level-1C (L1C_TB) data acquired by the L-band radiometer at 2-3 days interval [Entekhabi et al., 2014]. The TB observations are the arithmetic average of the fore- and aft-looking TB data obtained from https://reverb.echo.nasa.gov/ and are only assimilated at 06:00 LT (descending node). TB data are processed and mapped to geographic coordinates.

5.2.2. RADIATIVE TRANSFER MODEL (RTM)

To assimilate SMAP TB observations, the state propagation model for water and heat transfer is coupled to a RTM to generate TB simulations. The RTM used in this chapter mimics the RTM used in the SMAP Level-2 retrieval algorithm [O'Neill et al., 2015]. This model is developed by Jackson [1993] based on the $\tau-\omega$ model. This model applies to TB in both horizontal (TB_H) and vertical (TB_V) polarization. The real part of soil dielectric constant (ε_r) is first calculated from soil moisture using a dielectric model. Here the model proposed by Mironov et al. [2009] is used for its simplicity over other models [Wang and Schmugge, 1980; Dobson et al., 1985]. The smooth surface soil emissivity (e_{soil_s}) is calculated from the dielectric constant using the Fresnel equation.

For horizontal polarization, e_{soil_s} is calculated by

$$e_{soil\_s} = 1 - \left| \frac{\cos\eta - \sqrt{\varepsilon_r - \sin^2\eta}}{\cos\eta + \sqrt{\varepsilon_r - \sin^2\eta}} \right|^2 \tag{5.1}$$

where η is the incidence angle, which is 40° for the SMAP radiometer.

For vertical polarization, e_{soil_s} is calculated by

$$e_{soil\_s} = 1 - \left| \frac{\varepsilon_r\cos\eta - \sqrt{\varepsilon_r - \sin^2\eta}}{\varepsilon_r\cos\eta + \sqrt{\varepsilon_r - \sin^2\eta}} \right|^2 \tag{5.2}$$

The influence of surface roughness [Choudhury et al., 1979] is then included to derive the rough surface soil emissivity (e_{soil_r}) by

$$e_{soil\_r} = 1 - \frac{1 - e_{soil\_s}}{\exp(h_r\cos^2\eta)} \tag{5.3}$$

where h_r is a parameter dependent on the polarization, frequency and surface geometric properties [Entekhabi et al., 2014].

Further, vegetation influence is included to derive the land surface emissivity (e_{surf}):

$$e_{surf} = [1-\omega_s]\left[1-\gamma\right]\left[1+\left(1-e_{soil\_r}\right)\gamma\right] + e_{soil\_r}\gamma \tag{5.4}$$

Here ω_s [-] is the scattering albedo, and γ [-] is the one-way transmissivity of the canopy, which is estimated from the vegetation water content (VWC) based optical depth (τ):

$$\gamma = \exp(-\tau\sec\eta) = \exp(-b_v\cdot \mathrm{VWC}\cdot\sec\eta) \tag{5.5}$$

The values for h_r, ω_s and b_v are taken from a look-up table provided in O'Neill et al. [2015], and VWC is calculated from the actual NDVI data [O'Neill et al., 2015]. This is different from SMAP soil moisture retrieval algorithm, which uses NDVI climatology derived from multi-year data.

TB of the land surface (TB_{land}) is given by

$$TB_{land} = e_{surf}\cdot T_{eff} \tag{5.6}$$

where T_{eff} [K] is the effective temperature of the land surface, which is a measure of the contribution of the whole soil column to microwave emission. In many studies, T_{eff} is estimated as a weighted average of the surface and deeper ground temperature [Choudhury et al., 1982; Wigneron et al., 2001, 2008; Holmes et al., 2006]. Here the method proposed by Wigneron et al. [2008] is adopted, which considers the influence of soil moisture on the weights. TB simulations are performed at the model resolution of 0.05° and then aggregated to the SMAP TB grid scale (36-km) using a simple arithmetic averaging.

Water bodies within a SMAP cell dramatically lower the TB observations, and need to be accounted for in the forward modeling. At SMAP descending overpass (06:00 LT), the temperature within one model grid cell is very homogeneous, hence the water temperature is assumed the same as soil temperature, and $\mathrm{TB}_{\mathrm{water}}$ is derived using a theoretical model proposed by Klein and Swift [1977]. The simulated TB observations ($\mathrm{TB}_{\mathrm{sim}}$) is then calculated as a weighted average of $\mathrm{TB}_{\mathrm{land}}$ and $\mathrm{TB}_{\mathrm{water}}$:

$$\mathrm{TB}_{\mathrm{sim}} = f_{water}\mathrm{TB}_{\mathrm{water}} + (1 - f_{water})\mathrm{TB}_{\mathrm{land}} \tag{5.7}$$

where f_{water} is the water fraction in the model cell.

Since the TB of man-made, impervious and urban areas cannot be modeled theoretically [O'Neill et al., 2015], the urban fraction within model grid cells is treated in the following way: (1) If urban area is not the dominant land cover type of the cell, the cell is considered 'effective' and the influence from urban area is assumed marginal and ignored. (2) Otherwise, the cell is considered 'ineffective' and $\mathrm{TB}_{\mathrm{sim}}$ is not calculated for that grid cell. The 'ineffective' grid cells are not included in the spatial aggregation to the 36-km SMAP TB simulations.

5.2.3. BIAS CORRECTION AND OBSERVATION ERROR FOR SMAP TB

A seasonal correction approach is used here to correct for the bias in TB observations. In Chapter 4 CDF matching was used to correct for the bias in SMAP soil moisture since the bias in soil moisture is very stationary and less season dependent. In contrast, despite the dependence on soil moisture, the magnitude of TB is also strongly influenced by T_{eff} and vegetation patterns. The bias in TB hence varies with season, since both T_{eff} and vegetation have a strong season cycle. Therefore only the seasonally varying difference between SMAP TB observations and ensemble mean TB simulations is corrected.

The bias correction steps are conducted for TB_{H} and TB_{V} separately using data from 2015. Since SMAP TB observations are coarser than model simulations, the simulated TB is derived by averaging all 'effective' modeled TB from model grid cells that fall into each SMAP cell. To this end, we first calculate the ensemble mean of modeled TB for each 'effective' model grid cell at each SMAP descending overpass time. Then a 30-day moving window is used, which averages the time series of SMAP TB observations as well as simulated TB forecasts for each SMAP grid cell separately. Finally, the differences between window-mean SMAP TB observations and model simulations are removed from SMAP minus simulated TB innovations.

TB observation error consists of instrument error and representativeness error. The instrument error for SMAP radiometer is anticipated to be around 1.3 K at 36-km scale [Reichle et al., 2012; Das et al., 2016]. The representativeness error is composed of RTM

errors resulted from imperfect model structure, sub-optimal parameters or ancillary data (e.g., vegetation, soil), and the spatial and temporal mismatch error between TB observations and model simulations. The representativeness error for SMAP TB data is assumed similar to that of SMOS TB data, since both missions operate in L-band and provide TB observations at similar spatial scales. The representativeness error depends on soil moisture and LST and should ideally be modeled online in the assimilation system. Here a constant representativeness error of 4.5 K is adopted following De Lannoy and Reichle [2016a] for simplicity. The observation error is then assumed to be 5 K ($5 \approx \sqrt{1.3^2 + 4.5^2}$) for both horizontal and vertical polarizations.

5.2.4. SMAP TB ASSIMILATION

Similar to the case in Chapter 4, a hybrid particle assimilation strategy is used to assimilation SMAP TB and GOES LST data. At SMAP descending overpass time (06:00 LT), SMAP TB observations are assimilated using the PF if available. Since the model grid cells have a finer resolution, an averaging operator is adopted to convert the RTM derived TB at 0.05° model grid cell to the simulated TB at 36-km scale. For that purpose, first all 'effective' model grid cells in one SMAP TB grid cell are identified. Second, for each 'effective' model grid cell the particles are sorted by their simulated TB, which serves as the basis for updating particles in the assimilation procedure. This is to ensure that spatial patterns simulated by the model are retained in the updated states. Here it is assumed that the first particle yields the highest TB, while the last particle has the lowest TB. Finally, for all 'effective' model grid cells the particles are grouped by their respective ranking (i.e., the first group contains all the first ranked particles from each of the model grid cells). The simulated TB observation for each group is then estimated as the algebraic average of all members

$$\widehat{\mathbf{y}}_t^i = \frac{\sum_{j=1}^{M} \mathrm{TB}_{j,t}^i}{M} \tag{5.8}$$

Here M stands for the total number of 'effective' model grid cells within one SMAP grid cell, $\mathrm{TB}_{j,t}^i$ is the TB simulation of the ith particle in jth model grid cell at time step t. Here $\widehat{\mathbf{y}}_t^i$ is derived at the 36-km SMAP TB scale. During assimilation, the likelihood of each particle group is calculated using Equation 2.19. Soil moisture of the entire soil column is then updated based on the likelihood.

5.2.5. EXPERIMENT SETUP

The setup of the experiment is the same with that in Chapter 4. To evaluate the similarities between different assimilation strategy over the study area, the Kling-Gupta efficiency (KGE, [Gupta et al., 2009]) is used.

The KGE is expressed as

$$KGE = 1 - \sqrt{(r-1)^2 + \left(\frac{\sigma_{ts1}}{\sigma_{ts2}} - 1\right)^2 + \left(\frac{\mu_{ts1}}{\mu_{ts2}} - 1\right)^2} \tag{5.9}$$

where r is the correlation coefficient between two surface heat flux time series, σ_{ts1} and σ_{ts2} are the standard deviation of the two time series, while μ_{ts1} and μ_{ts2} are the

corresponding mean values. KGE ranges from minus infinity (poor agreement) to unity (perfect agreement).

5.3. RESULTS AND DISCUSSION

5.3.1. OPEN-LOOP SIMULATIONS

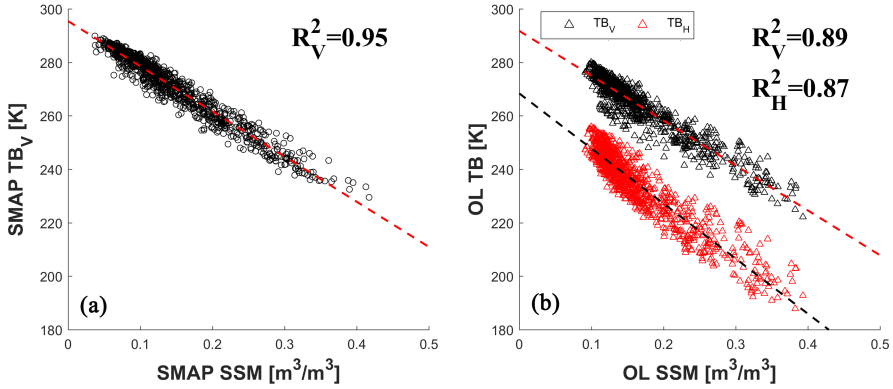

Figure 5.1: Correlations between TB and surface soil moisture (SSM) from (a) SMAP (L1C_TB and Level-3 SSM) and (b) OL simulations. The data pairs are extracted from all descending overpass time in the study period in all the 16 SMAP TB grid cells.

Figure 5.1 compares the correlations between the 36-km TB and SSM for SMAP products and OL simulations. Since the Level-3 SMAP soil moisture product is retrieved from vertically polarized TB observations using the single channel algorithm (SCA) algorithm [O'Neill et al., 2015], only TB_V is included in the SMAP analysis. The correlations between TB and SSM are generally very high, indicating a strong control on TB from the SSM condition. For vertical polarization, SMAP TB_V observations are generally higher than OL modeled TB_V and have a larger dynamic range. This may be caused by the difference between the SMAP sensing depth and model settings. Studies have shown that SMAP may measure shallower soil moisture than the nominal 5-cm depth [Shellito et al., 2016]. The simulated OL TB_V is better correlated with SSM than the TB_H simulations, which may be due to its lower sensitivity to biomass and surface roughness [Zeng et al., 2016]. The correlation between TB_V and SSM is lower for OL simulations than for SMAP data. This is mainly caused by differences in the ancillary data sets used for the operational retrieval and the forward simulation. In addition, the parameters used in RTM modeling at 0.05° are different from those used in SMAP SSM retrieval at 36-km scale.

The statistical metrics measuring the agreement between SMAP observations and OL simulations are provided in Figure 5.2 for both TB_H and TB_V (top row). The boxplots show the distribution of the statistics calculated for the 16 SMAP grid cells. OL simulated TB_V is slightly better correlated with SMAP observations than TB_H. In terms of unbiased RMSD (ubRMSD) and the bias, TB_V significantly outperforms TB_H. 8 SMAP grid cells have ubRMSD over 15 K for TB_H, while only one cell exhibits ubRMSD over 15 K for TB_V. The bias is generally less than -10 K for TB_V, while over 12 grid cells have bias

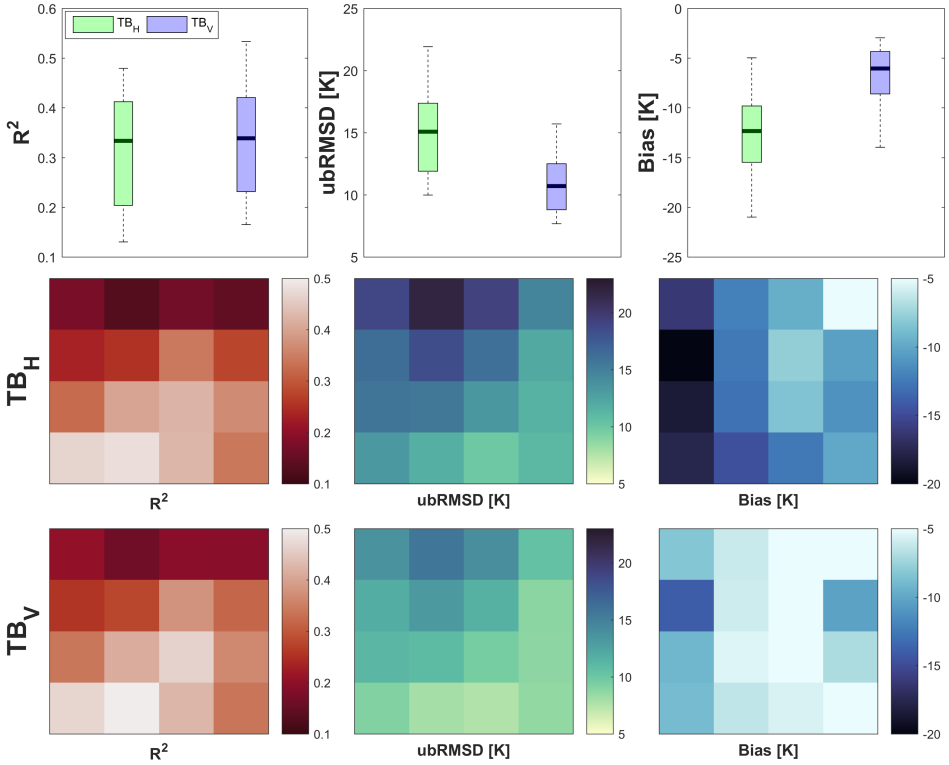

Figure 5.2: Statistical metrics between SMAP observations and OL simulations for TB_H and TB_V and their spatial patterns during the study period: (top row) boxplots for the metrics, (middle row) spatial pattern of the metrics for TB_H, (bottom row) spatial pattern of the metrics for TB_V.

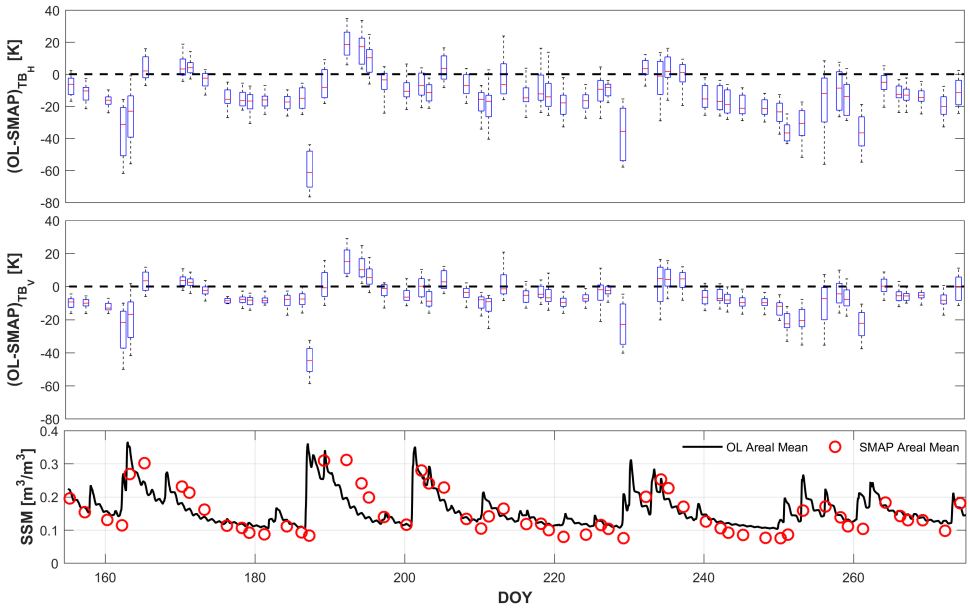

Figure 5.3: Boxplot time series of the differences between OL simulations and SMAP observations for TB_H and TB_V in the 16 SMAP grid cells. The areal mean soil moisture time series from OL simulations and SMAP is also plotted.

larger than -10 K for TB_H. Overall, the OL simulated TB is in better agreement with SMAP observations for vertical polarization than for horizontal polarization.

The spatial patterns of the statistical metrics are also shown in Figure 5.2 (middle and bottom rows). Generally, the statistical metrics show similar spatial patterns for TB_H and TB_V, where the OL simulations agree better with SMAP observations in the southeast part of the study area. The spatial patterns may be caused by the vegetation density. In the study area, a positive gradient of vegetation density is seen from the northwest to the southeast [Lu et al., 2017]. With more vegetation, the impact of soil moisture is reduced, which makes TB easier to model.

The time series of the differences between OL simulations and SMAP observations for TB_H and TB_V are plotted in Figure 5.3, and the areal mean SSM from OL simulations and SMAP Level-3 soil moisture product are also plotted for reference. The difference between OL simulated and SMAP observed TB is much smaller for TB_V than for TB_H because TB is less sensitive to soil moisture in vertical polarization than in horizontal polarization. The temporal evolution of the differences shows similar trends for both TB_H and TB_V, closely following the wet-up and dry-down events of the SSM. In general, the differences are smaller when the SSM is higher, and get larger when the soil dries down. After rainfall events, the soil moisture profile near the surface becomes very uniform, and the soil emissivity becomes less sensitive to soil moisture [Njoku and Entekhabi, 1996]. As a result, the uncertainty of TB is very small, despite the relatively shallow sensing depth for L-band radiometer for wet soil [Shellito et al., 2016]. Whereas the soil moisture profile

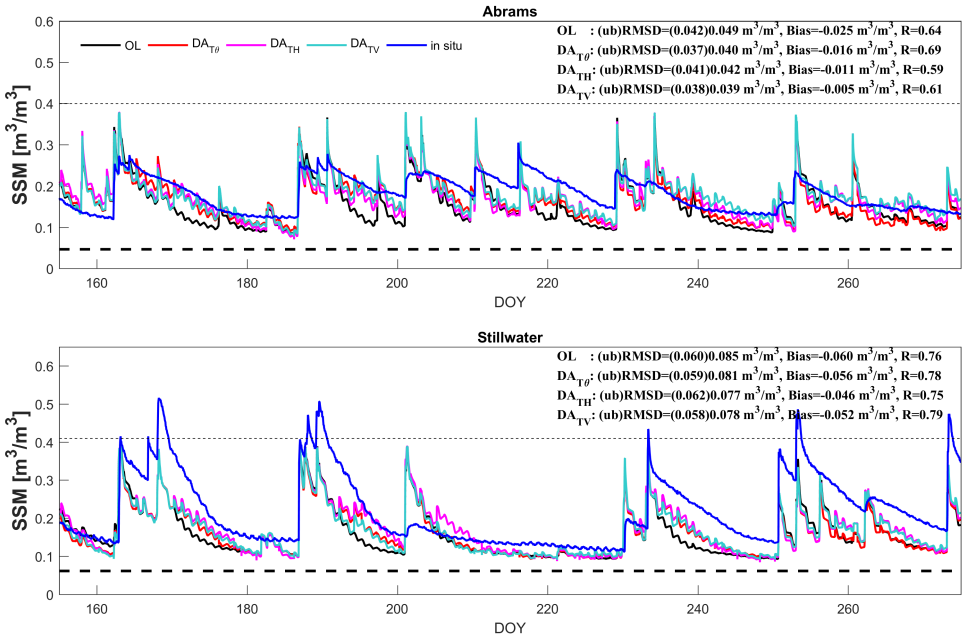

Figure 5.4: Time series of OL and assimilation results for SSM, together with in situ measurements at two stations. The ubRMSD is shown in the parentheses. The residual and saturated soil moisture used in the modeling are plotted with the thick and thin dashed lines, respectively.

gets less uniform with the soil drying down, and the deeper soil moisture influences the soil emissivity for drier soil [Njoku and Entekhabi, 1996]. Under this condition, a small difference in the sensing depth could lead to a significant difference in TB between SMAP observations and model simulations. In addition, the modeled SSM may dry down faster or slower than the true SSM, exerting different influences under wet or dry conditions. This implies that the difference between OL simulated TB and SMAP observed TB is to some extent related to the soil moisture condition or soil hydraulic properties. Correcting TB bias online as a function of soil moisture therefore could potentially improve TB assimilation schemes.

5.3.2. SOIL MOISTURE ESTIMATION

Figure 5.4 provides the comparison of SSM estimates from OL and three assimilation cases at Abrams and Stillwater. The assimilation cases include (i) assimilation of GOES LST and SMAP TB$_H$ (hereafter DA$_{TH}$), (ii) assimilation of GOES LST and SMAP TB$_V$ (hereafter DA$_{TV}$) and (iii) assimilation of GOES LST and SMAP Level-3 soil moisture retrievals (hereafter DA$_{T\theta}$) from Chapter 4. In general, the time series of OL closely follows the dynamics of in situ observations in both stations, indicating a good model performance. Given the limited time period of validation, no significant differences between the assimilation results can be highlighted. This evaluation is only indicative of how the different assimilation strategies perform. In Abrams, the SSM from OL has an ubRMSD of

0.042 m^3/m^3 and a bias of -0.025 m^3/m^3, which are improved in $DA_{T\theta}$ to 0.037 m^3/m^3 and -0.016 m^3/m^3, respectively. Assimilating TB observations instead of soil moisture retrievals reduces the estimation bias compared to in situ observations, particularly for DA_{TV}. $DA_{T\theta}$ yields SSM with relatively higher correlations with in situ measurements, which may result from the more direct relationship between soil moisture retrievals and in situ measurements. In Stillwater, the estimates are significantly influenced by the erroneous soil hydraulic properties used in the modeling as well as the disagreement in GPM data with in situ precipitation measurements [Lu et al., 2017]. Despite the influence, assimilating TB_H or TB_V shows slight improvement over assimilating soil moisture retrievals, particularly in reducing the estimation bias. This may indicate that TB observations indeed contain more information about soil moisture than soil moisture retrievals, which may have been filtered out in the retrieval process [De Lannoy and Reichle, 2016a].

The performance of data assimilation is also assessed for the second layer (5-15 cm) and root-zone soil moisture (hereafter RZSM) in Figure 5.5. A small difference exists between the thickness of soil column modeled (90 cm) and observed (100 cm). To calculate RZSM, the model simulations are averaged weighted by their respective layer thicknesses to derive a RZSM for the 0-90 cm soil column. The in situ soil moisture measurements are first linearly interpolated to get a soil moisture profile, and then integrated to get a RZSM for the 0-100 cm soil column. All assimilation strategies show correction of model simulations towards the independent measurements, particularly in the second layer where the correlation with surface soil moisture is stronger. Large bias exists between model simulations and in situ measurements for RZSM, which mainly comes from the initialization error of soil moisture profile, and the assimilation system is not designed to quickly undo this type of bias. In this experiment, the initial soil moisture profile is assumed uniform with randomly generated soil moisture, since little is known about the initial wetness condition of the soil column. SMAP observations are assimilated before the deep layer soil moisture has reached its climatological values. As a result, the updated deep layer soil moisture will be lower than the truth. In addition, in situ observations suggest that soil is saturated in the deepest layer with little evidence of dynamics, which further contributes to the large bias.

5.3.3. FLUX ESTIMATION

The 30-min *H* and *LE* estimates are assessed against in situ measurements at the four flux stations in Figure 5.6. All three assimilation strategies show improvement over OL simulations, particularly for *LE* estimates, which relates to a better characterization of soil moisture dynamics. Flux estimates from the three assimilation strategies are in general very similar. $DA_{T\theta}$ tends to yield higher correlations, which may result from the relatively higher correlations in soil moisture estimates (Figure 5.4). DA_{TV} slightly outperforms DA_{TH}, indicated by the smaller RMSD and higher correlation, but the difference is not significant. *H* and *LE* estimates at daytime (09:00-16:00 LT) scale yield similar results. The respective contribution of assimilating soil moisture and LST data to flux improvement has been explored in Lu et al. [2017]. When only LST data are assimilated, the RMSDs for flux estimates are very large since soil moisture is poorly simulated. In the soil moisture-only assimilation case, the modeled fluxes are well correlated to in situ

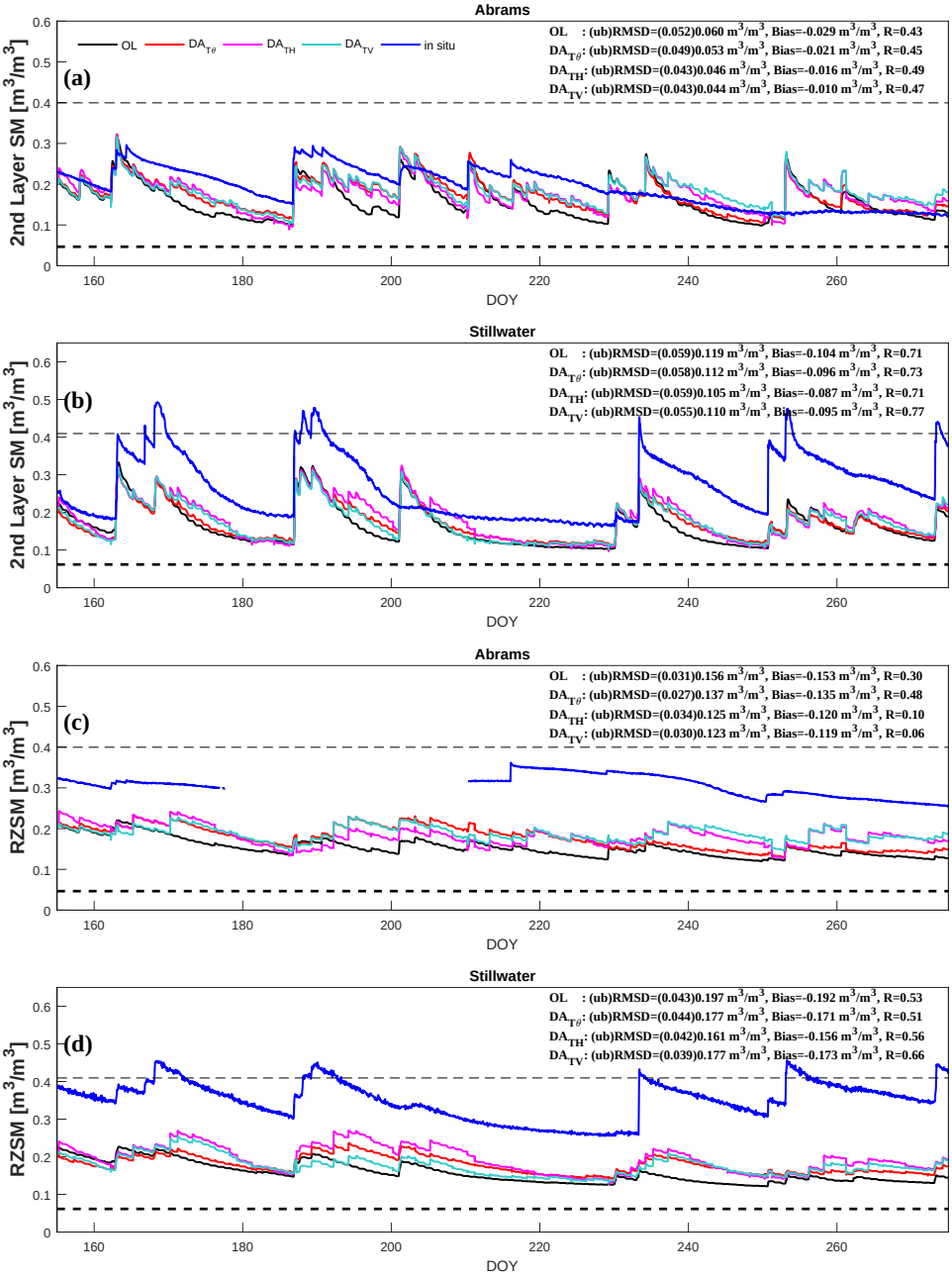

Figure 5.5: As of Figure 5.4 but for the second layer (5-15 cm, a-b) and root-zone soil moisture (c-d) assessment.

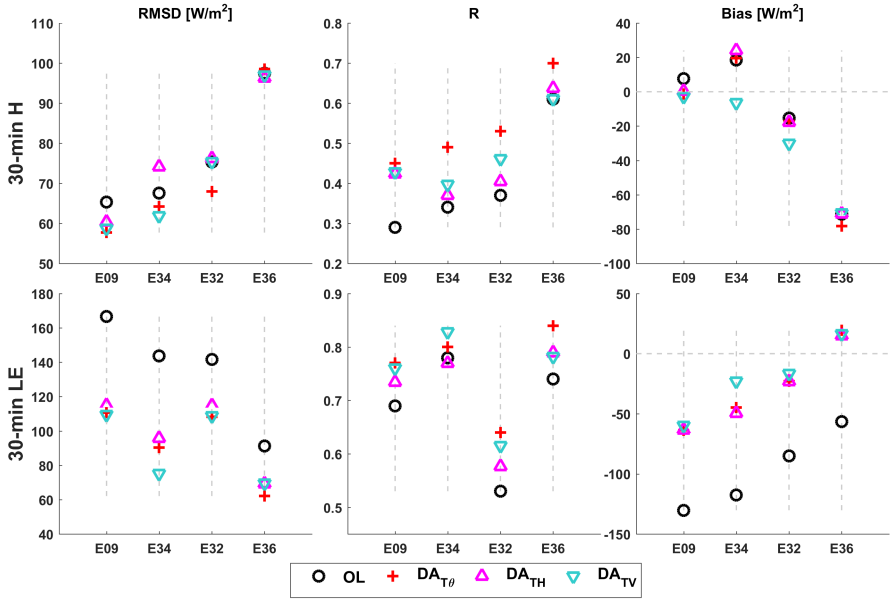

Figure 5.6: Assessment of 30-min H and LE estimates from OL, DA$_{T\theta}$, DA$_{TH}$ and DA$_{TV}$ at four flux stations during the study period.

observations, but the estimation bias is very high for both H and LE since the parameters cannot be updated. Overall, assimilation of LST and soil moisture information has the best performance.

Figure 5.7 shows the KGE between 30-min flux estimates from each pair of assimilation strategies to check the consistency between algorithms. It is demonstrated that the KGE between DA$_{TH}$ or DA$_{TV}$ and DA$_{T\theta}$ is generally above 0.8, which indicates a good agreement. The KGE in the northern part of the study area is slightly lower, which may be influenced by the soil moisture patterns. In the northern part, the soil is relatively wetter, which limits the magnitude of H. As a result, a small difference in H could lead to large differences in the statistical metrics, thus KGE gets lower. The KGE for LE is above 0.9 for most of the area, indicating a very good agreement between different assimilation strategies. The KGE is slightly lower in the northeast, where the vegetation is very dense. Similar results are obtained for results at daytime scale. This again highlights the influence from vegetation on the model performance. Overall, DA$_{TH}$ and DA$_{TV}$ yield very similar flux estimates across the study area for both H and LE.

The estimated time series of areal mean C_{HN} and EF are plotted in Figure 5.8. The estimated C_{HN} and EF follow the same temporal dynamics and are very close to each other in the magnitude. This again proves the similarities in the flux estimates. Although C_{HN} is also influenced by the evolution of other parameters, its time series is mainly dominated by LAI dynamics [Lu et al., 2017], while EF time series closely resembles the soil moisture dynamics. Around DOY 190 and 260 the parameter estimation differences are relatively large, which is mainly caused by the large differences in soil moisture es-

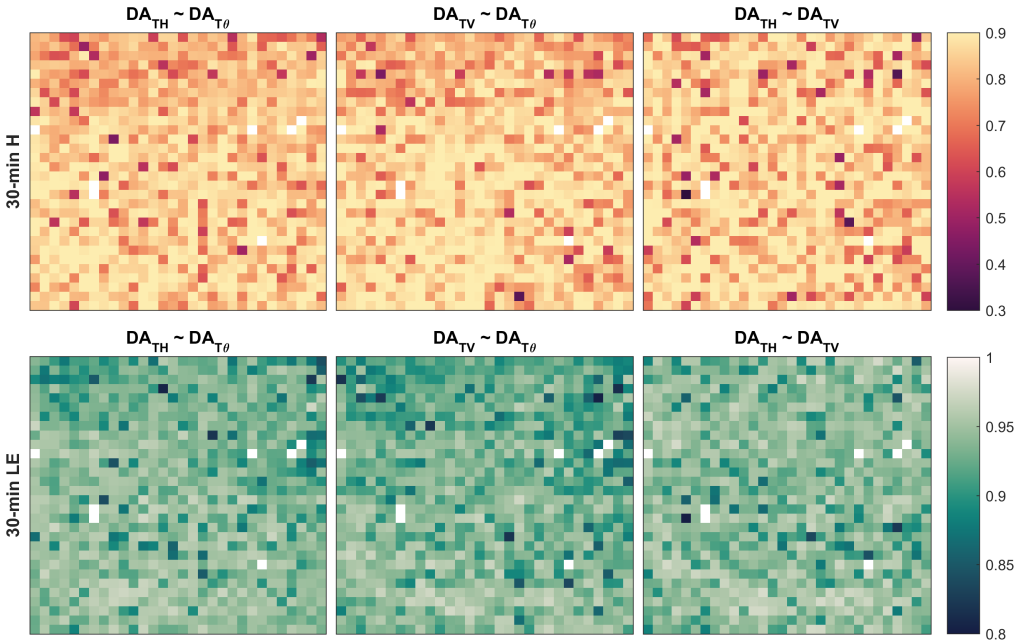

Figure 5.7: Intercomparison of the KGEs of 30-min H and LE estimates from $DA_{T\theta}$, DA_{TH} and DA_{TV}.

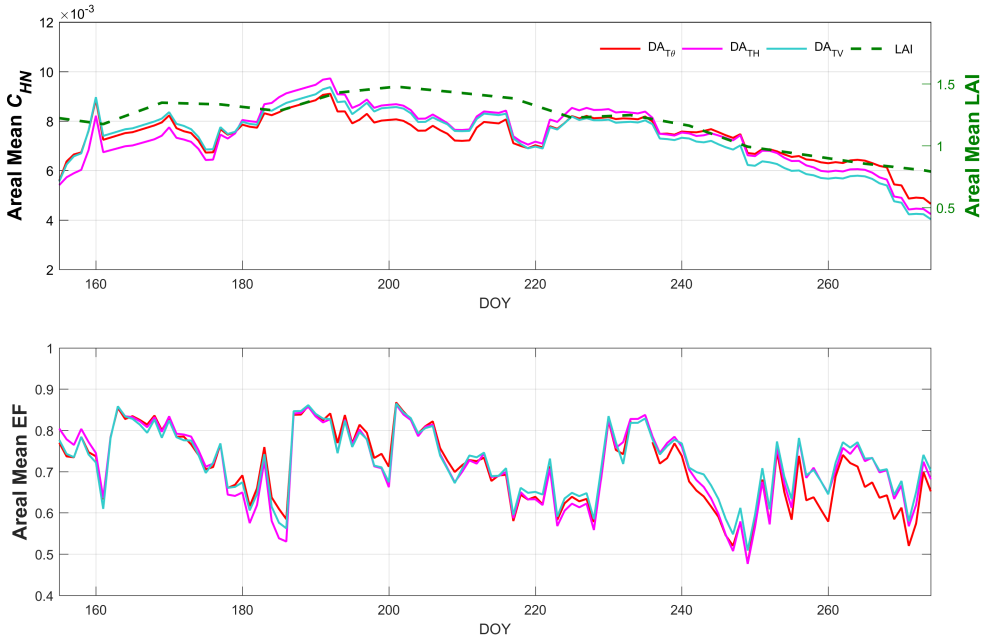

Figure 5.8: Time series of estimated areal mean C_{HN} and EF from $DA_{T\theta}$, DA_{TH} and DA_{TV}.

timates. Since soil moisture simulation influences flux estimates by constraining EF, the estimated EFs will be very similar when the differences in soil moisture estimates from different assimilation strategies are not pronounced, given the ±0.2 variation range. Consequently, the influence on C_{HN} and flux estimates is limited.

5.4. CONCLUSIONS

In this chapter, the water and heat transfer model is coupled to a radiative transfer model (RTM), and SMAP brightness temperature (TB) data and GOES LST data are assimilated together to improve surface heat flux estimates. Either TB at horizontal (TB_H) or vertical (TB_V) polarization is assimilated along with GOES LST data, and the estimates are compared to in situ observations and the results from Chapter 4 in which SMAP soil moisture retrievals were assimilated. The aim is to examine if the assimilation of physically consistent TB and LST data could yield improved surface heat flux estimates.

The agreement between the modeled soil moisture and the corresponding TB simulations is higher for TB_V than for TB_H, which may result from the lower sensitivity to biomass and surface roughness for vertical polarization. Analysis of the TB time series of the differences between OL simulations and SMAP observations suggests that the difference between simulation and observation is to some extent related to the soil moisture condition.

All three assimilation strategies improve surface soil moisture estimates compared to the OL simulation. DA_{TH} and DA_{TV} lead to smaller estimation bias, while $DA_{T\theta}$ yields larger correlations with in situ observations. Improvement is also seen in deeper layers, particularly for TB assimilation, though to a lesser degree than at the surface.

Assimilation also leads to improved H and LE estimates compared to OL estimates. $DA_{T\theta}$, DA_{TH} and DA_{TV} yield very similar flux estimates at both daytime and 30-min scale, particularly for LE estimates. The quality of surface heat flux estimates is mainly determined by GOES LST observations. Small differences in soil moisture estimates from different assimilation strategies have limited influence on the flux estimates.

It is worth noting that the performance of TB assimilation depends to a large extent on the bias correction as well as the characterization of model and observation errors. In this experiment, an RTM similar to the one used in the SMAP Level-2/3 soil moisture retrieval is used for TB forward simulation. Using another RTM with a different parameterization may lead to slightly different results. Regional optimization of parameters or dynamic online bias correction may also improve flux estimates.

6

CAN ESTIMATES BE IMPROVED BY ENHANCING THE SPATIO-TEMPORAL RESOLUTION OF SOIL MOISTURE OBSERVATIONS?

This chapter is based on:

Lu, Y., J. Dong, S. C. Steele-Dunne, Impact of soil moisture data resolution on soil moisture and surface heat flux estimates through data assimilation. (*submitted*)

6.1. INTRODUCTION

PREVIOUS chapters have demonstrated that although SMAP observations are very coarse in space and time, it is essential for successful soil moisture and surface heat flux estimation. As a result of the abundance of data sources, soil moisture data of higher spatial or temporal resolution have become possible. On one hand, soil moisture observations can be obtained at higher spatial resolution through active microwave remote sensing or downscaling procedures from coarse observations, which should be able to better characterize the spatial heterogeneity of soil moisture. On the other hand, multi-source soil moisture data from different remote sensing platforms contain complementary information on soil moisture dynamics, which provides great potential for better depicting the temporal evolution of soil moisture through data fusion. This provides great opportunity to explore the question that given observations at finer spatial or temporal resolution, how much improvement can be expected in soil moisture and surface heat flux estimates.

In this chapter, two experiments are conducted to evaluate the impact of spatial and temporal resolution of soil moisture observations. In the first experiment, SMAP Level-3 enhanced passive soil moisture product at 9-km resolution is assimilated. In the second experiment, a merged soil moisture product from SMAP and SMOS-IC data at 36-km resolution is used for assimilation. Results from both experiments are compared to those from assimilating SMAP Level-3 36-km soil moisture data in Chapter 4. The study area and test period are the same as those used in Chapter 4 to facilitate comparison.

6.2. MATERIALS AND METHODS

6.2.1. SMAP ENHANCED PASSIVE MICROWAVE SOIL MOISTURE PRODUCT

SMAP Level-3 enhanced passive microwave soil moisture product (L3_SM_P_E) distinguishes itself from the Level-3 passive microwave soil moisture product (L3_SM_P) in that the soil moisture retrievals are posted on 9-km grids instead of 36-km grids. This is done by first interpolating the original Level-1B TB observations using the Backus-Gilbert optimal interpolation technique [Chan et al., 2018]. This is to take advantage of the overlapping radiometer footprints. The interpolated TB 'observations' are then used as the input to the baseline algorithm to generate soil moisture retrievals at 9-km resolution. Comparison against in situ observations suggests that the performance of the 9-km enhanced soil moisture product is comparable to that of the 36-km soil moisture product [Chan et al., 2018].

6.2.2. SMOS-IC SOIL MOISTURE PRODUCT

SMOS-IC (SMOS-INRA-CESBIO) is an alternative soil moisture product generated based on the SMOS mission. It differs from the operational SMOS Level-3 soil moisture product in the treatment of heterogeneous grid cells. The main goal of this product is to be as independent as possible from ancillary data. To achieve this goal, SMOS-IC considers grid cells as homogeneous to avoid uncertainties caused by ancillary data which are used to characterize the heterogeneity of the grid cells. In addition, the schemes used for vegetation scattering albedo and soil roughness correction are also different. SMOS-IC product is posted on the same grid cells with SMOS data. Comparison against ECMWF (Euro-

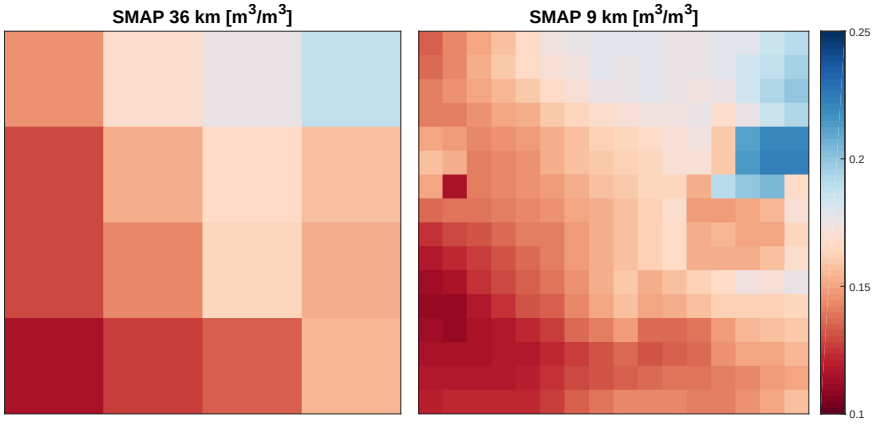

Figure 6.1: Observed areal mean surface soil moisture (SSM) during the study period from SMAP 36-km (L3_SM_P) product and 9-km (L3_SM_P_E) product.

pean Center for Medium range Weather Forecasting) soil moisture outputs suggests that SMOS-IC product yields higher correlations and lower ubRMSD (unbiased RMSD) than the operational SMOS soil moisture product over most pixels globally [Fernandez-Moran et al., 2017]. Here SMOS-IC data are used in a data fusion process to fill in the gaps of SMAP 36-km soil moisture observations between two descending overpasses.

6.2.3. EXPERIMENT SETUP

The methodology used is the same with that used in Chapter 4. In the first experiment (hereafter DA_{9km}), the study area is covered by 16×16 SMAP grid cells at 9-km resolution. A similar CDF-matching bias correction is performed, and soil moisture data assimilation is conducted for each 9-km grid cell separately. In the second experiment (hereafter DA_{merge}), the SMOS-IC data are first interpolated to 36-km resolution. The interpolated SMOS-IC data are then used to fill in the gaps of SMAP observations to achieve higher temporal resolution. Before the gap-filling procedure, SMAP and SMOS-IC data are first corrected for bias using CDF-matching. For days when only SMOS-IC data are available, the data are inserted into the SMAP data stream as additional 'observations'. On days with both SMAP and SMOS overpasses, SMOS-IC data are not used. This is to enhance the temporal resolution of soil moisture data while minimizing the perturbation of the original SMAP data series. It should be noted that the aim is not to find out the optimal approach for SMAP and SMOS-IC data fusion but to evaluate the impact on the assimilation results when more frequent soil moisture sampling is available. The soil moisture and surface heat flux estimates from the two experiments are compared to those from assimilating only SMAP 36-km soil moisture product (hereafter DA_{36km}).

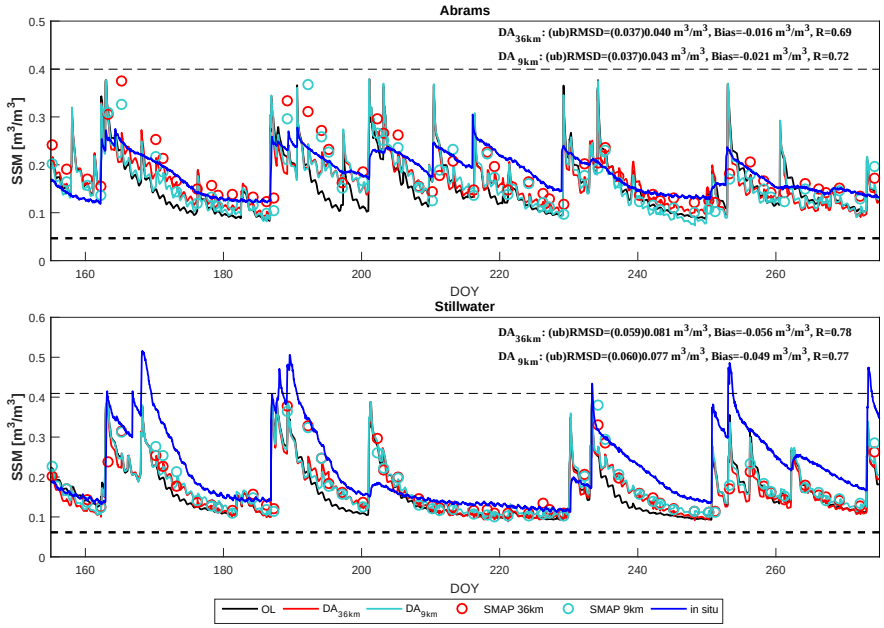

Figure 6.2: Assessment of SSM estimates from DA_{36km} and DA_{9km} against in situ measurements. The thick and thin dashed lines represent residual and saturated soil moisture used in the modeling, respectively.

6.3. RESULTS AND DISCUSSION

6.3.1. IMPROVING SPATIAL RESOLUTION OF SOIL MOISTURE OBSERVATIONS

The observed areal mean SSM during the study period is plotted in Figure 6.1 to examine the consistency and difference between the SMAP 36-km (L3_SM_P) product and 9-km (L3_SM_P_E) product. Both products show similar SSM patterns in the study area, indicating a clear dry-wet gradient from the southwest to the northeast. The areal mean SSM values generally agree well with each other, while the SMAP 9-km product better characterizes the spatial heterogeneity of SSM as a result of the enhanced resolution. The largest difference appears in the northeast of the area (grid cell (2,1) of the SMAP 36-km product), which is influenced by the relatively high fraction of water body. In this grid cell, a large lake exists in the northern part, which makes the SSM retrieval more difficult at finer spatial resolution. The soil moisture retrievals in this area therefore should be used with caution.

The SSM estimates from DA_{36km} and DA_{9km} are assessed at Abrams and Stillwater in Figure 6.2. The difference between SMAP 36-km and 9-km soil moisture observations are generally very small, particularly in Stillwater where there are many long dry-down events during the study period. The maximum difference however, can reach over 0.05 m^3/m^3 in both stations on a couple of days. The large differences mainly occur after rain events, which may be caused by the SSM heterogeneity within the 36-km footprint caused by the uneven distribution of precipitation and soil hydraulic properties. In terms of statistical metrics, DA_{9km} doesn't exhibit improvement over DA_{36km}. This may

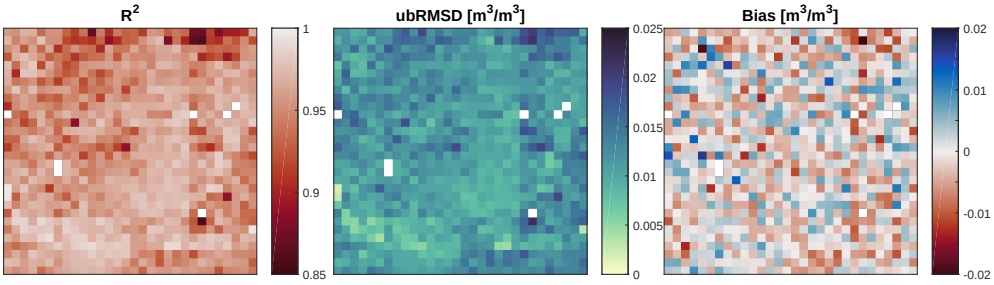

Figure 6.3: Statistical comparison of 30-min SSM time series from DA_{9km} with those from DA_{36km}.

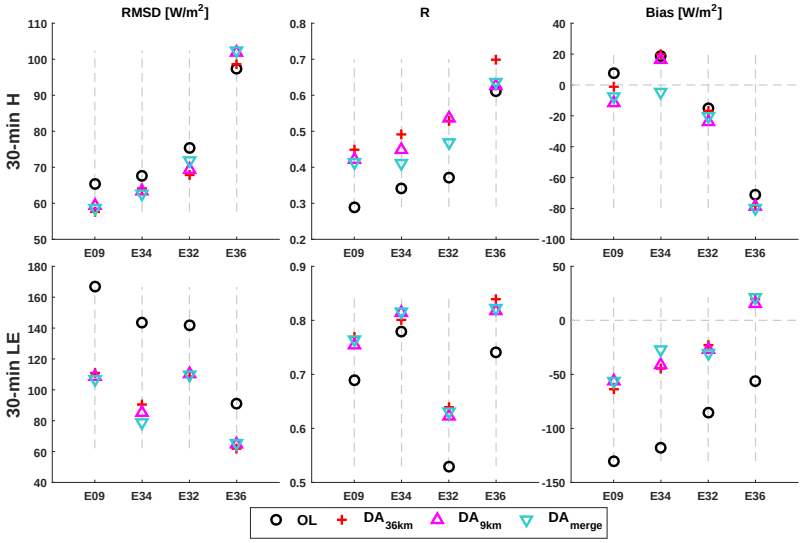

Figure 6.4: Comparison of 30-min H and LE estimates from DA_{36km}, DA_{9km} and DA_{merge} at four flux stations.

imply that the spatial variation of SSM is small within one 36-km grid cell in the study area, and that the SSM estimates are to a large extent dependent on the quality of the precipitation input. As a result, assimilating soil moisture data with enhanced spatial resolution only leads to limited improvement in SSM estimates, despite the finer spatial patterns the data set reveals.

The 30-min SSM estimates from DA_{9km} are compared with those from DA_{36km} in Figure 6.3. Over most of the area the R^2 is over 0.95, indicating a very good agreement in the estimated SSM dynamics. This is confirmed by the small ubRMSD and bias metrics in the study area. In general, assimilating SMAP SSM product at either 36-km or 9-km scale yields very similar SSM estimates.

Figure 6.4 compares the 30-min H and LE estimates from OL simulation, DA_{36km} and DA_{9km}. Flux estimates from DA_{9km} are very similar with those from DA_{36km} for both H and LE. This is natural since the soil moisture estimates from the two strategies are very similar. As a result, the constraints put on surface energy partitioning are alike, leading

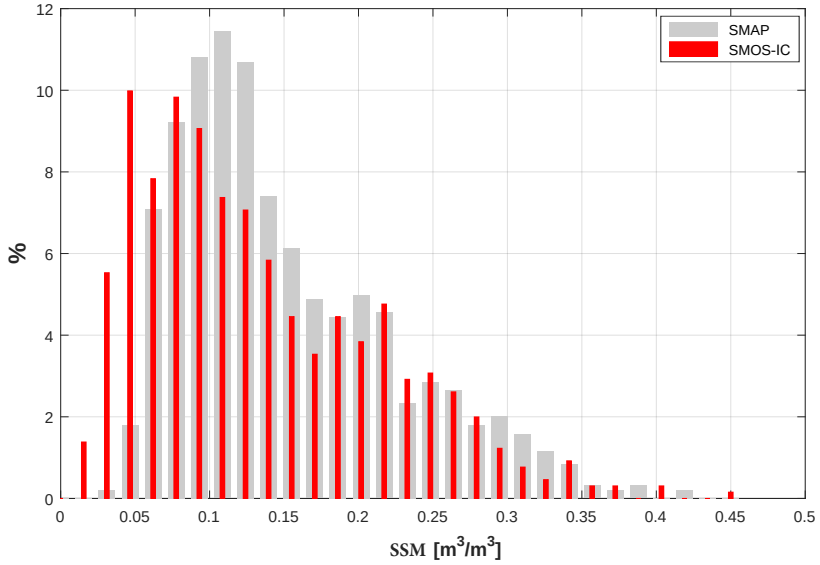

Figure 6.5: Histograms of SMAP L3_SM_P product and SMOS-IC product in the study area during the study period at 36-km scale.

to comparable flux estimates. The same conclusion can be drawn from evaluation at daytime scale (not shown).

6.3.2. IMPROVING TEMPORAL RESOLUTION OF SOIL MOISTURE OBSERVATIONS

The histograms of SSM from SMAP L3_SM_P product and SMOS-IC product (rescaled to 36-km resolution) are plotted in Figure 6.5 to check the consistency between the two products. SMAP L3_SM_P product shows a slight wet bias compared to the SMOS-IC product. The observed SSM from both products fall in the same range and exhibits similar distribution. Overall the two products agree very well with each other, which lays a good basis for data fusion.

The availabilities of the SMAP L3_SM_P product and SMOS-IC product in the 16 grid cells during the study period are shown in Figure 6.6. On average, there are 59 SMAP L3_SM_P observations and 40.7 SMOS-IC observations available during the study period for each grid cell. When the two products are merged, the mean available observations increase to 83.2 (41% increase), which will facilitate the characterization of soil moisture dynamics.

The SSM estimates from DA_{36km} and DA_{merge} are assessed at two soil moisture stations in Figure 6.7. The difference between the two strategies is most evident in the first and last days of the study period when there are more frequent additional observations from SMOS-IC. As a result, the SSM estimates from DA_{merge} are more strongly corrected towards the observations, which is also revealed by the reduced bias. In terms of sta-

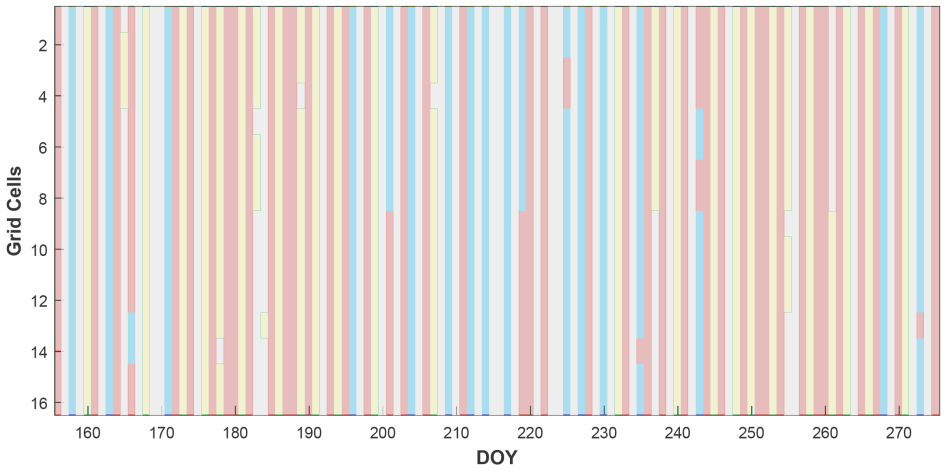

Figure 6.6: The availabilities of the SMAP L3_SM_P product and SMOS-IC product in the study area during the study period. The colors indicate (red) only SMAP L3_SM_P data available, (yellow) only SMOS-IC data available, (blue) both data available and (gray) no data available, respectively.

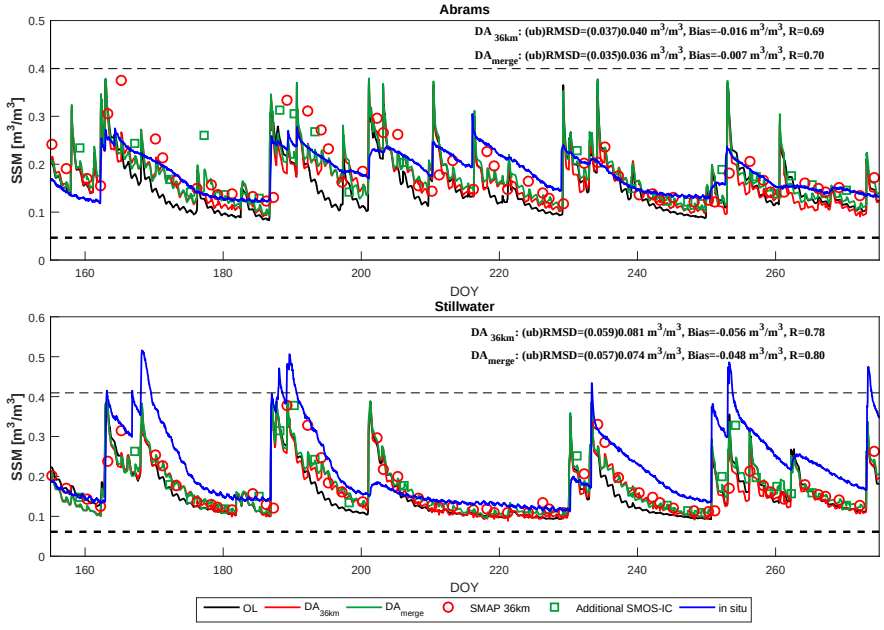

Figure 6.7: Assessment of SSM estimates from DA_{36km} and DA_{merge} against in situ measurements. The thick and thin dashed lines represent residual and saturated soil moisture used in the modeling, respectively.

tistical metrics, the improvement by assimilating merged SSM product is evident. The ubRMSD, RMSD, bias and R are all improved after assimilation, while the largest improvement is seen in the bias metric. This is mainly caused by the stronger constraint on soil moisture simulation through more frequent SSM assimilation.

30-min H and LE estimates from DA_{36km} and DA_{merge} are also compared in Figure 6.4. Despite the slight improvement in soil moisture estimates, no improvement is seen in the H and LE estimates from DA_{merge} compared to those from DA_{36km}. Since soil moisture influences flux estimation mainly through constraints on the EF, the EF estimates will not differ too much as a result of the limited improvement in soil moisture as well as the ±0.2 uncertainties given in EF estimation. As a result, the influence of slightly improved soil moisture estimates on flux estimates is limited. The comparison is similar at daytime scale (not shown).

6.4. CONCLUSIONS

In this chapter, two assimilation experiments are conducted and compared to the previous study which assimilated GOES LST data with SMAP L3_SM_P product at 36-km scale (DA_{36km}). In the first experiment (DA_{9km}), SMAP L3_SM_P_E product at 9-km is assimilated, while in the second experiment (DA_{merge}) a merged product from SMAP L3_SM_P and SMOS-IC data is used. This is to investigate the impact of enhancing the spatial or temporal resolution of soil moisture observations on the soil moisture and flux estimates.

Although the 9-km SMAP L3_SM_P_E product could better characterize the spatial heterogeneity of soil moisture, the SSM estimates are very similar to those from DA_{36km}. This may imply that at the scale of remote sensing soil moisture observations the SSM estimates are to a large extent influenced by other factors such as precipitation input, therefore the improvement in soil moisture estimates by enhancing the soil moisture observations to 9-km scale is limited.

Assimilating the merged soil moisture product outperforms all other assimilation strategies in soil moisture estimates at the two soil moisture stations. This benefits from the stronger constraints put on soil moisture dynamics. As a result of the enhanced temporal sampling frequency, soil moisture states are updated more frequently in DA_{merge}, which prevents the simulation error from becoming too large. This indicates that soil moisture data with enhanced temporal resolution indeed contain useful information that helps to improve soil moisture estimates.

Despite the differences in soil moisture estimates, no evident improvement in surface heat flux estimates can be seen from either DA_{9km} or DA_{merge}. This is expected in DA_{9km} since the soil moisture estimates are similar with those from DA_{36km}. In DA_{merge}, the improvement in soil moisture estimates does not lead to improvement in flux estimates as a result of the uncertainties in EF estimates. This may imply that surface energy partitioning cannot be further improved by improving soil moisture states alone, and that information from other data sources should be incorporated to further constrain EF, e.g., vegetation dynamics [Bateni et al., 2014].

Here the merged soil moisture data are generated directly from the SMAP and SMOS-IC soil moisture products for simplicity. It should be noted that the aim is not to find the optimal approach for SMAP and SMOS-IC data fusion but to evaluate the impact

when more frequent soil moisture sampling becomes available. A more rigorous data fusion should convert brightness temperature observations from SMOS to SMAP-like data using methods such as that proposed by De Lannoy et al. [2015] before performing soil moisture retrieval. The assimilation results are expected to be similar as a result of the similarity and consistency between the two missions.

7

CONCLUSIONS

7.1. KNOWLEDGE GENERATED

7.1.1. ON JOINT ASSIMILATION OF SOIL MOISTURE AND LST DATA

Surface heat fluxes are key to many aspects such as agricultural water management, climate science, land-atmosphere interaction and hydrological modeling, but the accurate estimation remains a problem. Previous studies have focused on assimilating LST data into heat transfer models to improve flux estimates. These methods perform poorly over wet or densely vegetated surfaces, since energy partitioning becomes energy-limited under such conditions. In this dissertation the heat transfer model is coupled to a water transfer model to facilitate the joint assimilation of in situ soil moisture and LST observations in Chapter 3. The value of incorporating soil moisture data is explored for the first time in depth through comparative assimilation studies. This is also the first study that utilizes the recently developed particle batch smoother (PBS) for surface heat flux estimation.

It is demonstrated that the PBS could effectively improve surface heat flux estimates by assimilating LST time series compared to a simulation-only case. When soil moisture data are jointly assimilated to further constrain EF, the flux estimates are greatly improved, particularly on wet conditions. A data-denial experiment suggests that the assimilation performance plateaus when over five LST observations are available in a LST-only assimilation case. The performance significantly improves when soil moisture observations are assimilated, particularly when LST observations are limited. This is instructive to the application with remote sensing data, in which LST observations from infrared sensors are often hampered by the presence of clouds.

7.1.2. ON THE APPLICATION WITH REMOTE SENSING DATA

To advance the developed methodology from an in situ application to a remote sensing application over a large area, many research gaps need to be bridged, in particular the difference in the spatio-temporal resolution between data sets. To solve this problem, a hybrid particle assimilation strategy is proposed, in which SMAP soil moisture retrievals

are assimilated using a particle filter and GOES LST time series is assimilated using an improved adaptive particle batch smoother (APBS). The reason is that remote sensing soil moisture data from passive microwave radiometers are much coarser than LST data from thermal bands in both space and time, therefore the information from soil moisture data will be masked out as a result of the LST dominance in numbers if assimilated together in a batch. The study is presented in Chapter 4 and is the first study to apply the PBS algorithm with remote sensing data.

It is demonstrated that the hybrid assimilation strategy successfully reconciles the resolution gap between soil moisture and LST data, and that surface heat fluxes are improved at both daytime and 30-min scale. In addition, by assimilating coarse soil moisture data the soil moisture estimates at fine resolution are also improved. A comparative study suggests that despite the very coarse spatio-temporal resolution, assimilating soil moisture data is crucial for reducing the soil moisture estimation bias caused by the uncertainties from forcing data, model structure and parameters. The proposed methodology is independent of ground measurements, therefore is easily transferable to other regions.

7.1.3. ON THE IMPACT OF DIFFERENT SOIL WETNESS DATA SETS

To eliminate the influence of inconsistent LST data used in SMAP soil moisture retrieval and model simulation, a study that directly assimilates brightness temperature (TB) observations from SMAP is conducted in Chapter 5. The state propagation model is coupled to a radiative transfer model (RTM), and TB from either horizontal or vertical polarization is assimilated together with GOES LST data.

The results demonstrate that the TB difference between model simulations and SMAP observations is to some extent related to the soil moisture condition, hence bias correction should ideally depend on the soil moisture state. Assimilating TB observations leads to smaller soil moisture estimation bias, while assimilating soil moisture retrievals yields larger correlations. Small differences in soil moisture estimates have limited influence on the flux estimates.

A further study is conducted on top of this to explore the impact of enhancing the spatial or temporal resolution of soil moisture data on the flux estimates. It is shown that the improvement is marginal by assimilating soil moisture data with finer spatial heterogeneity or more detailed temporal dynamics. This may indicate that no further improvement can be expected by using better soil moisture input. Other information sources need to be incorporated to further improve flux estimates (e.g., vegetation dynamics).

7.2. RECOMMENDATION FOR FUTURE RESEARCH

7.2.1. SOIL TEXTURE

Soil texture data are necessary to generate soil hydraulic properties and to facilitate radiative transfer modeling. The data used in this dissertation are provided at finer spatial resolution, therefore need to be processed using a spatial upscaling approach to derive data at the model resolution. During this process, uncertainties are introduced, which come from the non-linear relationship between soil hydraulic properties and soil tex-

ture. For example, the impact of aggregated soil texture data on the estimated soil hydraulic properties is highlighted in Chapter 4.

Using more spatially representative data sets should improve the soil moisture simulations and the assimilation estimates. Recently, a more advanced approach is proposed by Montzka et al. [2017] to scale soil hydraulic properties to individual grids, which may potentially reduce the uncertainties in the scaling processes.

7.2.2. VEGETATION DYNAMICS

Vegetation indices, including LAI and NDVI, are key input to the model framework. They dominate C_{HN} dynamics and govern the partitioning between soil evaporation and vegetation transpiration. In the current model, vegetation indices are obtained from MODIS products provided at relatively coarse temporal resolution (8-day or 16-day composite). The vegetation indices are linearly interpolated in time to get daily values, which may not well characterize the vegetation dynamics, particularly in the growing season. Using daily vegetation indices could improve the depiction of vegetation phenology, but no current products are available at such fine temporal resolution. Potential sources of vegetation dynamics include vegetation optical depth (VOD) data which are acquired from passive microwave remote sensing at finer temporal resolution (typically 2-3 days) but coarser spatial resolution.

Incorporating vegetation modeling may be a solution to this gap. Bateni et al. [2014] coupled a surface energy balance (SEB) model with a vegetation dynamics model (VDM) through the linkage between vegetation transpiration and photosynthesis, which facilitates joint assimilation of LST and fraction of photosynthetically active radiation absorbed by vegetation (FPAR) data. The key of this coupling is the LAI dynamics modeled by the VDM and used to solve the energy balance at the land surface. The coupling with VDM relieves the need for vegetation indices input, thus reduces the uncertainties introduced in the arbitrary temporal interpolation process. In addition, the synergy of surface energy partitioning, surface water movement and photosynthesis is tightened, which could potentially facilitate the assimilation of observations from other sources, such as vegetation indices, VOD and sun-induced chlorophyll fluorescence (SIF). Utilizing information from other data sources may further improve surface heat flux estimates, as is implied in Chapter 6.

7.2.3. APPLICATION ON CLOUDY DAYS

One fundamental assumption of this research is the self-preservation of daytime EF. This assumption has been extensively tested and proven robust under clear-sky conditions [Crago, 1996; Crago and Brutsaert, 1996; Gentine et al., 2007]. However, the assumption is invalid under cloudy-sky conditions, which represent more than half of the day-to-day weather [Jin, 2000]. Unlike clear-sky conditions, the diurnal behavior of EF under cloudy-sky conditions remains largely unexplored. Gentine et al. [2011] demonstrated that intermittent presence of clouds leads to large spikes in EF since solar radiation is attenuated, and that on very cloudy days, EF becomes very erratic. Peng et al. [2013] also confirmed the increased variability of diurnal EF with increasing cloud cover.

To estimate surface heat fluxes on cloudy days, a proper model to estimate EF under cloudy-sky conditions needs to be built. Although parameters cannot be updated

due to the limited availability of LST observations, improvement in surface heat fluxes is still expected if EF can be effectively approximated. This calls for the analysis of cloud influence on the reduction of solar radiation as well as on the evaporation processes. This is not within the scope of this research but is key to enhancing the applicability of this methodology to all-weather condition and may eventually lead to a consistent continent-scale surface heat flux product.

7.2.4. VEGETATION TYPE ON MODEL PERFORMANCE

This research as well as previous data assimilation studies have mainly focused on the application over grassland and woody savannah. A more detailed research is necessary to evaluate the performance of this methodology under different vegetation cover conditions (e.g., forest, shrubs, tundra, agricultural areas). In particular, focus should be given to the influence of vegetation cover on the constraint of soil moisture on EF. The vegetation height and canopy structure influence the incoming solar radiation partitioning as well as the radiometric temperature observed by satellites. The difference in root-zone depth also impacts the soil moisture simulation and the information contained in the observed surface soil moisture on evaporation estimation.

7.2.5. PARAMETERIZATION

In this dissertation, two parameters (a and b in Equation 4.11) are updated through LST assimilation to propagate C_{HN}, where a represents the influence from the soil and b characterizes the influence from vegetation density. Since the surface soil does not change dramatically over a short period, the variations of a is expected to be small. It is also demonstrated in Chapter 5 that although C_{HN} is also influenced by the parameters, its time series is mainly dominated by LAI dynamics. This implies that C_{HN} estimation may be further simplified by reducing the number of parameters to be updated, which would make the assimilation algorithm more robust. Further research should be conducted to form a look-up table for a for different soil texture as well as smaller and more physically reasonable ranges for b for different vegetation cover conditions and growth stages. This may introduce uncertainties of parameter spatial heterogeneity, but the uncertainties are expected to be manageable and can be mitigated by adding perturbations to daily LAI values.

7.2.6. BIAS CORRECTION

Bias correction of remote sensing soil moisture and TB data prior to data assimilation is essential for successful update of soil moisture state. A common practice is to use multi-year OL simulations and remote sensing observations to calculate the climatological difference between them. Here we only used data from 2015 for bias correction, due partially to the short record of the SMAP mission. Results demonstrate that bias estimated in this short period has limited influence on the estimated states. Using a longer test period should improve the robustness of bias correction and may lead to more statistically significant results.

REFERENCES

Abdolghafoorian, A., Farhadi, L., Bateni, S. M., Margulis, S., and Xu, T.: Characterizing the effect of vegetation dynamics on the bulk heat transfer coefficient to improve variational estimation of surface turbulent fluxes, Journal of Hydrometeorology, 18, 321–333, 2017.

Alavi, N., Warland, J. S., and Berg, A. A.: Assimilation of soil moisture and temperature data into land surface models: a survey, in: Data Assimilation for Atmospheric, Oceanic and Hydrologic Applications, pp. 429–448, Springer, 2009.

Allen, R. G., Tasumi, M., and Trezza, R.: Satellite-based energy balance for mapping evapotranspiration with internalized calibration (METRIC)-Model, Journal of Irrigation and Drainage Engineering, 133, 380–394, 2007.

Anderson, M., Norman, J., Diak, G., Kustas, W., and Mecikalski, J.: A two-source time-integrated model for estimating surface fluxes using thermal infrared remote sensing, Remote Sensing of Environment, 60, 195–216, 1997.

Anderson, M., Kustas, W., Norman, J., Hain, C., Mecikalski, J., Schultz, L., González-Dugo, M., Cammalleri, C., d'Urso, G., Pimstein, A., et al.: Mapping daily evapotranspiration at field to continental scales using geostationary and polar orbiting satellite imagery, Hydrology and Earth System Sciences, 15, 223–239, 2011.

Baldocchi, D., Falge, E., Gu, L., Olson, R., Hollinger, D., Running, S., Anthoni, P., Bernhofer, C., Davis, K., Evans, R., et al.: FLUXNET: A new tool to study the temporal and spatial variability of ecosystem-scale carbon dioxide, water vapor, and energy flux densities, Bulletin of the American Meteorological Society, 82, 2415–2434, 2001.

Bartalis, Z., Wagner, W., Naeimi, V., Hasenauer, S., Scipal, K., Bonekamp, H., Figa, J., and Anderson, C.: Initial soil moisture retrievals from the METOP-A Advanced Scatterometer (ASCAT), Geophysical Research Letters, 34, 2007.

Basara, J. B. and Crawford, K. C.: Linear relationships between root-zone soil moisture and atmospheric processes in the planetary boundary layer, Journal of Geophysical Research: Atmospheres (1984–2012), 107, ACL–10, 2002.

Bastiaanssen, W., Menenti, M., Feddes, R., and Holtslag, A.: A remote sensing surface energy balance algorithm for land (SEBAL). 1. Formulation, Journal of Hydrology, 212, 198–212, 1998a.

Bastiaanssen, W., Pelgrum, H., Wang, J., Ma, Y., Moreno, J., Roerink, G., and Van der Wal, T.: A remote sensing surface energy balance algorithm for land (SEBAL).: Part 2: Validation, Journal of Hydrology, 212, 213–229, 1998b.

Bateni, S. and Entekhabi, D.: Relative efficiency of land surface energy balance components, Water Resources Research, 48, 2012a.

Bateni, S. and Entekhabi, D.: Surface heat flux estimation with the ensemble Kalman smoother: Joint estimation of state and parameters, Water Resources Research, 48, 2012b.

Bateni, S. and Liang, S.: Estimating surface energy fluxes using a dual-source data assimilation approach adjoined to the heat diffusion equation, Journal of Geophysical Research: Atmospheres (1984–2012), 117, 2012.

Bateni, S., Entekhabi, D., and Castelli, F.: Mapping evaporation and estimation of surface control of evaporation using remotely sensed land surface temperature from a constellation of satellites, Water Resources Research, 49, 950–968, 2013a.

Bateni, S., Entekhabi, D., and Jeng, D.-S.: Variational assimilation of land surface temperature and the estimation of surface energy balance components, Journal of Hydrology, 481, 143–156, 2013b.

Bateni, S., Entekhabi, D., Margulis, S., Castelli, F., and Kergoat, L.: Coupled estimation of surface heat fluxes and vegetation dynamics from remotely sensed land surface temperature and fraction of photosynthetically active radiation, Water Resources Research, 50, 8420–8440, 2014.

Bell, J. E., Palecki, M. A., Baker, C. B., Collins, W. G., Lawrimore, J. H., Leeper, R. D., Hall, M. E., Kochendorfer, J., Meyers, T. P., Wilson, T., et al.: US Climate Reference Network soil moisture and temperature observations, Journal of Hydrometeorology, 14, 977–988, 2013.

Bengtsson, T., Bickel, P., Li, B., et al.: Curse-of-dimensionality revisited: Collapse of the particle filter in very large scale systems, in: Probability and Statistics: Essays in honor of David A. Freedman, pp. 316–334, Institute of Mathematical Statistics, 2008.

Betts, A. K. and Ball, J. H.: FIFE surface climate and site-average dataset 1987-89, Journal of the Atmospheric Sciences, 55, 1091–1108, 1998.

Boni, G., Entekhabi, D., and Castelli, F.: Land data assimilation with satellite measurements for the estimation of surface energy balance components and surface control on evaporation, Water Resources Research, 37, 1713–1722, 2001.

Cai, X., Pan, M., Chaney, N. W., Colliander, A., Misra, S., Cosh, M. H., Crow, W. T., Jackson, T. J., and Wood, E. F.: Validation of SMAP soil moisture for the SMAPVEX15 field campaign using a hyper-resolution model, Water Resources Research, 53, 3013–3028, 2017.

Campbell, G. S.: Soil physics with BASIC: transport models for soil-plant systems, vol. 14, Elsevier, 1985.

Caparrini, F., Castelli, F., and Entekhabi, D.: Mapping of land-atmosphere heat fluxes and surface parameters with remote sensing data, Boundary-Layer Meteorology, 107, 605–633, 2003.

Caparrini, F., Castelli, F., and Entekhabi, D.: Estimation of surface turbulent fluxes through assimilation of radiometric surface temperature sequences, Journal of Hydrometeorology, 5, 145–159, 2004a.

Caparrini, F., Castelli, F., and Entekhabi, D.: Variational estimation of soil and vegetation turbulent transfer and heat flux parameters from sequences of multisensor imagery, Water Resources Research, 40, 2004b.

Castelli, F., Entekhabi, D., and Caporali, E.: Estimation of surface heat flux and an index of soil moisture using adjoint-state surface energy balance, Water Resources Research, 35, 3115–3125, 1999.

Chan, S., Bindlish, R., O'Neill, P., Jackson, T., Njoku, E., Dunbar, S., Chaubell, J., Piepmeier, J., Yueh, S., Entekhabi, D., et al.: Development and assessment of the SMAP enhanced passive soil moisture product, Remote Sensing of Environment, 204, 931–941, 2018.

Chan, S. K., Bindlish, R., O'Neill, P. E., Njoku, E., Jackson, T., Colliander, A., Chen, F., Burgin, M., Dunbar, S., Piepmeier, J., et al.: Assessment of the SMAP passive soil moisture product, IEEE Transactions on Geoscience and Remote Sensing, 54, 4994–5007, 2016.

Chirouze, J., Boulet, G., Jarlan, L., Fieuzal, R., Rodriguez, J., Ezzahar, J., Er-Raki, S., Bigeard, G., Merlin, O., Garatuza-Payan, J., et al.: Intercomparison of four remote-sensing-based energy balance methods to retrieve surface evapotranspiration and water stress of irrigated fields in semi-arid climate, Hydrology and Earth System Sciences, 18, 1165–1188, 2014.

Choudhury, B., Schmugge, T. J., Chang, A., and Newton, R.: Effect of surface roughness on the microwave emission from soils, Journal of Geophysical Research: Oceans, 84, 5699–5706, 1979.

Choudhury, B., Schmugge, T., and Mo, T.: A parameterization of effective soil temperature for microwave emission, Journal of Geophysical Research: Oceans, 87, 1301–1304, 1982.

Choudhury, B., Idso, S., and Reginato, R.: Analysis of an empirical model for soil heat flux under a growing wheat crop for estimating evaporation by an infrared-temperature based energy balance equation, Agricultural and Forest Meteorology, 39, 283–297, 1987.

Choudhury, B. J.: Relationships between vegetation indices, radiation absorption, and net photosynthesis evaluated by a sensitivity analysis, Remote Sensing of Environment, 22, 209–233, 1987.

Colliander, A., Jackson, T., Bindlish, R., Chan, S., Das, N., Kim, S., Cosh, M., Dunbar, R., Dang, L., Pashaian, L., et al.: Validation of SMAP surface soil moisture products with core validation sites, Remote Sensing of Environment, 191, 215–231, 2017.

Crago, R. and Brutsaert, W.: Daytime evaporation and the self-preservation of the evaporative fraction and the Bowen ratio, Journal of Hydrology, 178, 241–255, 1996.

Crago, R. D.: Conservation and variability of the evaporative fraction during the daytime, Journal of Hydrology, 180, 173–194, 1996.

Crow, W. T. and Kustas, W. P.: Utility of assimilating surface radiometric temperature observations for evaporative fraction and heat transfer coefficient retrieval, Boundary-Layer Meteorology, 115, 105–130, 2005.

Crow, W. T., Koster, R. D., Reichle, R. H., and Sharif, H. O.: Relevance of time-varying and time-invariant retrieval error sources on the utility of spaceborne soil moisture products, Geophysical Research Letters, 32, 2005.

Crow, W. T., Lei, F., Hain, C., Anderson, M. C., Scott, R. L., Billesbach, D., and Arkebauer, T.: Robust estimates of soil moisture and latent heat flux coupling strength obtained from triple collocation, Geophysical Research Letters, 42, 8415–8423, 2015.

Das, N.: SMAP Ancillary Data Report: Soil Attributes, Jet Propulsion Lab., California Inst. Technol., Pasadena, CA, USA, JPL D-53058, 2013.

Das, N. N., Entekhabi, D., and Njoku, E. G.: An algorithm for merging SMAP radiometer and radar data for high-resolution soil-moisture retrieval, Geoscience and Remote Sensing, IEEE Transactions on, 49, 1504–1512, 2011.

Das, N. N., Entekhabi, D., Dunbar, R. S., Njoku, E. G., and Yueh, S. H.: Uncertainty Estimates in the SMAP Combined Active–Passive Downscaled Brightness Temperature, IEEE Transactions on Geoscience and Remote Sensing, 54, 640–650, 2016.

De Lannoy, G. J. and Reichle, R. H.: Assimilation of SMOS brightness temperatures or soil moisture retrievals into a land surface model, Hydrology and Earth System Sciences, 20, 4895, 2016a.

De Lannoy, G. J. and Reichle, R. H.: Global assimilation of multiangle and multipolarization SMOS brightness temperature observations into the GEOS-5 catchment land surface model for soil moisture estimation, Journal of Hydrometeorology, 17, 669–691, 2016b.

De Lannoy, G. J., Houser, P. R., Pauwels, V., and Verhoest, N. E.: State and bias estimation for soil moisture profiles by an ensemble Kalman filter: Effect of assimilation depth and frequency, Water Resources Research, 43, 2007a.

De Lannoy, G. J., Reichle, R. H., Houser, P. R., Pauwels, V., and Verhoest, N. E.: Correcting for forecast bias in soil moisture assimilation with the ensemble Kalman filter, Water Resources Research, 43, 2007b.

De Lannoy, G. J., Reichle, R. H., Peng, J., Kerr, Y., Castro, R., Kim, E. J., and Liu, Q.: Converting between SMOS and SMAP level-1 brightness temperature observations over nonfrozen land, IEEE Geoscience and Remote Sensing Letters, 12, 1908–1912, 2015.

DeChant, C. M. and Moradkhani, H.: Examining the effectiveness and robustness of sequential data assimilation methods for quantification of uncertainty in hydrologic forecasting, Water Resources Research, 48, 2012.

Dirmeyer, P. A., Zeng, F. J., Ducharne, A., Morrill, J. C., and Koster, R. D.: The sensitivity of surface fluxes to soil water content in three land surface schemes, Journal of Hydrometeorology, 1, 121–134, 2000.

Dobson, M. C., Ulaby, F. T., Hallikainen, M. T., and El-Rayes, M. A.: Microwave dielectric behavior of wet soil-Part II: Dielectric mixing models, IEEE Transactions on Geoscience and Remote Sensing, pp. 35–46, 1985.

Dong, J., Steele-Dunne, S. C., Judge, J., and van de Giesen, N.: A particle batch smoother for soil moisture estimation using soil temperature observations, Advances in Water Resources, 83, 111–122, 2015.

Dong, J., Steele-Dunne, S. C., Ochsner, T. E., Hatch, C. E., Sayde, C., Selker, J., Tyler, S., Cosh, M. H., and van de Giesen, N.: Mapping high-resolution soil moisture and properties using distributed temperature sensing data and an adaptive particle batch smoother, Water Resources Research, 52, 7690–7710, 2016a.

Dong, J., Steele-Dunne, S. C., Ochsner, T. E., and van de Giesen, N.: Estimating soil moisture and soil thermal and hydraulic properties by assimilating soil temperatures using a particle batch smoother, Advances in Water Resources, 91, 104–116, 2016b.

Dorigo, W., Gruber, A., De Jeu, R., Wagner, W., Stacke, T., Loew, A., Albergel, C., Brocca, L., Chung, D., Parinussa, R., et al.: Evaluation of the ESA CCI soil moisture product using ground-based observations, Remote Sensing of Environment, 162, 380–395, 2015.

Duan, Q., Schaake, J., and Koren, V.: FIFE 1987 water budget analysis, Journal of Geophysical Research: Atmospheres (1984–2012), 101, 7197–7207, 1996.

Dunne, S. and Entekhabi, D.: Land surface state and flux estimation using the ensemble Kalman smoother during the Southern Great Plains 1997 field experiment, Water Resources Research, 42, 2006.

Dunne, S. C., Entekhabi, D., and Njoku, E. G.: Impact of multiresolution active and passive microwave measurements on soil moisture estimation using the ensemble Kalman smoother, IEEE Transactions on Geoscience and Remote Sensing, 45, 1016–1028, 2007.

Entekhabi, D., Rodriguez-Iturbe, I., and Castelli, F.: Mutual interaction of soil moisture state and atmospheric processes, Journal of Hydrology, 184, 3–17, 1996.

Entekhabi, D., Njoku, E. G., Neill, P. E., Kellogg, K. H., Crow, W. T., Edelstein, W. N., Entin, J. K., Goodman, S. D., Jackson, T. J., Johnson, J., et al.: The soil moisture active passive (SMAP) mission, Proceedings of the IEEE, 98, 704–716, 2010.

Entekhabi, D., Yueh, S., O'Neill, P., Kellogg, K., et al.: SMAP handbook, JPL Publication JPL, pp. 400–1567, 2014.

Evensen, G.: Sequential data assimilation with a nonlinear quasi-geostrophic model using Monte Carlo methods to forecast error statistics, Journal of Geophysical Research: Oceans, 99, 10 143–10 162, 1994.

Evensen, G. and Van Leeuwen, P. J.: An ensemble Kalman smoother for nonlinear dynamics, Monthly Weather Review, 128, 1852–1867, 2000.

Farhadi, L., Entekhabi, D., Salvucci, G., and Sun, J.: Estimation of land surface water and energy balance parameters using conditional sampling of surface states, Water Resources Research, 50, 1805–1822, 2014.

Farhadi, L., Entekhabi, D., and Salvucci, G.: Mapping land water and energy balance relations through conditional sampling of remote sensing estimates of atmospheric forcing and surface states, Water Resources Research, 52, 2737–2752, 2016.

Fernandez-Moran, R., Al-Yaari, A., Mialon, A., Mahmoodi, A., Al Bitar, A., De Lannoy, G., Rodriguez-Fernandez, N., Lopez-Baeza, E., Kerr, Y., and Wigneron, J.-P.: SMOS-IC: An alternative SMOS soil moisture and vegetation optical depth product, Remote Sensing, 9, 457, 2017.

Foken, T.: The energy balance closure problem: an overview, Ecological Applications, 18, 1351–1367, 2008.

Freitas, S. C., Trigo, I. F., Macedo, J., Barroso, C., Silva, R., and Perdigão, R.: Land surface temperature from multiple geostationary satellites, International Journal of Remote Sensing, 34, 3051–3068, 2013.

French, A. N., Schmugge, T. J., Kustas, W. P., Brubaker, K. L., and Prueger, J.: Surface energy fluxes over El Reno, Oklahoma, using high-resolution remotely sensed data, Water Resources Research, 39, 2003.

Gentine, P., Entekhabi, D., Chehbouni, A., Boulet, G., and Duchemin, B.: Analysis of evaporative fraction diurnal behaviour, Agricultural and Forest Meteorology, 143, 13–29, 2007.

Gentine, P., Entekhabi, D., and Polcher, J.: The diurnal behavior of evaporative fraction in the soil–vegetation–atmospheric boundary layer continuum, Journal of Hydrometeorology, 12, 1530–1546, 2011.

Gupta, H. V., Kling, H., Yilmaz, K. K., and Martinez, G. F.: Decomposition of the mean squared error and NSE performance criteria: Implications for improving hydrological modelling, Journal of Hydrology, 377, 80–91, 2009.

Hall, F. G., Huemmrich, K. F., Goetz, S. J., Sellers, P. J., and Nickeson, J. E.: Satellite remote sensing of surface energy balance: success, failures, and unresolved issues in FIFE, Journal of Geophysical Research: Atmospheres (1984–2012), 97, 19 061–19 089, 1992.

Holmes, T., De Rosnay, P., De Jeu, R., Wigneron, R.-P., Kerr, Y., Calvet, J.-C., Escorihuela, M., Saleh, K., and Lemaître, F.: A new parameterization of the effective temperature for L band radiometry, Geophysical Research Letters, 33, 2006.

Holmes, T. R., Hain, C. R., Crow, W. T., Anderson, M. C., and Kustas, W. P.: Microwave implementation of two-source energy balance approach for estimating evapotranspiration, Hydrology and Earth System Sciences, 22, 1351, 2018.

Hou, A. Y., Kakar, R. K., Neeck, S., Azarbarzin, A. A., Kummerow, C. D., Kojima, M., Oki, R., Nakamura, K., and Iguchi, T.: The global precipitation measurement mission, Bulletin of the American Meteorological Society, 95, 701–722, 2014.

Houldcroft, C. J., Grey, W. M., Barnsley, M., Taylor, C. M., Los, S. O., and North, P. R.: New vegetation albedo parameters and global fields of soil background albedo derived from MODIS for use in a climate model, Journal of Hydrometeorology, 10, 183–198, 2009.

Huffman, G. J., Bolvin, D. T., and Nelkin, E. J.: Integrated Multi-satellitE Retrievals for GPM (IMERG) technical documentation, NASA/GSFC Code, 612, 47, 2015.

Idso, S., Jackson, R., Reginato, R., Kimball, B., and Nakayama, F.: The dependence of bare soil albedo on soil water content, Journal of Applied Meteorology, 14, 109–113, 1975.

Imaoka, K., Kachi, M., Fujii, H., Murakami, H., Hori, M., Ono, A., Igarashi, T., Nakagawa, K., Oki, T., Honda, Y., et al.: Global Change Observation Mission (GCOM) for monitoring carbon, water cycles, and climate change, Proceedings of the IEEE, 98, 717–734, 2010.

Jackson, T. J.: III. Measuring surface soil moisture using passive microwave remote sensing, Hydrological Processes, 7, 139–152, 1993.

Jackson, T. J., Bindlish, R., Cosh, M. H., Zhao, T., Starks, P. J., Bosch, D. D., Seyfried, M., Moran, M. S., Goodrich, D. C., Kerr, Y. H., et al.: Validation of soil moisture and ocean salinity (SMOS) soil moisture over watershed networks in the US, Geoscience and Remote Sensing, IEEE Transactions on, 50, 1530–1543, 2012.

Jazwinski, A. H.: Stochastic Processes and Filtering Theory, vol. 64, Academic Press, 1970.

Jin, M.: Interpolation of surface radiative temperature measured from polar orbiting satellites to a diurnal cycle 2. Cloudy-pixel treatment, J. Geophys. Res, 105, 4061–4076, 2000.

Kalman, R. E.: A new approach to linear filtering and prediction problems, Journal of Basic Engineering, 82, 35–45, 1960.

Kerr, Y. H., Waldteufel, P., Wigneron, J.-P., Martinuzzi, J., Font, J., and Berger, M.: Soil moisture retrieval from space: The Soil Moisture and Ocean Salinity (SMOS) mission, IEEE Transactions on Geoscience and Remote Sensing, 39, 1729–1735, 2001.

Kim, S.-B., Moghaddam, M., Tsang, L., Burgin, M., Xu, X., and Njoku, E. G.: Models of L-band radar backscattering coefficients over global terrain for soil moisture retrieval, IEEE Transactions on Geoscience and Remote Sensing, 52, 1381–1396, 2014.

Klein, L. and Swift, C.: An improved model for the dielectric constant of sea water at microwave frequencies, IEEE Journal of Oceanic Engineering, 2, 104–111, 1977.

Knyazikhin, Y., Glassy, J., Privette, J., Tian, Y., Lotsch, A., Zhang, Y., Wang, Y., Morisette, J., Votava, P., Myneni, R., et al.: MODIS leaf area index (LAI) and fraction of photosynthetically active radiation absorbed by vegetation (FPAR) product (MOD15) algorithm theoretical basis document, Theoretical Basis Document, NASA Goddard Space Flight Center, Greenbelt, MD, 20771, 1999.

Kornelsen, K. C. and Coulibaly, P.: Reducing multiplicative bias of satellite soil moisture retrievals, Remote Sensing of Environment, 165, 109–122, 2015.

Kornelsen, K. C., Cosh, M. H., and Coulibaly, P.: Potential of bias correction for downscaling passive microwave and soil moisture data, Journal of Geophysical Research: Atmospheres, 120, 6460–6479, 2015.

Koster, R. D., Dirmeyer, P. A., Guo, Z., Bonan, G., Chan, E., Cox, P., Gordon, C., Kanae, S., Kowalczyk, E., Lawrence, D., et al.: Regions of strong coupling between soil moisture and precipitation, Science, 305, 1138–1140, 2004.

Kumar, S. V., Reichle, R. H., Harrison, K. W., Peters-Lidard, C. D., Yatheendradas, S., and Santanello, J. A.: A comparison of methods for a priori bias correction in soil moisture data assimilation, Water Resources Research, 48, 2012.

Kustas, W., Schmugge, T., Humes, K., Jackson, T., Parry, R., Weltz, M., and Moran, M.: Relationships between evaporative fraction and remotely sensed vegetation index and microwave brightness temperature for semiarid rangelands, Journal of Applied Meteorology, 32, 1781–1790, 1993.

Kustas, W., Humes, K., Norman, J., and Moran, M.: Single-and dual-source modeling of surface energy fluxes with radiometric surface temperature, Journal of Applied Meteorology, 35, 110–121, 1996.

Lee, H., Seo, D.-J., Liu, Y., Koren, V., McKee, P., and Corby, R.: Variational assimilation of streamflow into operational distributed hydrologic models: effect of spatiotemporal scale of adjustment, Hydrology and Earth System Sciences, 16, 2233–2251, doi:10.5194/hess-16-2233-2012, URL https://www.hydrol-earth-syst-sci.net/16/2233/2012/, 2012.

Leisenring, M. and Moradkhani, H.: Snow water equivalent prediction using Bayesian data assimilation methods, Stochastic Environmental Research and Risk Assessment, 25, 253–270, 2011.

Leisenring, M. and Moradkhani, H.: Analyzing the uncertainty of suspended sediment load prediction using sequential data assimilation, Journal of hydrology, 468, 268–282, 2012.

Lhomme, J. P. and Elguero, E.: Examination of evaporative fraction diurnal behaviour using a soil-vegetation model coupled with a mixed-layer model, Hydrology and Earth System Sciences Discussions, 3, 259–270, 1999.

Li, Z.-L., Tang, B.-H., Wu, H., Ren, H., Yan, G., Wan, Z., Trigo, I. F., and Sobrino, J. A.: Satellite-derived land surface temperature: Current status and perspectives, Remote Sensing of Environment, 131, 14–37, 2013.

Lievens, H., De Lannoy, G., Al Bitar, A., Drusch, M., Dumedah, G., Franssen, H.-J. H., Kerr, Y., Tomer, S. K., Martens, B., Merlin, O., et al.: Assimilation of SMOS soil moisture and brightness temperature products into a land surface model, Remote Sensing of Environment, 180, 292–304, 2016.

Lievens, H., Martens, B., Verhoest, N., Hahn, S., Reichle, R., and Miralles, D.: Assimilation of global radar backscatter and radiometer brightness temperature observations to improve soil moisture and land evaporation estimates, Remote Sensing of Environment, 189, 194–210, 2017a.

Lievens, H., Reichle, R. H., Liu, Q., De Lannoy, G., Dunbar, R. S., Kim, S., Das, N. N., Cosh, M., Walker, J. P., and Wagner, W.: Joint Sentinel-1 and SMAP data assimilation to improve soil moisture estimates, Geophysical Research Letters, 2017b.

Lu, Y., Dong, J., Steele-Dunne, S. C., and van de Giesen, N.: Estimating surface turbulent heat fluxes from land surface temperature and soil moisture observations using the particle batch smoother, Water Resources Research, 52, 9086–9108, 2016.

Lu, Y., Steele-Dunne, S. C., Farhadi, L., and van de Giesen, N.: Mapping surface heat fluxes by assimilating SMAP soil moisture and GOES land surface temperature data, Water Resources Research, 53, 10 858–10 877, 2017.

Ma, Y., Menenti, M., and Feddes, R.: Parameterization of heat fluxes at heterogeneous surfaces by integrating satellite measurements with surface layer and atmospheric boundary layer observations, Advances in Atmospheric Sciences, 27, 328–336, 2010.

Margulis, S. A., McLaughlin, D., Entekhabi, D., and Dunne, S.: Land data assimilation and estimation of soil moisture using measurements from the Southern Great Plains 1997 Field Experiment, Water Resources Research, 38, 2002.

Margulis, S. A., Girotto, M., Cortés, G., and Durand, M.: A particle batch smoother approach to snow water equivalent estimation, Journal of Hydrometeorology, 16, 1752–1772, 2015.

Minacapilli, M., Consoli, S., Vanella, D., Ciraolo, G., and Motisi, A.: A time domain triangle method approach to estimate actual evapotranspiration: Application in a Mediterranean region using MODIS and MSG-SEVIRI products, Remote Sensing of Environment, 174, 10–23, 2016.

Mironov, V. L., Kosolapova, L. G., and Fomin, S. V.: Physically and mineralogically based spectroscopic dielectric model for moist soils, IEEE Transactions on Geoscience and Remote Sensing, 47, 2059–2070, 2009.

Mladenova, I., Jackson, T., Njoku, E., Bindlish, R., Chan, S., Cosh, M., Holmes, T., De Jeu, R., Jones, L., Kimball, J., et al.: Remote monitoring of soil moisture using passive microwave-based techniques-Theoretical basis and overview of selected algorithms for AMSR-E, Remote Sensing of Environment, 144, 197–213, 2014.

Montzka, C., Herbst, M., Weihermüller, L., Verhoef, A., and Vereecken, H.: A global data set of soil hydraulic properties and sub-grid variability of soil water retention and hydraulic conductivity curves, Earth System Science Data, 9, 529–543, doi: 10.5194/essd-9-529-2017, URL https://www.earth-syst-sci-data.net/9/529/2017/, 2017.

Moradkhani, H., Hsu, K.-L., Gupta, H., and Sorooshian, S.: Uncertainty assessment of hydrologic model states and parameters: Sequential data assimilation using the particle filter, Water Resources Research, 41, 2005.

Moradkhani, H., DeChant, C. M., and Sorooshian, S.: Evolution of ensemble data assimilation for uncertainty quantification using the particle filter-Markov chain Monte Carlo method, Water Resources Research, 48, 2012.

Niu, G.-Y., Yang, Z.-L., Mitchell, K. E., Chen, F., Ek, M. B., Barlage, M., Kumar, A., Manning, K., Niyogi, D., Rosero, E., et al.: The community Noah land surface model with multiparameterization options (Noah-MP): 1. Model description and evaluation with local-scale measurements, Journal of Geophysical Research: Atmospheres, 116, 2011.

Njoku, E. G. and Entekhabi, D.: Passive microwave remote sensing of soil moisture, Journal of Hydrology, 184, 101–129, 1996.

Njoku, E. G., Jackson, T. J., Lakshmi, V., Chan, T. K., and Nghiem, S. V.: Soil moisture retrieval from AMSR-E, IEEE Transactions on Geoscience and Remote Sensing, 41, 215–229, 2003.

Norman, J. M., Kustas, W. P., and Humes, K. S.: A two-source approach for estimating soil and vegetation energy fluxes in observations of directional radiometric surface temperature, Agricultural and Forest Meteorology, 77, 263–293, 1995.

Oleson, K. W., Lawrence, D. M., Gordon, B., Flanner, M. G., Kluzek, E., Peter, J., Levis, S., Swenson, S. C., Thornton, E., Feddema, J., et al.: Technical description of version 4.0 of the Community Land Model (CLM), 2010.

O'Neill, P., Njoku, E., Jackson, T., Chan, S., and Bindlish, R.: SMAP algorithm theoretical basis document: Level 2 & 3 soil moisture (passive) data products, Jet Propulsion Lab., California Inst. Technol., Pasadena, CA, USA, JPL D-66480, 2015.

Pan, M., Cai, X., Chaney, N. W., Entekhabi, D., and Wood, E. F.: An initial assessment of SMAP soil moisture retrievals using high-resolution model simulations and in situ observations, Geophysical Research Letters, 43, 9662–9668, 2016.

Peng, J., Borsche, M., Liu, Y., and Loew, A.: How representative are instantaneous evaporative fraction measurements for daytime fluxes?, Hydrology and Earth System Sciences, 17, 3913–3919, 2013.

Reichle, R., Crow, W., Koster, R., Kimball, J., and De Lannoy, G.: Algorithm Theoretical Basis Document (ATBD) SMAP Level 4 Surface and Root Zone Soil Moisture (L4_SM) Data Product, NASA Goddard Space Flight Center: Greenbelt, MD, USA, 2012.

Reichle, R. H.: Data assimilation methods in the Earth sciences, Advances in Water Resources, 31, 1411–1418, 2008.

Reichle, R. H. and Koster, R. D.: Bias reduction in short records of satellite soil moisture, Geophysical Research Letters, 31, 2004.

Reichle, R. H., Entekhabi, D., and McLaughlin, D. B.: Downscaling of radio brightness measurements for soil moisture estimation: A four-dimensional variational data assimilation approach, Water Resources Research, 37, 2353–2364, 2001a.

Reichle, R. H., McLaughlin, D. B., and Entekhabi, D.: Variational data assimilation of microwave radiobrightness observations for land surface hydrology applications, IEEE Transactions on Geoscience and Remote Sensing, 39, 1708–1718, 2001b.

Reichle, R. H., Koster, R. D., Dong, J., and Berg, A. A.: Global soil moisture from satellite observations, land surface models, and ground data: Implications for data assimilation, Journal of Hydrometeorology, 5, 430–442, 2004.

Reichle, R. H., Crow, W. T., and Keppenne, C. L.: An adaptive ensemble Kalman filter for soil moisture data assimilation, Water Resources Research, 44, 2008.

Reichle, R. H., De Lannoy, G. J., Liu, Q., Ardizzone, J. V., Colliander, A., Conaty, A., Crow, W., Jackson, T. J., Jones, L. A., Kimball, J. S., et al.: Assessment of the SMAP Level-4 Surface and Root-Zone Soil Moisture Product Using In Situ Measurements, Journal of Hydrometeorology, 18, 2621–2645, 2017a.

Reichle, R. H., De Lannoy, G. J., Liu, Q., Koster, R. D., Kimball, J. S., Crow, W. T., Ardizzone, J. V., Chakraborty, P., Collins, D. W., Conaty, A. L., et al.: Global Assessment of the SMAP Level-4 Surface and Root-Zone Soil Moisture Product Using Assimilation Diagnostics, Journal of Hydrometeorology, 18, 3217–3237, 2017b.

Rigden, A. J. and Salvucci, G. D.: Evapotranspiration based on equilibrated relative humidity (ETRHEQ): Evaluation over the continental U.S., Water Resources Research, 51, 2951–2973, 2015.

Sahoo, A. K., De Lannoy, G. J., Reichle, R. H., and Houser, P. R.: Assimilation and downscaling of satellite observed soil moisture over the Little River Experimental Watershed in Georgia, USA, Advances in Water Resources, 52, 19–33, 2013.

Santanello, J. A., Peters-Lidard, C. D., and Kumar, S. V.: Diagnosing the sensitivity of local land-atmosphere coupling via the soil moisture-boundary layer interaction, Journal of Hydrometeorology, 12, 766–786, 2011.

Schaap, M. G., Leij, F. J., and Van Genuchten, M. T.: ROSETTA: a computer program for estimating soil hydraulic parameters with hierarchical pedotransfer functions, Journal of Hydrology, 251, 163–176, 2001.

Schaefer, G. L., Cosh, M. H., and Jackson, T. J.: The USDA natural resources conservation service soil climate analysis network (SCAN), Journal of Atmospheric and Oceanic Technology, 24, 2073–2077, 2007.

Sellers, P., Mintz, Y., Sud, Y. e. a., and Dalcher, A.: A simple biosphere model (SiB) for use within general circulation models, Journal of the Atmospheric Sciences, 43, 505–531, 1986.

Sellers, P. J., Hall, F. G., Asrar, G., Strebel, D., and Murphy, R.: An overview of the first international satellite land surface climatology project (ISLSCP) field experiment (FIFE), Journal of Geophysical Research: Atmospheres (1984–2012), 97, 18 345–18 371, 1992.

Seneviratne, S. I., Corti, T., Davin, E. L., Hirschi, M., Jaeger, E. B., Lehner, I., Orlowsky, B., and Teuling, A. J.: Investigating soil moisture–climate interactions in a changing climate: A review, Earth-Science Reviews, 99, 125–161, 2010.

Seo, D.-J., Koren, V., and Cajina, N.: Real-time variational assimilation of hydrologic and hydrometeorological data into operational hydrologic forecasting, Journal of Hydrometeorology, 4, 627–641, 2003.

Shellito, P. J., Small, E. E., Colliander, A., Bindlish, R., Cosh, M. H., Berg, A. A., Bosch, D. D., Caldwell, T. G., Goodrich, D. C., McNairn, H., et al.: SMAP soil moisture drying more rapid than observed in situ following rainfall events, Geophysical Research Letters, 43, 8068–8075, 2016.

Shokri, N., Lehmann, P., Vontobel, P., and Or, D.: Drying front and water content dynamics during evaporation from sand delineated by neutron radiography, Water Resources Research, 44, 2008.

Simunek, J., Van Genuchten, M. T., and Sejna, M.: The HYDRUS-1D software package for simulating the movement of water, heat, and multiple solutes in variably saturated media, version 3.0, HYDRUS software series 1, Department of Environmental Sciences, University of California Riverside, Riverside Edition, 2005.

Sini, F., Boni, G., Caparrini, F., and Entekhabi, D.: Estimation of large-scale evaporation fields based on assimilation of remotely sensed land temperature, Water Resources Research, 44, 2008.

Sobrino, J. and Romaguera, M.: Land surface temperature retrieval from MSG1-SEVIRI data, Remote Sensing of Environment, 92, 247–254, 2004.

Stordal, A. S., Karlsen, H. A., Nævdal, G., Skaug, H. J., and Vallès, B.: Bridging the ensemble Kalman filter and particle filters: the adaptive Gaussian mixture filter, Computational Geosciences, 15, 293–305, 2011.

Su, C.-H. and Ryu, D.: Multi-scale analysis of bias correction of soil moisture, Hydrology and Earth System Sciences, 19, 17–31, 2015.

Su, Z.: The Surface Energy Balance System (SEBS) for estimation of turbulent heat fluxes, Hydrology and Earth System Sciences Discussions, 6, 85–100, 2002.

Sun, D. and Pinker, R. T.: Estimation of land surface temperature from a Geostationary Operational Environmental Satellite (GOES-8), Journal of Geophysical Research: Atmospheres, 108, 2003.

Sutanto, S., Wenninger, J., Coenders-Gerrits, A., and Uhlenbrook, S.: Partitioning of evaporation into transpiration, soil evaporation and interception: a comparison between isotope measurements and a HYDRUS-1D model, Hydrology and Earth System Sciences, 16, 2605–2616, 2012.

Tang, R., Li, Z.-L., and Tang, B.: An application of the T_s–VI triangle method with enhanced edges determination for evapotranspiration estimation from MODIS data in arid and semi-arid regions: Implementation and Validation, Remote Sensing of Environment, 114, 540–551, 2010.

Tian, X., Xie, Z., Dai, A., Shi, C., Jia, B., Chen, F., and Yang, K.: A dual-pass variational data assimilation framework for estimating soil moisture profiles from AMSR-E microwave brightness temperature, Journal of Geophysical Research: Atmospheres, 114, 2009.

Twine, T. E., Kustas, W., Norman, J., Cook, D., Houser, P., Meyers, T., Prueger, J., Starks, P., and Wesely, M.: Correcting eddy-covariance flux underestimates over a grassland, Agricultural and Forest Meteorology, 103, 279–300, 2000.

Van Genuchten, M. T.: A closed-form equation for predicting the hydraulic conductivity of unsaturated soils, Soil Science Society of America Journal, 44, 892–898, 1980.

Vickers, D., Göckede, M., and Law, B. E.: Uncertainty estimates for 1-h averaged turbulence fluxes of carbon dioxide, latent heat and sensible heat, Tellus B, 62, 87–99, 2010.

Wanders, N., Karssenberg, D., Roo, A. d., De Jong, S., and Bierkens, M.: The suitability of remotely sensed soil moisture for improving operational flood forecasting, Hydrology and Earth System Sciences, 18, 2343–2357, 2014.

Wang, J. R. and Schmugge, T. J.: An empirical model for the complex dielectric permittivity of soils as a function of water content, IEEE Transactions on Geoscience and Remote Sensing, pp. 288–295, 1980.

Wang, K. and Dickinson, R. E.: A review of global terrestrial evapotranspiration: Observation, modeling, climatology, and climatic variability, Reviews of Geophysics, 50, 2012.

Wang, K., Li, Z., and Cribb, M.: Estimation of evaporative fraction from a combination of day and night land surface temperatures and NDVI: A new method to determine the Priestley–Taylor parameter, Remote Sensing of Environment, 102, 293–305, 2006.

Wigneron, J.-P., Laguerre, L., and Kerr, Y. H.: A simple parameterization of the L-band microwave emission from rough agricultural soils, IEEE Transactions on Geoscience and Remote Sensing, 39, 1697–1707, 2001.

Wigneron, J.-P., Chanzy, A., De Rosnay, P., Rudiger, C., and Calvet, J.-C.: Estimating the effective soil temperature at L-band as a function of soil properties, IEEE Transactions on Geoscience and Remote Sensing, 46, 797–807, 2008.

Wilson, K., Goldstein, A., Falge, E., Aubinet, M., Baldocchi, D., Berbigier, P., Bernhofer, C., Ceulemans, R., Dolman, H., Field, C., et al.: Energy balance closure at FLUXNET sites, Agricultural and Forest Meteorology, 113, 223–243, 2002.

Xia, Y., Mitchell, K., Ek, M., Sheffield, J., Cosgrove, B., Wood, E., Luo, L., Alonge, C., Wei, H., Meng, J., et al.: Continental-scale water and energy flux analysis and validation for the North American Land Data Assimilation System project phase 2 (NLDAS-2): 1. Intercomparison and application of model products, Journal of Geophysical Research: Atmospheres, 117, 2012.

Xu, T., Bateni, S., Liang, S., Entekhabi, D., and Mao, K.: Estimation of surface turbulent heat fluxes via variational assimilation of sequences of land surface temperatures from Geostationary Operational Environmental Satellites, Journal of Geophysical Research: Atmospheres, 119, 10–780, 2014.

Xu, T., Bateni, S. M., and Liang, S.: Estimating turbulent heat fluxes with a weak-constraint data assimilation scheme: A case study (HiWATER-MUSOEXE), Geoscience and Remote Sensing Letters, IEEE, 12, 68–72, 2015.

Xu, T., Bateni, S., Neale, C., Auligne, T., and Liu, S.: Estimation of Turbulent Heat Fluxes by Assimilation of Land Surface Temperature Observations From GOES Satellites Into an Ensemble Kalman Smoother Framework, Journal of Geophysical Research: Atmospheres, 123, 2409–2423, 2018.

Yan, H. and Moradkhani, H.: Combined assimilation of streamflow and satellite soil moisture with the particle filter and geostatistical modeling, Advances in Water Resources, 94, 364–378, 2016.

Yan, H., DeChant, C. M., and Moradkhani, H.: Improving soil moisture profile prediction with the particle filter-Markov chain Monte Carlo method, Geoscience and Remote Sensing, IEEE Transactions on, 53, 6134–6147, 2015.

Yang, K., Zhu, L., Chen, Y., Zhao, L., Qin, J., Lu, H., Tang, W., Han, M., Ding, B., and Fang, N.: Land surface model calibration through microwave data assimilation for improving soil moisture simulations, Journal of Hydrology, 533, 266–276, 2016.

Yilmaz, M. T. and Crow, W. T.: The optimality of potential rescaling approaches in land data assimilation, Journal of Hydrometeorology, 14, 650–660, 2013.

Zeng, J., Chen, K.-S., Bi, H., and Chen, Q.: A preliminary evaluation of the SMAP radiometer soil moisture product over United States and Europe using ground-based

measurements, IEEE Transactions on Geoscience and Remote Sensing, 54, 4929–4940, 2016.

Zeng, X.: Global vegetation root distribution for land modeling, Journal of Hydrometeorology, 2, 525–530, 2001.

Zhao, L., Yang, Z.-L., and Hoar, T. J.: Global soil moisture estimation by assimilating AMSR-E brightness temperatures in a coupled CLM4–RTM–DART system, Journal of Hydrometeorology, 17, 2431–2454, 2016.

Zheng, D., van der Velde, R., Su, Z., Wang, X., Wen, J., Booij, M. J., Hoekstra, A. Y., and Chen, Y.: Augmentations to the Noah model physics for application to the Yellow River source area. Part II: Turbulent heat fluxes and soil heat transport, Journal of Hydrometeorology, 16, 2677–2694, 2015.

Zhu, W., Jia, S., and Lv, A.: A Universal Ts-VI Triangle Method for the Continuous Retrieval of Evaporative Fraction From MODIS Products, Journal of Geophysical Research: Atmospheres, 122, 2017.

ACKNOWLEDGEMENTS

After acting as the photographer at many PhD defenses in the past five years, it's finally my chance to step forward and stand in front of the camera. A PhD research is never easy for anyone, and I'm grateful that mine has always been challenging and rewarding, which would be impossible without the help of many people.

I would like to thank Prof. Nick van de Giesen for offering me the opportunity to do my research in this world-renowned university in such a marvellous country. Nick gave me sufficient directions in the beginning of my PhD research and has always been supportive in offering me opportunities to increase my exposure in the community in conferences and workshops. I also get enough freedom to do my own research.

My sincere gratitude goes to my promotor Prof. Susan Steele-Dunne. I always remember that one afternoon after 6 months into my PhD when I was so lost in finding a research topic, Susan came to me and asked 'Would you like a decent coffee downstairs?'. In the coffee corner on the first floor, Susan explained to me the idea of estimating energy fluxes using thermal and wetness information, which little by little developed into this PhD research. Looking backward, that was one moment that changed my life. During my PhD trajectory, I always got quick and valuable input from Susan whenever I had problems. I also learned a lot from her on how to act professionally as a researcher. I am deeply indebted to Susan, and it's been an honour working with her.

I want to thank my colleagues in room 4.97 during the years for a lovely and multicultural office: Dr. Ruud van der Ent, Dr. Koen Hilgersom, Bao Anh Nong, Dr. Yee Mon Thu, Xinyu Liu, Judith Uwihirwe and Changrang Zhou. In particular, I would like to thank Koen for making calls to IND for me on visa issues before my vacation to Morocco, and to thank Ruud for translating the Summary into an outstanding Samenvatting with great patience. I also thank Prof. Gabriëlle De Lannoy for her help in translating the data assimilation jargons into Dutch.

I wish to thank the SMAPVEX16 experiment team: Dr. Mike Cosh, Dr. Lynn McKee, Prof. Brian Hornbuckle, Victoria Walker, Jimmie Bragdon, Prof. John Qu, Alex White, Patrick O'connor, Melanie Feliciano, Hyunglok Kim, Eunsang Cho, Prof. Long Zhao, Jiyue Zhu, Huanting Huang, Chenyang Xu, Jaime Polo and Dr. Subit Chakrabarti. I enjoyed working and living together with you guys, although it was torturous to get up before 6 am to collect soil data. In particular, I want to thank my team-mate Alex for showing me the right way to conduct field work with his rich experience and Patrick for being a nice host and a great guide.

My thankfulness goes to all my colleagues in the department of water management. This acknowledgement would be incredibly long if I were to list their names one by one. I want to thank Petra Hulsman for helping me to confirm my energy contract with Eneco and Dr. Gerrit Schoups for cancelling it. I also wish to offer my special thanks to Dr. Jianzhi Dong, Dr. Xin Tian and Dr. Yingrong Wen for their continued help throughout the years.

My research would not have been worry-free without the hard work and great expertise of our wonderful secretaries: Betty Rothfusz, Lydia de Hoog and Luz Ton-Estrada. I also thank my basketball team-mates for all the sweating and refreshing Friday afternoons on the basketball court.

I'm deeply grateful to my father Yuming Lu and my mother Limin Zheng for supporting me to pursue a PhD overseas. I'm so indepted to you, and I hope I have made you proud. I'm grateful to my aunt Hongyan Zheng and my uncle Yang Cao for taking great care of my grandparents. I also want to take this opportunity to thank my fiancée's elder sister Dr. Wei Wei and her husband Zhe Tang for taking care of my parents-in-law-to-be Mr. Shuxiang Wei and Mrs. Meixiu Huang when we were away in Europe.

Most importantly, I wish to express my heartfelt gratitude to my fiancée Dr. Chunzhu Wei. Thank you for being my harbour when I'm tired and my shield when I'm weak. I feel sorry for not being able to be by your side in the past five years when you needed me, and I hope to make it up to you in the rest of my life. I try not to be emotional when I write this, but you know I love you with all my heart.

Yang Lu
August 2018

CURRICULUM VITÆ

Yang LU

31-08-1989 Born in Xinyang, China.

EDUCATION

Jan 2019 PhD in water management
Delft University of Technology, Delft, the Netherlands
Thesis: Estimating Surface Heat Fluxes Using Temperature And Wetness Information
Promotors: Prof. dr. ir. Susan C. Steele-Dunne
Prof. dr. ir. Nick C. van de Giesen

Jun 2013 MSc. in remote sensing of hydrology
Beijing Normal University, Beijing, China
Thesis: Spatio-temporal Downscaling of TRMM Precipitation Data in the Yarlung-Zangbo River Basin

Jun 2010 B.E. in surveying and mapping
Tongji University, Shanghai, China
Thesis: Combined Navigation of GPS-INS using the Kalman Filter

FIELD EXPERIMENTS

May-Jun 2016 SMAPVEX16 Experiment Intensive Observation Period 1
Ames, Iowa, United States

Aug 2016 SMAPVEX16 Experiment Intensive Observation Period 2
Ames, Iowa, United States

PRESENTATIONS (SELECTED)

Y. Lu, Susan C. Steele-Dunne, Nick van de Giesen, *Mapping surface heat fluxes by assimilating GOES land surface temperature and SMAP products*, AGU Fall Meeting, New Orleans, United States, December 2017. (oral presentation)

Y. Lu, Susan C. Steele-Dunne, Nick van de Giesen, *Mapping soil moisture and surface heat fluxes by assimilating GOES land surface temperature and SMAP soil moisture data*, EGU General Assembly, Vienna, Austria, April 2017. (oral presentation)

Y. Lu, Jianzhi Dong, Susan C. Steele-Dunne, Nick van de Giesen, *Estimating surface heat fluxes by assimilating land surface temperature and soil moisture data*, Boussinesq Lectures, Brussels, Belgium, October 2016. (oral presentation)

Y. Lu, Jianzhi Dong, Susan C. Steele-Dunne, Nick van de Giesen, *Estimating surface turbulent heat fluxes from land surface temperature and soil moisture using the particle batch smoother*, EGU General Assembly, Vienna, Austria, April 2016. (oral presentation)

LIST OF PUBLICATIONS

4. **Y. Lu**, Jianzhi Dong, Susan C. Steele-Dunne. *Impact of Soil Moisture Data Resolution on Soil Moisture and Surface Heat Flux Estimates Through Data Assimilation. (submitted)*

3. **Y. Lu**, Susan C. Steele-Dunne, Gabriëlle De Lannoy. *Improving Surface Heat Flux Estimates by Assimilation of SMAP Brightness Temperature and GOES Land Surface Temperature Data. (in revision)*

2. **Y. Lu**, Susan C. Steele-Dunne, Leila Farhadi, Nick van de Giesen. *Mapping Surface Heat Fluxes by Assimilating SMAP Soil Moisture and GOES Land Surface Temperature Data*, Water Resources Research, **53**, 10858-10877, 2017.

1. **Y. Lu**, Jianzhi Dong, Susan C. Steele-Dunne, Nick van de Giesen. *Estimating Surface Turbulent Heat Fluxes from Land Surface Temperature and Soil Moisture Observations Using the Particle Batch Smoother*, Water Resources Research, **52**, 9086-9108, 2016.